

Johannes Gutenberg-Universität Mainz

**Manipulation of Néel vector in
antiferromagnetic Mn_2Au by electric
current and magnetic field pulses.**



Dissertation
zur Erlangung des Grades
"Doktor der Naturwissenschaften"
am Fachbereich Physik, Mathematik und Informatik
der Johannes Gutenberg-Universität
in Mainz

Stanislav Bodnar

geboren am 25. Dezember 1990
in Wolgograd, USSR

7. Mai 2020

Contents

List of Figures	vi
Abbreviations	viii
List of publications	ix
Abstract	x
Kurzfassung	xii
Introduction	xiv
1 Mechanisms of manipulation of Néel vector in antiferromagnets	1
1.1 Methods of manipulation of the Néel vector in antiferromagnets	1
1.2 Manipulation of the Néel vector in antiferromagnets with locally broken inversion symmetry via Néel spin-orbit torque	4
1.3 Manipulation of the Néel vector in antiferromagnetic CuMnAs	8
2 Experimental techniques used in this work	11
2.1 Radio frequency magnetron sputtering	11
2.2 X-ray diffraction characterization	13
2.3 Scanning electron microscopy and atomic force microscopy	15
2.4 The experimental setup for the transport measurements	16
2.5 High magnetic field pulse cryostat	17
2.6 X-ray Magnetic Linear/Circular Dichroism Photoemission Electron Microscopy	19
2.6.1 X-ray absorption spectroscopy	21
2.6.2 X-ray circular magnetic dichroism	22
2.6.3 X-ray linear magnetic dichroism	24
3 Sample preparation	26
3.1 Optimization of crystal quality of the Mn ₂ Au thin films	26
3.2 Optimization of the morphology of the Mn ₂ Au thin films	30
3.3 Patterning of the Mn ₂ Au microstructures by optical lithography	33
4 Current induced switching of Néel vector in Mn₂Au	35
4.1 Current-induced Néel vector reorientation in Mn ₂ Au	35
4.2 The role of heating in the Néel vector switching process	39

4.3	Simulation of the current distribution in the microstructures	41
5	Direct visualization of current induced Néel vector switching in Mn₂Au	44
5.1	Visualization of the antiferromagnetic domains in Mn ₂ Au	44
5.2	Switching of the Néel vector in the as-prepared sample	51
5.3	Néel vector switching in Mn ₂ Au with prealined Néel vector	55
5.4	Evaluation of the switched domains fraction	57
6	Manipulation of the Néel vector in Mn₂Au by high magnetic field pulses	60
6.1	Persistent magnetoresistance effects in Mn ₂ Au induced by high magnetic field pulse	61
6.2	Fast magnetoresistance measurements	65
6.3	The effect of the magnetoresistance relaxation.	68
6.4	Visualization of the antiferromagnetic domain pattern of Mn ₂ Au exposed to large magnetic fields	70
7	Discussion of the results	76
7.1	The key role of the NSOT in the current induced manipulation of the Néel vector in Mn ₂ Au	76
7.2	Comparison of the experimentally observed AMR with theoretically estimated values	78
7.3	Persistent resistance changes induced by the current pulses	80
	Conclusion	82
	A Appendix	84
	Bibliography	88
	Contributions	91
	Curriculum Vitae	92

List of Figures

1.1	Schematic image of AFM/FM spin-spring system.	2
1.2	Switching of Néel vector in NiO.	3
1.3	Effect of bands splitting due to Rashba splitting.	5
1.4	Crystal structure and magnetic structure of Mn ₂ Au.	6
1.5	Shift of Fermi surfaces	7
1.6	Geometry of the NSOT	8
1.7	Crystal and magnetic structure of CuMnAs	9
1.8	Current induced Néel vector switching in CuMnAs	9
2.1	Scheme of RF-sputtering chamber	12
2.2	Scheme of reflection of x-ray from lattice.	13
2.3	Scheme of $\theta/2\theta$ geometry	14
2.4	Scheme of mosaicity.	15
2.5	Scheme of the SEM and AFM microscopes.	16
2.6	Scheme of transport setup	17
2.7	Schematic picture of magnetic cryostat.	18
2.8	Time profile of the magnetic field pulse	19
2.9	Schematic picture of large scale synchrotron facility.	20
2.10	Scheme of the X-PEEM setup.	21
2.11	Transition of electrons in x-ray range of energies	22
2.12	Origins of XMCD	23
2.13	Origins of XMLD	25
3.1	$\theta/2\theta$ XRD scan of Mn ₂ Au thin film.	27
3.2	Rocking curves of Mn ₂ Au grown at different temperatures	28
3.3	Rocking curve of the Mn ₂ Au thin film for two different in-plane orientations	29
3.4	In-plane XRD φ -scan of 80 nm Mn ₂ Au thin film	30
3.5	SEM and AFM scans of the samples grown at high temperature	31
3.6	SEM and AFM scans of the samples grown at the different temperatures	31
3.7	SEM and AFM scans of the samples grown at the different temperatures	32
3.8	Optical lithography steps.	33
3.9	Layout of the structure used for transport measurements.	34
4.1	Sample layout	36
4.2	Current induced changes of transversal resistivity	37
4.3	Current induced changes of longitudinal and transversal resistivities.	38
4.4	Current induced changes of resistance in saturation regime	38
4.5	Sample temperature while application of current pulses	40

4.6	Electric field distribution while application writing pulses	42
4.7	Electric field distribution while application probe current	42
5.1	Schematic picture of X-PEEM setup geometry	45
5.2	Transition of electrons in x-ray range of energies	46
5.3	XMLD-PEEM asymmetry image of 240 nm Mn_2Au thin films.	47
5.4	XMLD-PEEM asymmetry for two sample orientations	48
5.5	AFM scan of the sample used for the Néel vector switching experiment . .	49
5.6	Origins of the remained morphology in asymmetry images in Mn_2Au . . .	50
5.7	Histogram distribution of the intensity of the XMLD-PEEM asymmetric images.	51
5.8	Sample layout of the sample used for experiments on Néel vector switching visualization.	52
5.9	XMLD-PEEM asymmetry images taken before and after application of current pulses	53
5.10	Difference XMLD-PEEM images taken in as-prepared sample.	54
5.11	Schematic picture of the current applied in a sample with tilted (001) plane. . .	55
5.12	Difference images taken obtained after application of current pulses along different directions	56
5.13	Black and white images of difference images.	58
5.14	Fraction of switched domains	58
6.1	XMLD-PEEM asymmetry image of a sample with prealigned Néel vector . .	61
6.2	Persistent changes of resistance in Mn_2Au induced by high field pulse . .	62
6.3	Persistent changes of resistance induced by high field pulse in Mn_2Au sample with reduced crystal quality	64
6.4	Persistent changes of resistance of a sample for the case of magnetic field being applied along hard axis	65
6.5	Magnetoresistance curve in Mn_2Au measured along easy axis.	66
6.6	Magnetoresistance curve in Mn_2Au measured along hard axes.	67
6.7	Magnetoresistance curve in Mn_2Au measured after two pulses.	68
6.8	Relaxation of magnetoresistance in Mn_2Au after spin flop transition . . .	69
6.9	XMLD-PEEM asymmetry images of AFM domains in Mn_2Au after spin flop transition.	70
6.10	Structure of the sample used for the visualization of the 180 degrees domains. .	71
6.11	XMCD/XMLD PEEM images of $\text{Mn}_2\text{Au}/\text{Fe}$ thin film with aligned Néel vector.	72
6.12	Schematic image of the domain structure Mn_2Au while the application of the high field pulse along the easy axis.	74
6.13	Schematic image of domain structure in Mn_2Au while application of the high field pulse along hard axis.	74
6.14	XMLD-PEEM asymmetry image of the sample after application of the high field pulse along hard axis.	75
7.1	Theoretically calculated value of AMR in Mn_2Au	79
A.1	Example of the mask design used for the X-PEEM experiments.	85
A.2	Temperature stability in magnetic cryostat at room temperature.	86

Abbreviations

AFM	AntiFerroMagnet
AMR	Anisotropic MagnetoResistance
FM	FerroMagnet
DFT	Density Functional Theory
DW	Domain Wall
PEEM	Photoemission Electron Microscopy
THZ	TeraHertz
NSOT	NeelSpinOrbitTorque
SEM	Scanning Electron Microscopy
STT	Spin Transfer Torque
SOT	Spin Orbit Torque
SMR	Spin Hall Magnetoresistance
T_N	Neel Temperature
UHV	Ultra-High Vacuum
XRD	Xray Diffraction
XAS	Xray Absorption Spectrum
XMLD	Xray Magnetic Linear Dichroism
XMCD	Xray Magnetic Circular Dichroism

List of publications

- 1) S. Yu. Bodnar, L. Smejkal, I. Turek, T. Jungwirth, O. Gomonay, J. Sinova, A. A. Sapozhnik, H.-J. Elmers, M. Kläui and M. Jourdan. "*Writing and reading antiferromagnetic Mn_2Au by Néel spin-orbit torques and large anisotropic magnetoresistance*" Nature Communications 9, 348 (2018)
- 2) A. A. Sapozhnik, M. Filianina, S. Yu. Bodnar, A. Lamirand, M.-A. Mawass, Y. Skourski, H.-J. Elmers, H. Zabel, M. Kläui, and M. Jourdan. "*Direct imaging of antiferromagnetic domains in Mn_2Au manipulated by high magnetic fields.*" Phys. Rev. B 97, (2018)
- 3) S. Yu. Bodnar, M. Filianina, S. P. Bommanaboyena, T. Forrest, F. Maccherozzi, A. A. Sapozhnik, Y. Skourski, M. Kläui, and M. Jourdan. "*Imaging of current induced Néel vector switching in antiferromagnetic Mn_2Au .*" Phys. Rev. B 99, 140409(R) (2019)
- 4) S.Yu.Bodnar, Y.Skourski, S.P.Bommanaboyena, M.Kläui and M.Jourdan. "*Domain wall and anisotropic magnetoresistance of the antiferromagnet Mn_2Au .*" arXiv:1909.12606v2 .
- 5) H. J. Elmers, S. V. Chernov, S. Dsouza, S. P. Bommanaboyena, S. Yu. Bodnar, et al., "*Néel vector induced manipulation of valence states in the collinear antiferromagnet Mn_2Au* ". (ACS Nano submitted).

Abstract

In antiferromagnetic spintronics the Néel vector corresponding to the staggered magnetization is used to encode information. In the framework of spin-based electronics, antiferromagnets as active elements have a number of advantages compared to ferromagnetic materials: The natural spin dynamics of antiferromagnets in the THz range is of major significance as it makes this class of magnetic materials promising for ultrafast switching as well as for the generation and detection of THz radiation.

Furthermore, the lack of net magnetization of antiferromagnets makes their Néel vector oriented state robust with respect to external magnetic fields. This property results in a high stability of the information encoded in the Néel vector orientation, which cannot be destroyed by external magnetic fields. Last but not least, antiferromagnets do not produce stray fields, which are limiting the minimum feasible size of data storage units based on ferromagnets.

However, the lack of net magnetization makes the manipulation of the Néel vector orientation much more challenging than the corresponding manipulation of the magnetization of ferromagnets. One of the possible approaches is based on a current induced bulk spin-orbit torque, which was predicted to exist for very specific crystal structures of collinear antiferromagnets, the so-called Neel spin-orbit torque. Only two antiferromagnetic compounds with the required crystal structure are known up to now: Mn_2Au , on which this work is focused, and CuMnAs .

In my thesis, I investigate the effects of current pulses on the antiferromagnetic domain structure which is modified by a Néel vector reorientation originating from Néel spin-orbit torques and alternative effects. As an alternative Néel vector manipulation method, I also investigate the switching of the Néel vector orientation in Mn_2Au by the application of very large high magnetic field pulses causing a spin-flop transition.

To investigate current induced Néel vector switching in Mn_2Au , I performed electric transport measurements where I measured current-induced changes of the resistance of up to 6% and compared the results with calculations of our collaboration partners.

In order to directly visualize the Néel vector reorientation, we performed photoelectron emission microscopy experiments with magnetic contrast combined with transport measurements. During this experiment, massive changes of the AFM domain pattern induced by current pulses were observed. Also the reorientation of the Néel vector induced by magnetic field pulse driven spin-flop transitions was correlated with magnetotransport measurements. Here, persistent changes of the resistance associated with anisotropic magnetoresistance and a transient drop of the resistance in the range of 2% were obtained.

These experiments demonstrated Néel vector switching in Mn_2Au both by a current induced Néel spin-orbit torque mechanism and by a magnetic field induced spin-flop transition. It was shown that the magnetoresistance of the antiferromagnetic domain walls in Mn_2Au plays a crucial role in the understanding of current-induced resistance modifications associated with Néel vector switching processes. Additional to transient effects, there are as well persistent resistance modifications induced by the Néel vector reorientation, which is an essential property for data storage applications.

Kurzfassung

In der auf antiferromagnetischen Materialien basierenden Spin-Elektronik wird der Néel Vektor, welcher der Untergittermagnetisierung entspricht, verwendet um Informationen zu speichern. In der Spin-Elektronik hat die Verwendung von Antiferromagneten als aktive Elemente mehrere Vorteile verglichen mit ferromagnetischen Materialien: Die intrinsische Spin-Dynamik von Antiferromagneten im THz Bereich ist von größter Bedeutung, da durch diese Eigenschaft prinzipiell ultraschnellens Schalten genauso wie die die Erzeugung und Detektion von THz Strahlung ermöglicht wird.

Weiterhin bewirkt die fehlende Netto-Magnetisierung von Antiferromagneten eine große Unempfindlichkeit der Orientierung des Néel Vektors gegenüber externen Magnetfeldern. Diese Eigenschaft bewirkt eine hohe Stabilität der gespeicherten Information, die durch externe Magnetfelder nicht zerstört werden kann. Darüber hinaus erzeugen Antiferromagnete keine Streufelder, die zur Begrenzung der minimal möglichen Größe einzelner Bits zur Datenspeicherung beitragen.

Allerdings stellt die gezielte Orientierung des Néel Vektors aufgrund der fehlenden Netto-Magnetisierung eine deutlich größere Herausforderung als die Manipulation des Magnetisierungsvektors von Ferromagneten dar. Ein Lösungsweg basiert auf strominduzierten Néel Spin-Bahn Drehmomenten, deren Auftreten für eine sehr spezifische Kristallstruktur von kollinearen Antiferromagneten vorausgesagt wurde. Nur zwei Antiferromagnete mit dieser Struktur sind bisher bekannt: Mn_2Au , das in dieser Arbeit untersucht wird, und CuMnAs .

Im Rahmen meiner Promotion habe ich die Wirkung von Strompulsen auf die antiferromagnetische Domänenstruktur von Mn_2Au untersucht, welche durch die von Néel Spin-Bahn Drehmomenten verursachten Orientierung des Néel Vektors und anderen Effekten modifiziert wird. Als alternative Methode zur Orientierung des Néel Vektors habe ich Magnetfeldpulse mit sehr großer Feldstärke eingesetzt, welche einen Spin-Flop Übergang erzeugen.

Um strominduzierte Néel Vektor Schaltvorgänge zu untersuchen, habe ich elektrische Transportmessungen eingesetzt: Ich habe strominduzierte Widerstandsänderungen von bis zu 6% gemessen und mir Berechnungen unserer Kollaborationspartner verglichen. Zur direkten Abbildung der Umorientierung des Néel Vektors haben wir Photoelektronen-Emissions-Mikroskopie mit magnetischem Kontrast verwendet. Im Rahmen dieser Experimente konnte eine deutliche strominduzierte Modifikation der Domänenstruktur beobachtet werden. Ebenso gelang es, die Magnetfeldpuls induzierte Ausrichtung des Néel Vektors mit elektrischen Transportmessungen zu korrelieren. Bei diesen Experimenten konnten stabile, durch den anisotropen Magnetowiderstandseffekt verursachte Widerstandsänderungen und relaxierende Widerstandsreduktionen im Bereich von 2% beobachtet werden.

Diese Experimente demonstrieren Néel Vektor Schalten in Mn_2Au sowohl durch strominduzierte Néel Spin-Bahn Drehmomente als auch durch magnetfeldinduzierte Spin-Flop Übergänge. Es wurde gezeigt, dass der Magnetowiderstand von Domänenwänden in Mn_2Au eine entscheidende Rolle zum Verständnis der strominduzierten Widerstandsänderungen spielt, welche mit Schaltprozessen des Néel Vektors assoziiert werden. Zusätzlich zu flüchtigen Effekten werden langzeitstabile Widerstandsänderungen durch eine Umorientierung des Néel Vektors erzeugt, was eine für Speicheranwendungen essentielle Eigenschaft darstellt.

Introduction

Antiferromagnets (AFMs) are a class of magnetic materials which exhibits no net magnetic moment in the absence of a magnetic field. At the same time, the pattern of individual magnetic moments in AFM is ordered, due to magnetic interactions favoring antiparallel orientation of neighboring magnetic moments. Antiferromagnets exhibit this type of spin arrangement below some critical temperature, named Néel temperature T_N . This class of materials was first described by Louis Néel [1, 2]. For his pioneering work on magnetism of solids including antiferromagnets, Louis Néel was awarded the Nobel Prize in 1970 [3]. Louis Néel described antiferromagnetic materials as *”extremely interesting from the theoretical viewpoint, but do not seem to have any applications”* [4]. This statement was based on the fact, that the zero net magnetization of antiferromagnets makes the manipulation as well as the read-out of the magnetic state difficult. However, for collinear antiferromagnets, it is straight forward to define a so called Néel vector, which corresponds to the staggered magnetization. In contrast to Néel’s statement cited above, this vector can be used to encode information. The novel field of AFM spintronics is based on this concept and promises significant advantages compared to conventional ferromagnetic spintronics. As mentioned before, AFM materials have no net magnetization, which makes it difficult to manipulate the Néel vector orientation. At the same time, the lack of net magnetization leads to superior stability of the magnetic state encoded in the Néel vector orientation. This property is very important for data storage applications.

Furthermore, AFMs are very attractive in terms of their high frequency dynamics, which is in the THz range [5]. This phenomenon makes AFM materials promising for fast switching of stored information and for THz device applications such as THz emitters [6] and detectors [7].

Last but not least, antiferromagnets do not produce stray magnetic fields, which limits the minimum feasible size of the data storage unit based on ferromagnets [8]. Nowadays, antiferromagnetic spintronics is a rapidly growing area of condensed matter

physics [9]. Many scientific groups around the world propose different ways of manipulation and read-out of magnetic states in antiferromagnets.

One of the newest and promising approaches for AFM spintronics is the manipulation of the Néel vector via current-induced Néel spin-orbit torques (NSOT). Reorientation of the Néel vector via NSOT requires special symmetries of crystal and magnetic structures. Only two compounds with the NSOTs required structure and type of magnetic ordering are known, including Mn_2Au . Additionally, the Néel vector can be manipulated by the application of sufficiently large magnetic fields resulting in a spin-flop transition. In the case of Mn_2Au at least 30T are required. This thesis investigates the manipulation of the Néel vector by current pulses with a magnitude of the order of 10^7 A/cm^2 and by magnetic field pulses with an amplitude larger than 30T.

My thesis is divided in the following seven chapters:

In **Chapter 1**, I describe the mechanism of the Néel Spin-Orbit torque in structures with locally broken inversion symmetry.

In **Chapter 2**, I give an overview of the experimental techniques used in this work for the characterization of the Mn_2Au thin films and for the visualization of the AFM domain pattern.

In **Chapter 3**, I describe the optimization of the growth conditions of the Mn_2Au thin films.

In **Chapter 4**, the visualization of the current-induced Néel vector manipulation in Mn_2Au microstructures is presented. The influence of the heating will be discussed in this chapter as well.

In **Chapter 5**, I show results of the visualization of the Néel vector reorientation in Mn_2Au by XMLD-PEEM for an as-prepared sample and a samples with a prealigned Néel vector.

In **Chapter 6**, I show the reorientation of the Néel vector by large magnetic field pulses.

In **Chapter 7**, I discuss the results obtained during this PhD project.

Chapter 1

Mechanisms of manipulation of Néel vector in antiferromagnets

In this chapter, I present a brief overview of some methods of the Néel vector manipulation in AFMs, focusing on the mechanism of Néel Spin-Orbit Torque (NSOT). Additionally, an overview of existing experimental realizations of the Néel vector switching in CuMnAs, presumably based on NSOTs, is given.

1.1 Methods of manipulation of the Néel vector in antiferromagnets

As was mentioned before, AFMs are robust to an external magnetic field. This property makes it very difficult to manipulate the Néel vector of antiferromagnets. Manipulation of Néel vector in antiferromagnetic and read-out of the Néel vector orientation are the key tasks of modern AFM spintronics. Finding mechanisms of manipulation of the Néel vector in AFMs is a challenging task. Significant progress was achieved within the last 15 years with many researchers investigating possible mechanisms of manipulation of Néel vector in different AFM compounds [10–12].

One of the first approaches for the Néel vector manipulation in antiferromagnets, which was investigated experimentally, is the reorientation of the Néel vector via exchange coupling with a ferromagnetic layer. This type of system is also known as the exchange spring [10]. The key phenomenon behind the manipulation of the antiferromagnetic state via exchange springs is exchange coupling between the ferromagnetic layer and the antiferromagnetic layer at the interface. In such structures, the application of an external magnetic field leads to an alignment of spins of the top FM layer along

the direction of the applied magnetic field. Due to exchange coupling between spins of the ferromagnetic layer and the antiferromagnetic layer, the spins on top of the AFM layer follow the magnetization of the FM layer in the external magnetic field. The figure below shows a schematic picture of the exchange spring.

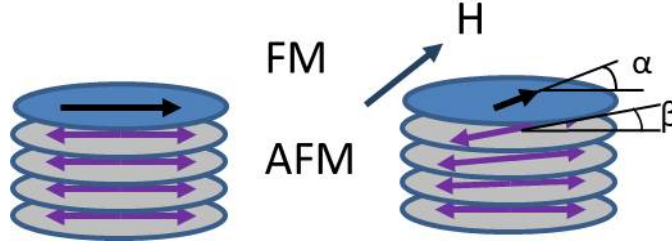


FIGURE 1.1: Schematic image of exchange spring structure in AFM/FM spin-spring system (adapted from ref.[10]).

This method was used experimentally for manipulating the Néel vector in antiferromagnetic insulating material NiO and ferromagnetic Co layer [10]. In this work the modification of the Néel vector of the top NiO layer induced by an external magnetic field was read out via X-ray circular magnetic dichroism measurements (XMCD). By application of the external magnetic field we can reorient the Néel vector in the top AFM layers.

The second method of Néel vector switching is the reorientation of the Néel vector in heterostructures with insulating AFM/heavy metal (HM) layers. This type of the Néel vector switching was realized only recently [13, 14]. In this type of structure, the top HM layer is used in order to inject a spin current into an antiferromagnetic layer, which leads to the presence of spin-orbit torque (SOT). As an example, L. Baldrati et al.[14], investigated current-induced effects in the multi-layer system of NiO(001)/Pt. In this work, switching of the Néel vector in NiO via SOT action on domain walls (DWs) was observed. In this work, current pulses were applied along two orthogonal directions in order to inject a spin current from Pt into NiO. Figure 1.2 b) shows an optical microscopy image of the structure used in this experiment. The reorientation of the Néel vector was identified via changes of the spin Hall magnetoresistance (SMR). The SMR is a resistance change in a bilayer system consisting of a magnetic layer and a HM with a large spin Hall angle and another magnetic material due to interaction of the spin current from heavy material and the magnetic layer. A more detailed description of this effect can be found in the work by H. Nakayama [15]. Figure 1.2 a) shows the value of the SMR recorded after the application of current pulses along perpendicular directions, showing a clear switching behavior of the SMR.

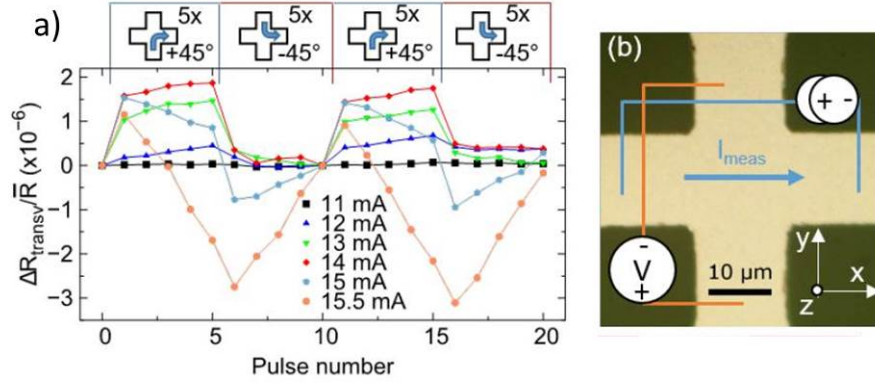


FIGURE 1.2: a) SMR signal in NiO/Pt system recorded after application current pulses along different directions. b) Scheme of the structure used in the experiment of Néel vector switching in the NiO/Pt system. Pictures taken from ref. [14].

One of the last approaches for the Néel vector reorientation, which was realized experimentally, is Néel vector manipulation via application of strain to AFM layer. As an example A. Sapozhnik et al. and Chen et al. realized experimentally reorientation of the Néel vector in AFM $\text{Mn}_2\text{Au}(001)$ by applying static strain [16, 17]. The manipulations of the Néel vector were read out via changes of the X-ray linear magnetic dichroism (XMLD). Changes of the Néel vector, in this case, are not persistent and Néel vector relaxes to its initial state at zero applied strain. However, stain-induced effects in AFMs is a rapidly growing area of spintronics and there is a possibility to discover a antiferromagnetic system in which applied stain leads to persistent changes on the Néel vector reorientation without relaxation at zero applied strain.

This Ph.D. work is focused on the concept of Néel vector reorientation via NSOTs, which is in principle possible in structures with locally broken inversion symmetry of magnetic sublattices. Investigation of the Néel vector switching via the NSOT mechanism is a rapidly growing area of modern spintronics. The reason for such intense interest of a large number of the scientific groups to such structures is the possibility to investigate new phenomena associated with the Néel vector reorientation process. Also, the Néel vector switching via NSOT can potentially be used in data storage applications due to fast natural spin dynamics in AFMs. The detailed description of the mechanism and structures, in which this mechanism can be applied, is discussed in the following section.

1.2 Manipulation of the Néel vector in antiferromagnets with locally broken inversion symmetry via Néel spin-orbit torque

The effect used in our work to switch the Néel vector orientation in Mn_2Au is known as Néel spin-orbit torque (NSOT). This type of torque allows reorienting the Néel vector in conductive antiferromagnets by the application of current pulses of high density. In general, the phenomenon of NSOT originates from the Rashba effect and two different magnetic torques acting on antiferromagnetic sublattices.

In order to understand the mechanism of NSOT, we first consider the Rashba effect. The Rashba effect is a phenomenon of momentum depend splitting of the electronic bands in systems with broken inversion symmetry. A 2D quantum well can serve as an example of such a system. For these systems we have to consider an electric field pointing along the direction of growth of a quantum well $E=E_z$. The resulting Hamiltonian for electrons in this 2D case can be described by the following Hamiltonian:

$$H_R = \frac{\mathbf{k}^2}{2m} + \alpha \mathbf{n}(\boldsymbol{\sigma} \times \mathbf{k}) = \frac{\mathbf{k}^2}{2m} + \alpha(\sigma_x k_y - \sigma_y k_x), \quad (1.1)$$

where \mathbf{k} is wave vector, $\boldsymbol{\sigma}$ is the Pauli matrix and α is the splitting constant, which is proportional to the electric field E_z .

If we consider now the Rashba term for electrons moving within the xy-plane, this term has opposite signs for electrons with a spin up and down. This leads to splitting of the electronic bands for these two states. In the simplest case of parabolic dispersion, the total electron energy can be represented by the following formula:

$$E(k) = \frac{\hbar^2 k^2}{2m} \pm \alpha k, \quad (1.2)$$

where $E(k)$ is the electron energy, α is the Rashba constant and \hbar is Planck's reduced constant. The sign of the additional energy term depends on the relative orientation of the electron spin and the wave vector.

As the result, the dispersion curves for electrons with spin up and spin down are splitted. Figure 1.3 shows the effect of the band splitting for electrons with spin up and spin down.

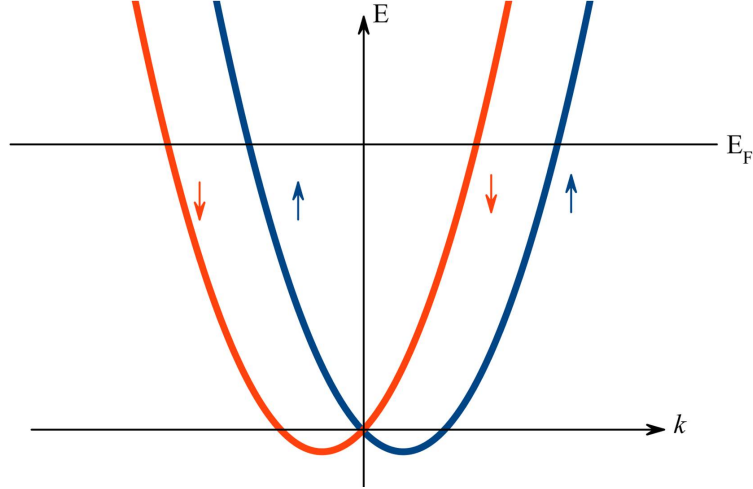


FIGURE 1.3: Splitting of the band of electrons with spin up and down.

Splitting of the electronic bands is a necessary part of the NSOT phenomenon. The mechanism of NSOT was first described by Zelezny et al. [18]. He considered the crystal structure of Mn_2Au , shown in figure 1.4. This material has an easy (001) plane and within this plane it has two easy axes parallel to the $[110]$ and $[1\bar{1}0]$ directions. If we look at the structure of Mn_2Au , we notice that the central Mn atom marked by red color has four neighboring gold atoms below and four neighboring Mn atoms above, while for the central Mn atom marked by blue color the situation is inverted. This phenomenon leads to the presence of staggered electric field along z direction, which is schematically shown in the image below.

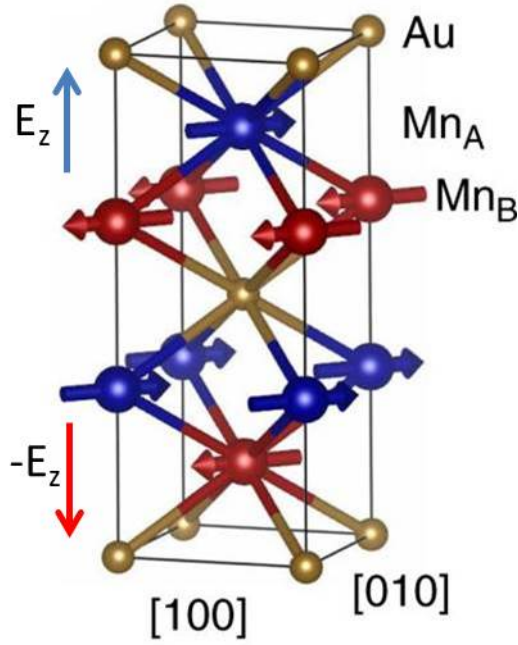


FIGURE 1.4: Crystal structure and magnetic structure of Mn_2Au . Red and blue arrows show schematically the direction of the staggered electric field E_z near Mn atoms.

Due to the presence of a staggered electric field in such systems, it is necessary to take into account the Rashba interaction for the electrons propagating through the crystal in the (001) plane. As mentioned before, the Rashba effect leads to a splitting of the electron bands. Figure 1.5 a) shows the schematic image of the corresponding Fermi surface shift due to the Rashba effect. The shift of the Fermi surfaces also can be considered as polarization of the electrons within AFM sublattices moving within the (001) plane. The polarized current can be represented as an effective magnetic field. Zelezny estimated the value of the effective magnetic field generated in Mn_2Au due to band splitting of electronic states with spin up and down. The following formula gives the value of the effective magnetic field generated within the magnetic sublattices A and B by an electric current in Mn_2Au [18].

$$\mathbf{B}^{A/B} \sim [\mathbf{M}^{A/B} \times (\hat{z} \times \mathbf{J})], \quad (1.3)$$

where \mathbf{B} is a field generated by spin-polarized current acting on the sublattices, \mathbf{M} is magnetization of sublattices A, B and \mathbf{J} is electric current.

Figure 1.5 b) shows the value of the effective magnetic field generated by the Rashba effect. Because the electric field in materials with local broken inversion symmetry is staggered, the effective magnetic field created by the electrons is also staggered. For the sublattices A and B the effective magnetic field has the opposite sign.

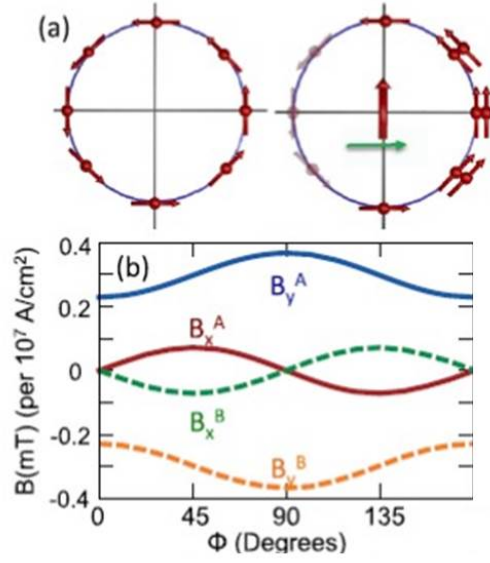


FIGURE 1.5: a) Schematics of the intraband inverse spin galvanic effect in a model Rashba system. b) Intraband NSOT field in Mn_2Au as a function of the in-plane spin-axis angle. The sublattice indexes A or B and the component of the field x, y, and z ([100], [010], [001]) are shown for each curve. Pictures taken from ref. [18].

Taking into account the fact, that the electric current induces an effective staggered magnetic field, which acts on the sublattices magnetization, we can now discuss the full mechanism of the NSOT. There are two types of torques involved in this process. When an electrical current is injected in such a system, following the mechanism described above, it gets partially polarized. This leads to the generation of the field like torque, discussed above, acting on the sublattices A and B. These effective magnetic fields are marked in figure 1.6 as H_a and H_b and the torques associated with this effective field are marked as τ_H . While acting, this torque tilts the magnetization of the sublattices out of plane (figure 1.6). In this configuration an exchange torque acts on the magnetic sublattices A and B. On the figure this torque marked as τ_E . The exchange torque acts as a field-like torque and rotates the magnetization of the sublattices by 90 degrees. Once the Néel vector is perpendicular to the applied current, the field-like torque generated by the current, which is tilting the magnetic moments out of plane, vanishes. Figure 1.6 shows the directions of the torques involved in the process of Néel vector switching.

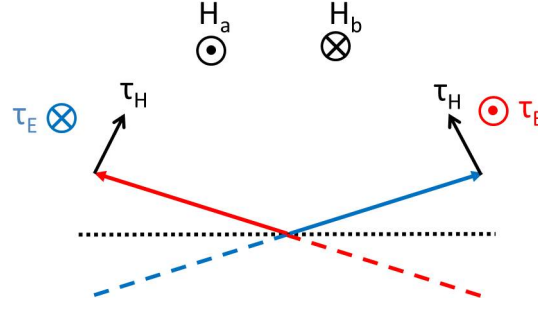


FIGURE 1.6: Schematic geometry of the NSOT. Blue and red arrows indicates magnetization direction of sublattices, τ_E is exchange torque, τ_H is field torques act of magnetic sublattices (adapted from ref. [9]).

Thus, in easy-plane antiferromagnetic materials with locally broken inversion symmetry and two orthogonal easy axes, the application of current pulses can flip the Néel vector by 90 degrees. Using experimentally determined values of the constants of anisotropy [19], Zelezny estimated a required current for the Néel vector reorientation in Mn_2Au , which is of the order of $10^8 - 10^9 \text{ A/cm}^2$. Changes of the Néel vector orientation can be read out via changes of resistance in transport measurements and via changes of the AFM domain pattern observed by XMLD-PEEM. Experimental results related to the manipulation of the Néel vector in Mn_2Au via NSOT will be discussed in the following chapters.

1.3 Manipulation of the Néel vector in antiferromagnetic CuMnAs

The reorientation of the Néel vector by the application of current pulses via NSOT was recently experimentally realized in the semimetallic antiferromagnetic compound CuMnAs [20, 21]. CuMnAs is a semimetallic antiferromagnetic compound with local broken inversion symmetry. Figure 1.7 a) shows crystal and magnetic structure of CuMnAs. This antiferromagnetic material has an easy plane (001) and within this plane, it has two easy axes that are parallel to the directions [100] and [010]. In such structures, we can expect the presence staggered effective magnetic field generated by the Rasha effect, as discussed above. In Ref. [20] an effective staggered magnetic field for CuMnAs was calculated. Figure 1.7 b) shows the calculated value of the effective magnetic field generated by the Rashba effect in CuMnAs.

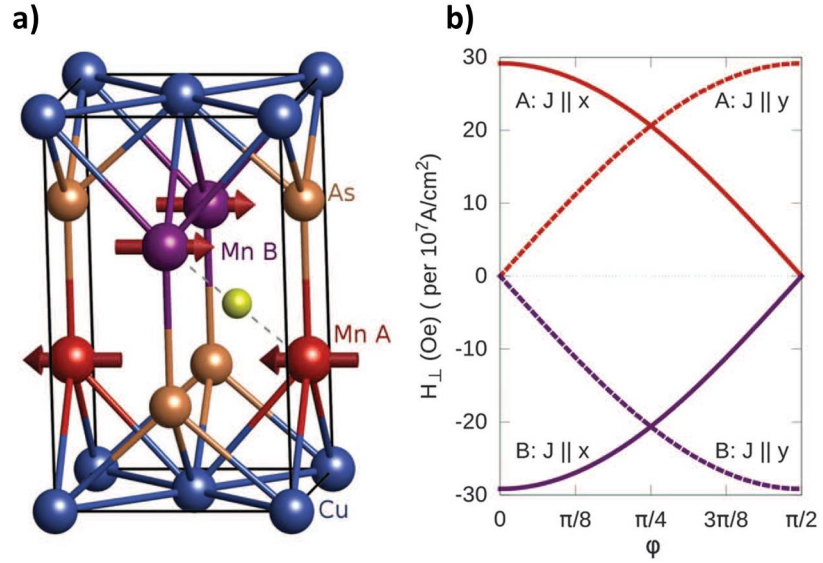


FIGURE 1.7: a) Crystal and magnetic structure of CuMnAs. b) Microscopic calculations of the components of the spin-orbit field transverse to the magnetic moments. Picture taken from ref. [20].

Following the idea of the Néel vector switching via NSOT, Wadley et al., performed transport experiments in CuMnAs. The authors patterned CuMnAs(001) thin-film into a cross structure with 8 legs. Two pairs of wires were used in order to inject current pulses along two easy axes ([010] and [100]). The other 4 wires were used to probe the resistance of the center of the cross structure. Figure 1.8 a) shows an optical microscopy image of the device and schematic of the measurement geometry.

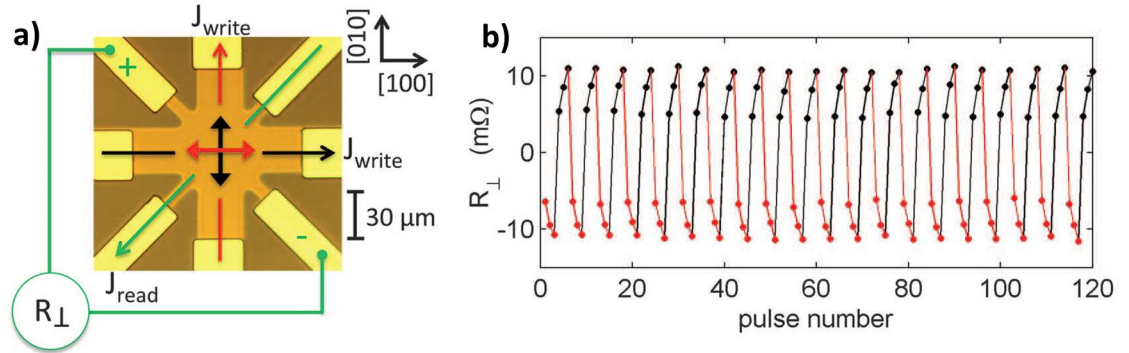


FIGURE 1.8: a) Optical microscopy image of the device and schematic of the measurement geometry. b) Value of transverse resistance recorded after application of current pulses along different crystal directions. Picture taken from ref. [20].

During their experiments, the authors applied current pulses along the easy axes of CuMnAs and measured transverse resistance value after each current pulse. Figure 1.8 b) shows the value of the transverse resistance recorded after the applying the current pulses along [010] and [100] crystal directions. In these experiments, current pulses with

a density $J=0.5 \times 10^7$ A/cm² and duration 50 ms were used. In the figure, it is visible that the application of current pulses along [010] crystal direction leads to a drop of the transverse resistance and application current pulses along [010] leads to the rise of the transverse resistance. The authors interpreted the changes of the transverse resistance as originating from the reorientation of the Néel vector in the central area of the cross structure.

This thesis is dedicated to the investigation of Néel vector manipulation in Mn₂Au (001) by the application of current pulses and by high magnetic field pulses (60 T). As was discussed before, Mn₂Au has a crystal and magnetic structure, which is expected to enable a reorientation of the Néel vector via the NSOT mechanism. Antiferromagnetic Mn₂Au and CuMnAs are the only known compounds with this property.

Antiferromagnetic Mn₂Au attracts the attention of many scientific groups due to its superior properties with compared to CuMnAs. The first advantage of Mn₂Au is its very high Néel temperature. Mn₂Au has a Néel temperature T_N of about 1500 K, while CuMnAs has $T_N=480$ K [20]. This property of Mn₂Au allows the operating of devices based on it in a wide range of temperatures. Also, such a high ordering temperature keeps Mn₂Au in the antiferromagnetic phase during electric current pulse injection with high current density. Thus, the high T_N makes it easier to separate temperature driven effects from intrinsic torques.

The second important advantage of Mn₂Au is its high conductivity comparing to CuMnAu. Antiferromagnetic Mn₂Au is a metallic compound with a specific resistance at room temperature $\rho \simeq 20$ $\mu\Omega\text{cm}$ [22], while CuMnAs is semimetallic compound with 8 times higher specific resistance value [20] ($\rho \simeq 160$ $\mu\Omega\text{cm}$). That leads to smaller heat dissipation in Mn₂Au during current pulses injection.

Another advantage of Mn₂Au is the fact that Mn₂Au is a non-toxic material. This fact makes this material easy to work with. Also, this property might be important for industrial applications.

In the following chapters, I describe the experimental realization of the Néel vector reorientation in Mn₂Au via application of current and field pulses.

Chapter 2

Experimental techniques used in this work

In this chapter I would like to present an overview of the experimental techniques used during my PhD project. I used magnetron sputtering to grow continuous epitaxial thin films of Mn_2Au . I varied the deposition temperature in order to optimize the quality of the Mn_2Au thin films. The crystal quality of the Mn_2Au thin films was examined by X-ray diffraction. To determine the surface quality of the Mn_2Au thin films I used atomic force microscopy (AFM) and scanning electron microscopy (SEM). X-ray magnetic linear/circular dichroism photoemission electron microscopy (XMLD/XMCD-PEEM) was used to visualize the domain pattern of Mn_2Au . In order to measure changes of resistance induced by the spin-flop transition, I performed transport measurements during the application of a magnetic field pulse. A brief description of this experimental technique is given in this chapter. Experiments on switching of the Néel vector were also performed using a room temperature tabletop transport setup. A description of this setup is given in this chapter.

2.1 Radio frequency magnetron sputtering

In order to grow epitaxial thin films of Mn_2Au I used radio frequency (RF) magnetron sputtering. Sputtering is a deposition process that falls under the category of physical vapor deposition. This technique serves mainly for the deposition of metallic thin films with a thickness smaller than $5\text{ }\mu\text{m}$. The basic principles of the sputtering deposition are illustrated in figure 2.1.

Sputtering deposition setups can be different in their design but the main principles are always the same. A bulk disk of the material to be deposited called target is bombarded by ions of the inert gas, which is in our case argon. In order to ionize the gas atoms in the chamber, an RF voltage is applied to the anode. When the ions of argon collide with the target, it leads to the injection of target atoms into the chamber volume. After that, the target atoms are deposited onto the substrate surface, where the target atoms form the thin film. Typically, the target is cooled by water [23]. In our case, I used magnetron RF-sputtering. In this configuration, there is a magnet below the target. The magnet confines electrons over the negatively charged target resulting in an increased ionization probability of the sputtering gas close to the target and by this confining the sputtering plasma. This results in a stable sputtering plasma already at relatively low sputter gas pressures.

In our case, the Mn_2Au thin-films were grown in 0.1 mbar Ar atmosphere from a single target with a stoichiometry ration of Mn to Au of 2:1. The UHV chamber includes a gate valve to control the argon pressure in the sputtering chamber during deposition. The sample holder has a heater and temperature sensor attached to it. The sample temperature can be set in a range between room temperature and 850°C . During the deposition I tuned the parameters such as the temperature of the sample and the power of the source in order to achieve better crystal and surface quality of the Mn_2Au thin films.

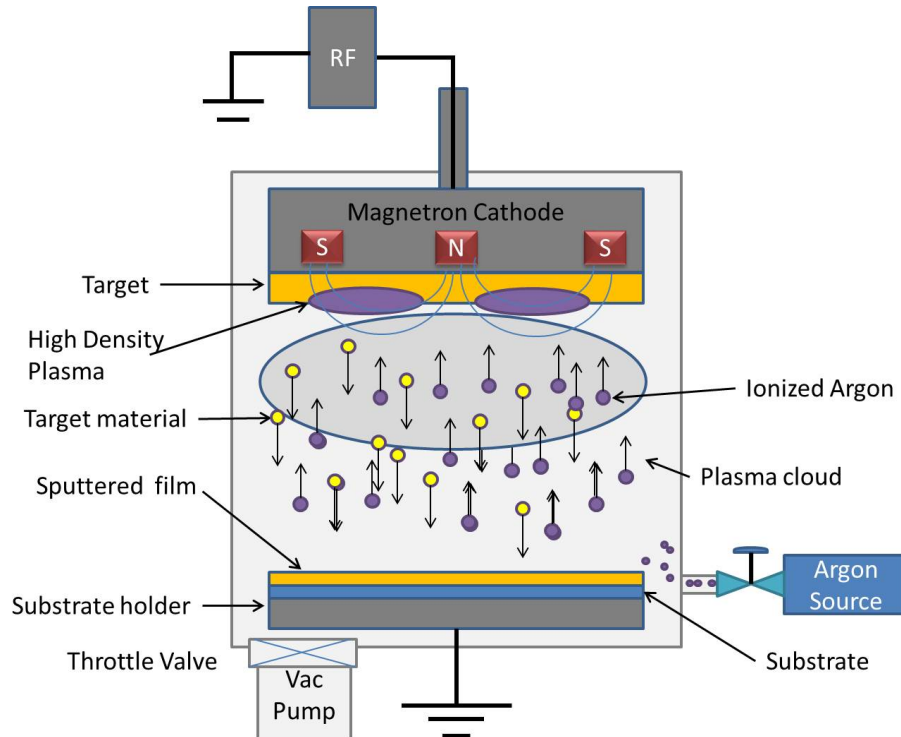


FIGURE 2.1: Scheme of the magnetron sputtering chamber.

The growth parameters at which the Mn_2Au thin films were deposited, can be found in chapter 3.

2.2 X-ray diffraction characterization

The main experimental technique which was used in this work in order to examine the crystal quality of Mn_2Au thin films, is X-ray diffraction (XRD). X-ray diffraction is an elastic scattering of x-ray from a periodic crystal structure. Figure 2.2 shows a scheme of the x-ray interference from planes of atoms in a crystal lattice.

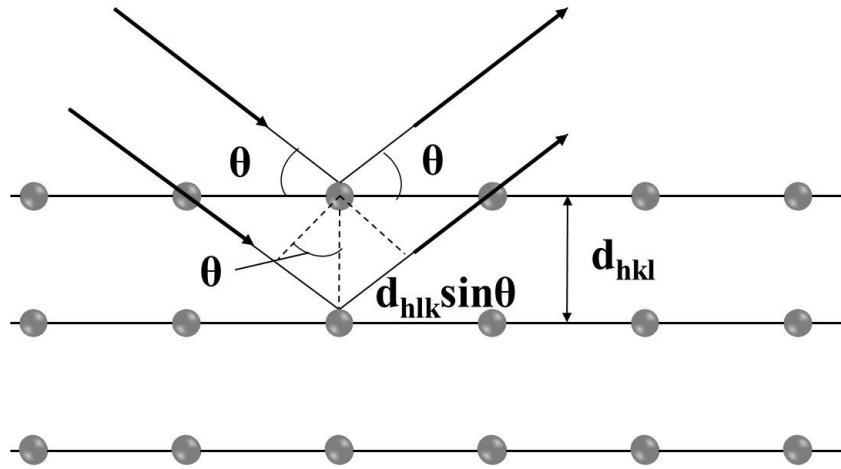


FIGURE 2.2: Scheme of reflection of the x-ray beam from the crystal lattice [24].

We consider an incident X-ray beam under an angle θ with respect to the crystal plane. The scattered monochromatic x-ray electromagnetic waves that are in phase give constructive interference in certain directions. The condition for constructive interference is given by Bragg's law:

$$2d\sin\theta = n\lambda, \quad (2.1)$$

where d is interplanar distance, λ is wavelength of the incident x-ray beam and n is a positive integer.

In order to investigate the crystal quality of the samples I performed experiments on the continuous films of Mn_2Au using a diffractometer Bruker D8 Discover. This x-ray diffractometer has as a source of monochromatic X-ray radiation an X-ray tube with a copper anode, which generates an incident x-ray beam with wavelength $\lambda=1,54 \text{ \AA}$. A common scheme of a diffractometer is shown in figure 2.3 a). The sample is placed in the center of a circle. The X-ray source and the detector can move on the circle stage.

The geometry in which the incident x-rays hit the sample surface under the angle θ and the detector measures reflected x-ray beam under 2θ is called $\theta/2\theta$. Figure 2.3 b) shows a schematic picture of $\theta/2\theta$ geometry. By tuning the angle θ , we can find such values of the θ angle at which Bragg's condition is satisfied. In this case, we observe peaks in the intensity which correspond to the crystal structures with a certain lattice constant.

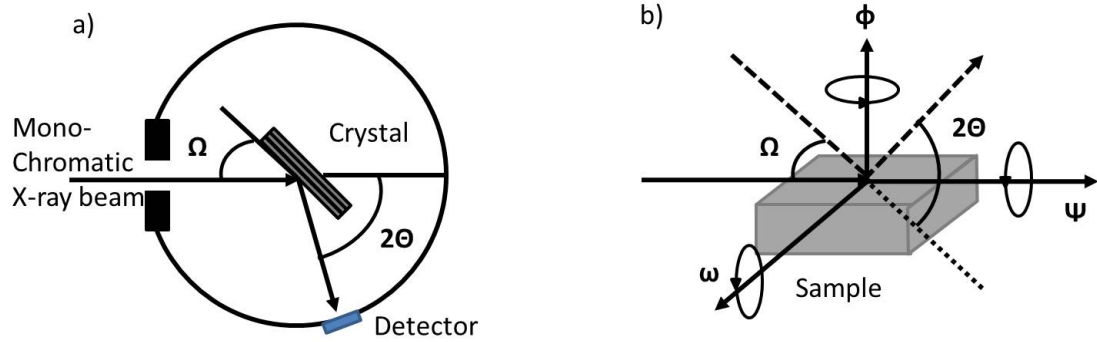


FIGURE 2.3: a) Schematic picture of a diffractometer setup. b) Illustration of the $\theta/2\theta$ geometry [24].

Using additional degrees of freedom it is also possible to probe lattice planes, which are tilted with respect to the sample surface. For example, it is possible to characterize the in-plane crystal order of the sample. For this we have to set $\theta/2\theta$ angles to the value which corresponds to an out-of-plane Bragg peak. Then, the sample surface is tilted to move the out-of-plane Bragg peak into the scattering plane. A rotation of the sample around its surface normal is now showing the in-plane order, i.e. epitaxy of the thin film sample.

Changing the ω angle we can also examine crystal quality. This type of scan is known as a rocking curve and characterizes the mosaicity of the sample, i.e. the spread of the tilting angles of the lattice vectors throughout the thin film. The width of this rocking curve can give us information about the degree of mosaicity of the sample [25]. Higher degree of mosaicity corresponds to higher broadening of the rocking curves. Figure 2.4 shows a schematic image of the broadening of the rocking curves due to mosaicity.

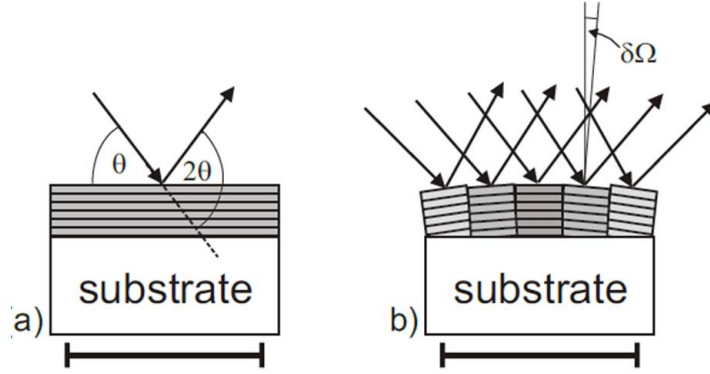


FIGURE 2.4: Scheme of mosaicity [24].

XRD is a powerful method for the characterization of the crystal quality. Crystal quality is one of the material parameters which defines the intrinsic resistance value of antiferromagnets, which is an important quantity for any transport measurement.

2.3 Scanning electron microscopy and atomic force microscopy

During this PhD project I used scanning electron microscopy (SEM) and atomic force microscopy (AFM) to examine the surface quality of the Mn_2Au samples. Figure 2.5 a) shows a schematic picture of SEM. An electron gun generates electron beam, which is accelerated by the negative high voltage in the range of 0.1-30 kV applied between the anode plate and the filament of the electron gun [26]. By tuning the high voltage, we can change the energy of the incident electrons. After passing the anode plate the electron beam will diverge. By using condenser lenses, the electron beam can be focused in a parallel beam. After that, the system of objective lenses focuses the electrons on the probe spot on the specimen surface.

The focused electron beam hits the sample at the specimen stage which can be moved in three directions. The focused electron beam produces electrons emitted from the sample, which are counted by a detector to generate an SEM image. This includes backscattered electrons, the Auger electron, secondary electrons, and characteristic x-ray radiation.

Modern conventional SEM machines can achieve a spatial resolution of about 1 nm [27]. There is one main requirement for the samples in order for them to be investigated by using SEM. The samples need to be conductive. The non-conductive samples have to be covered by a conductive coating layer before the measurements.

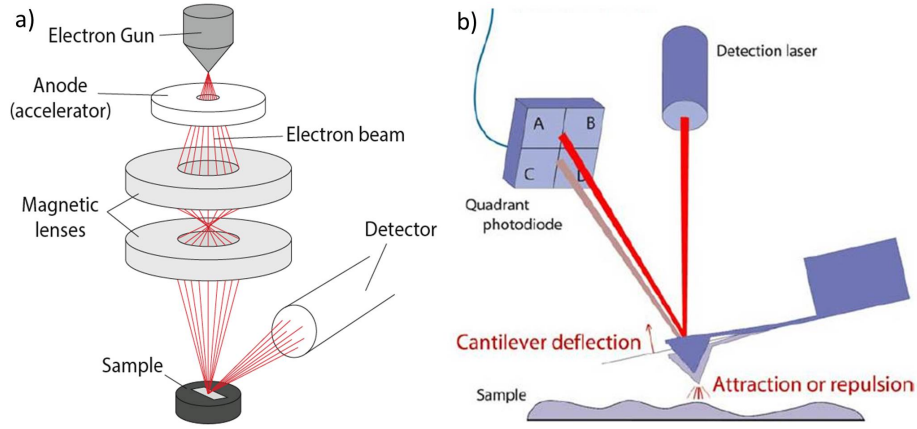


FIGURE 2.5: a) Schematic image of SEM. b) Schematic image of AFM [29].

The second experimental technique used in this work to examine surface quality of the Mn_2Au thin films is atomic force microscopy. Atomic force microscopy is scanning probe microscopy which allows to achieve a spatial resolution of a few angstroms. Atomic force microscopy is based on scanning of the sample surface by the tip of the cantilever. A schematic image of scanning geometry is shown in figure 2.5 b). Piezoelectric elements in the AFM setup serve to the purpose of accurate and precise movements of the cantilever tip in the xy-directions. From the backside, the cantilever is illuminated by a laser beam reflected onto a detector with four segments. The tip of the cantilever experiences the repulsive or attractive interaction with the surface of the sample arising from electromagnetic interaction between the tip of the cantilever and the sample's atom. By scanning the sample's surface line by line we can build its full image. In this PhD work atomic force microscopy was used in order to examine surface roughness of the sample, additionally to the SEM measurements.

2.4 The experimental setup for the transport measurements

To identify changes of the Néel vector orientation induced by the electric current pulses I performed transport experiments on Mn_2Au microstructures. As it is known, the antiferromagnetic order in metallic materials leads to the presence of the anisotropic magnetoresistance (AMR). This phenomenon can be seen as a different longitudinal resistance value while measuring resistance along different directions with respect to the Néel vector. This asymmetry arises from a different scattering probability for the electrons propagating under different angles with respect to the Néel vector [30]. Additionally to that, we can see the current Néel vector reorientation as the changes of the transversal resistance.

Following the mechanism of the current-induced Néel vector switching described in chapter 1, I performed transport experiments on the current-induced Néel vector re-orientation in Mn_2Au . For my experiments on the Néel vector switching I used Keithley 2430 as a source of current pulses. This device allows applying current pulses with the amplitude up to 10 A and total power up to 1 kW per pulse. In order to probe changes of the Néel vector orientation I measured the longitudinal and the transversal resistance before and after applying the current pulses. To measure the value of the sample resistance I used Keithley 224 as the current source and Keithley 2182A nanovoltmeter to probe the voltage. Keithley 2430 was connected to the sample via the Keithley 705 multiplexer unit. The multiplexer unit allows switching the connected devices between different channels. The setup was controlled by a LabVIEW based software. Figure 2.6 shows a schematic image of the transport setup used for the Néel vector switching experiments. The results of the transport experiments on the current induced Néel vector switching are described in chapter 4.

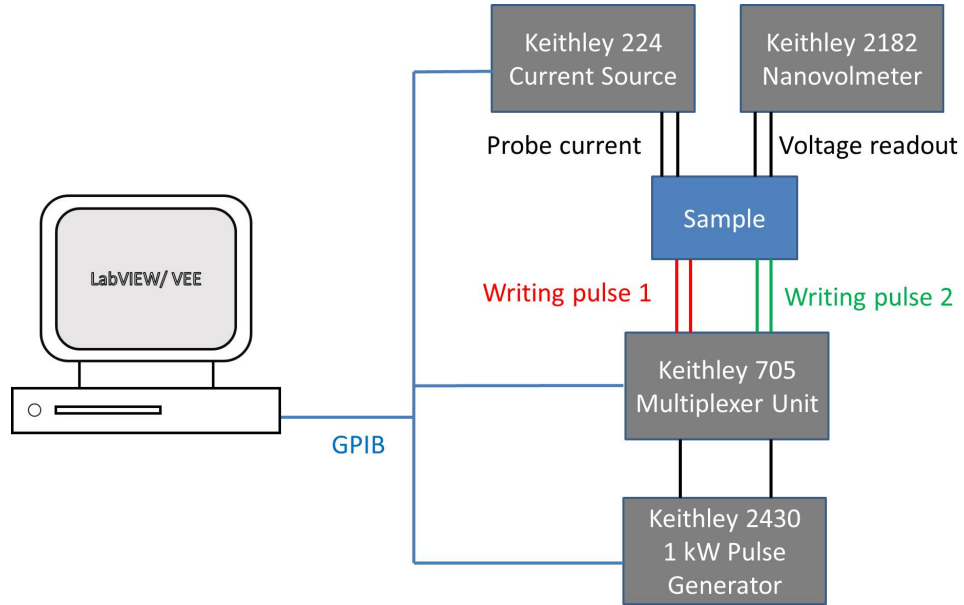


FIGURE 2.6: Scheme of the experimental setup used for the Néel vector switching experiment.

2.5 High magnetic field pulse cryostat

To investigate the phenomenon of the reorientation of the Néel vector induced by the pulses of the high magnetic field I performed electric transport experiments using a magnetic pulse cryostat. As it was shown in our recent work [31], the reorientation of the Néel vector in Mn_2Au can be achieved by the application of magnetic field above 30 T. That is quite a high magnetic field that can not be achieved in standard DC

magnetic cryostats. Usually, conventional lab-based cryostats allow applying a continuous magnetic field up to 16 T [32]. If you require a higher magnetic field for your experiments, they have to be performed using pulse magnetic cryostats. Dresden High Magnetic Field Laboratory (Helmholz Zentrum) provides an opportunity to apply magnetic field with an amplitude up to 70T using a pulse magnetic cryostat. The figure below shows the schematic image of the magnetic cryostat. The sample holder has a temperature sensor attached to it. This allows monitoring the temperature during the experiments. By mounting a sample heater, the measurements could be performed in a range of temperatures from 4 K up to 300 K. In our case, in order to achieve the best possible temperature stability all experiments were performed at liquid He temperature 4K.

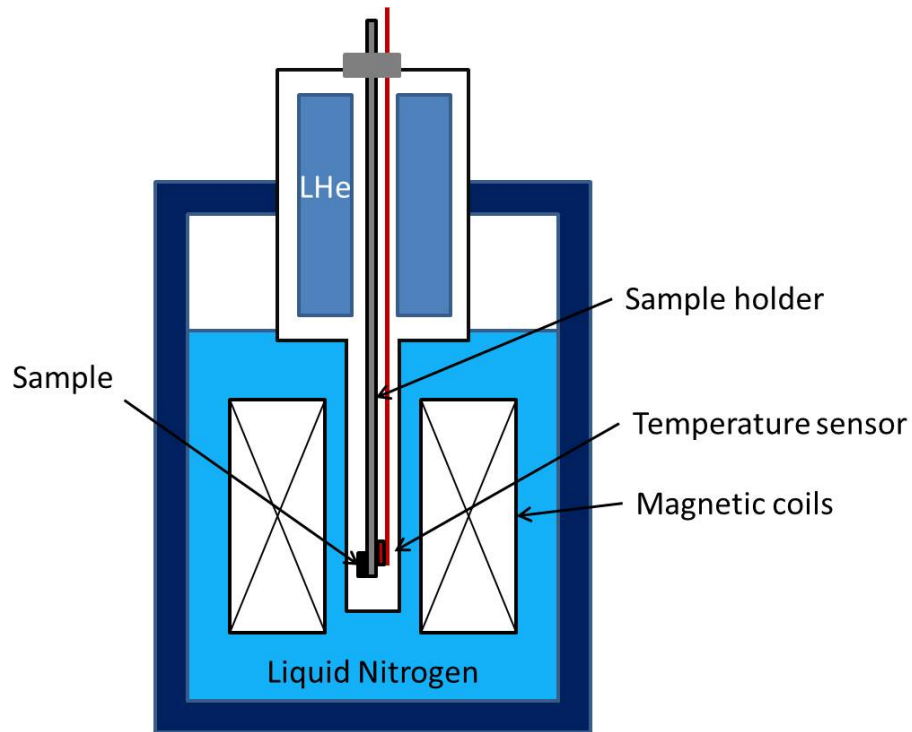


FIGURE 2.7: Schematic picture of the magnetic cryostat.

The pulse magnet is based on copper coils which are cooled to the temperature of 77 K. A capacitor bank allows to apply the pulses of high voltage up to 22 kV, which generate the current pulses of 30 kA. The high voltage pulse applied to the copper coils, induces the pulse of the high magnetic field with a fixed pulse duration of 150 ms. After each pulse of the high magnetic field there is waiting time of approximately four hours which is required before the next field pulse in order to cool down the copper coils. Figure 2.8 shows the time profile of the magnetic field pulse.

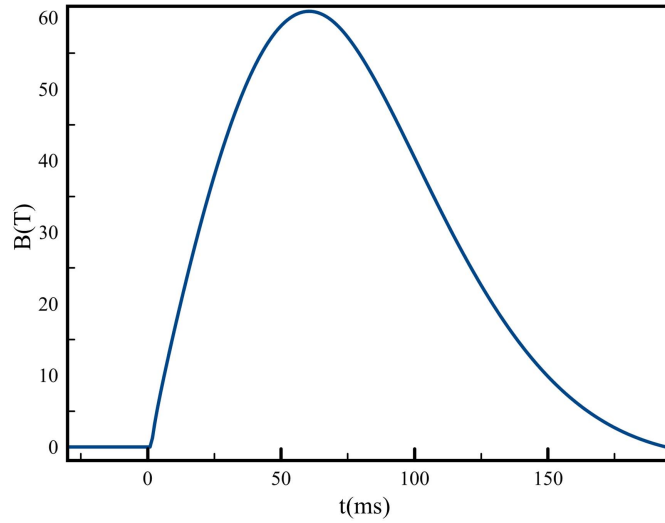


FIGURE 2.8: Value of magnetic field recorded while applying a pulse of the high magnetic field.

2.6 X-ray Magnetic Linear/Circular Dichroism Photoemission Electron Microscopy

The main experimental technique which was used during this PhD work for the visualization of the antiferromagnetic domains is x-ray magnetic linear/circular dichroism photoelectron emission microscopy (XMLD/XMCD-PEEM). XMLD/XMCD uses the differential absorption of horizontal and vertical linear/circular polarized light in a magnetic sample in order to examine magnetic materials and their properties. These experiments have been performed at large scales synchrotron facilities such as the Diamond Light Source (United Kingdom) and BESSY II (Germany).

The synchrotron radiation is an electromagnetic radiation emitted from the electrons which are accelerated radially. While being accelerated by the magnetic field electrons emit photons. This type of the electromagnetic radiation can be produced in synchrotrons using bending magnets, undulators and/or wigglers. Synchrotron light sources typically consist of three parts in it. The first part is a linear accelerator and a booster ring, which are used to accelerate the electrons to the energy, typically 1-3 GeV, at which they can be injected into a storage ring. The second part is the storage ring where the kinetic energy of the electrons is kept constant. The third part is beamlines with experimental setups. Synchrotron electromagnetic radiation covers a wide range of energies from microwave to hard x-ray with photon energy up to 30 KeV. Figure 2.9 shows a schematic picture of a research synchrotron facility.

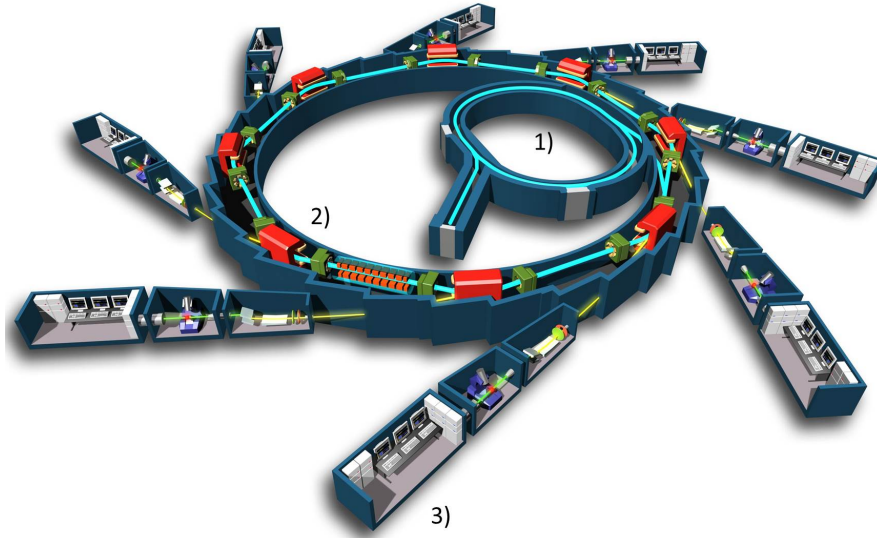


FIGURE 2.9: Schematic image of synchrotron facility. 1) Booster ring, 2) storage ring and 3) beamlines [33] .

The polarization of the synchrotron radiation can be set as linear or curricular. During experiments we can set the energy of X-ray photons. Synchrotron radiation has a high degree of monochromaticity. At the beamline I06 at Diamond Light source, where most of the X-PEEM experiments were carried at the energy range of X-ray between 300 eV and 800 eV with an energy resolution of 0.3 eV.

The synchrotron radiation is required to enable many techniques such as diffraction, holography and spectroscopy. During my PhD project I used the X-ray Photoemission Electron Microscopy (X-PEEM) in order to visualize antiferromagnetic domains of Mn_2Au . Figure 2.10 shows a principal scheme of a X-PEEM setup. A sample is illuminated by a focused X-ray beam. The X-ray photon excites electrons from a different core levels to the Fermi level depending on the X-ray photon energy. High voltage (12 kV) is applied between the sample and the objective lens to extract the photo-excited electrons from the sample. Then the objective magnetic lens collects the electrons from the sample and move them through an electron column with the system of the magnetic lenses. After that, the electrons are projected on a screen. Depending on the configuration of each particular X-PEEM setup it can have some additional devices attached to it such as a spin filter, electron energy analyzer, etc .

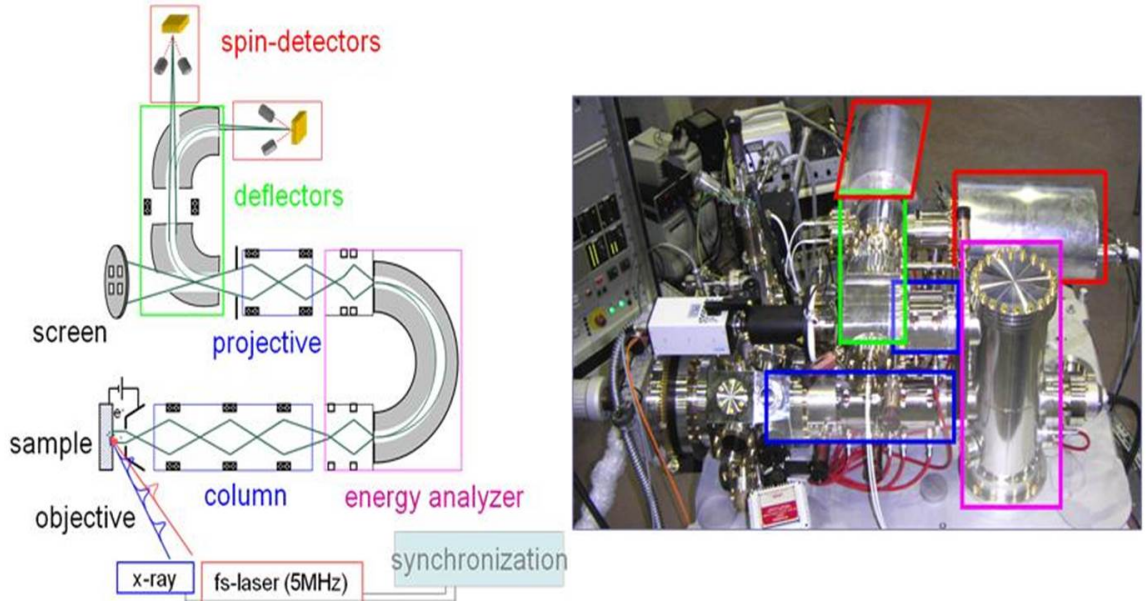


FIGURE 2.10: Schematic image and a photo of the X-PEEM setup on BESSYII [34].

2.6.1 X-ray absorption spectroscopy

As it was mentioned before, electrons can be excited resonantly from different core levels to the Fermi level by X-ray photons with different energies. The energies, which correspond to these transitions, are unique for different elements [35]. This also includes magnetic materials such as Co, Fe and Mn. Figure 5.2 a) shows a scheme of the electron transitions from the different core levels to the Fermi level. There are abbreviations, which correspond to different transitions, such K edge, which corresponds to transition from the 1s state to the Fermi level.

The experiments on XAS were performed on a large number of materials. Nowadays, the energies of the electron transition for different materials are tabulated and can be found in a handbook of spectroscopy (see ref. [36]). Figure 5.2 b) shows X-ray absorption spectra for L_2 and L_3 transitions for Fe, Ni and Co. Oxidation of the materials leads to broadening of the X-ray absorption lines and also to the presence of the additional peaks. The experiments on XAS can give us a lot of information about the material properties such as oxidation of the material, the chemical composition of the sample, etc.

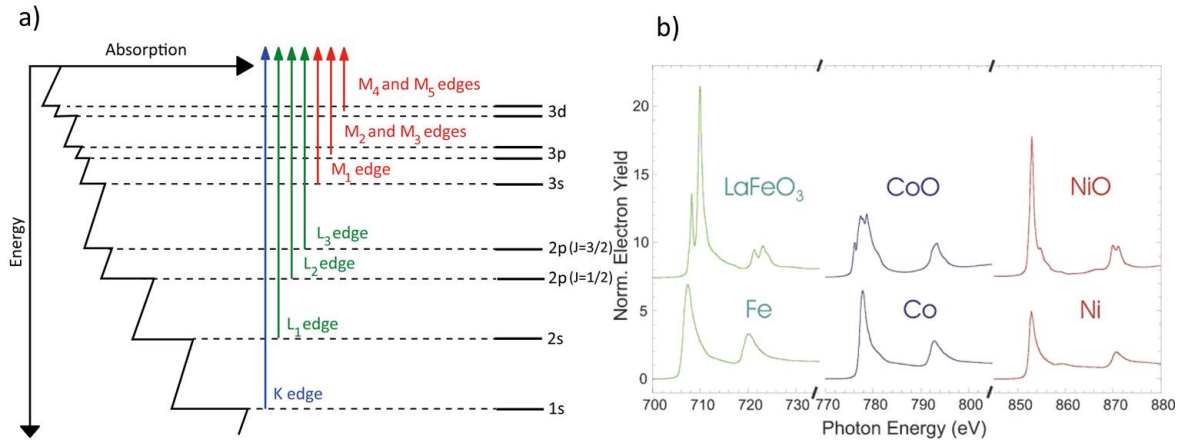


FIGURE 2.11: a) Schematic representation of the electron transition from different core levels to the Fermi level [37]. b) X-ray absorption of different materials [38].

In order to achieve the best accuracy the experiments on XAS should be performed on the spectroscopic beamlines. Nevertheless, the X-ray absorption spectra could be measured using X-PEEM. By tuning the energy of the incident X-ray beam we can acquire images at these energies. After that we can integrate the total intensity of each image and restore a resulting X-ray absorption spectra. During our experiments on X-PEEM, the X-ray absorption spectrum was measured for each Mn₂Au sample in order to examine the sample surface on oxidation.

2.6.2 X-ray circular magnetic dichroism

In order to visualize the ferromagnetic domain structure of bilayer system Mn₂Au/Fe I used the XMCD-PEEM method. In general, the XMCD is a phenomenon of absorption asymmetry of X-ray photons with different circular polarization in ferromagnetic materials.

In contrast to the paramagnetic materials, in ferromagnetic materials there is an asymmetry of the electrons with a spin up and down on the Fermi level. Presence of net magnetization in ferromagnetic materials leads to the exchange splitting of the electronic bands with a spin up and down on the Fermi level (figure 2.12 a) and b). This results in a different number for the electrons with spin up and down as well as in a different number of electronic states on the Fermi level for electrons with a spin up and spin down.

In order to measure the difference in number of d electrons with a spin up and spin down, we need to make the process of the x-ray absorption spin depend. That can be done via the excitation of the photoelectrons by the circularly polarized x-ray photons,

which transfer angular momentum $l=1$. According to the dipole selection rules, transitions between states are only allowed in case if the following requirements are fulfilled: $\Delta m_l = \pm 1$ and $\Delta m_s = 0$, where Δm_l is an angular momentum quantum number and Δm_s is spin quantum number. This is the case for the p-d electron transitions in ferromagnetic materials.

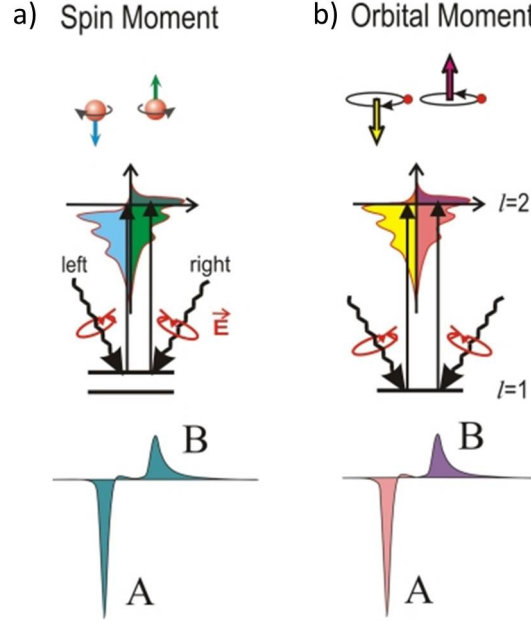


FIGURE 2.12: a) and b) illustrated electron transitions in a one-electron model. The transitions occur from the spin-orbit split 2p core shell to empty conduction band states [40].

If requirements for the angular momentum are fulfilled, we can calculate the probabilities for the allowed transitions from the p- to d-states. The probability for the allowed p-d electron transitions can be described by the following relation:

$$P_{i \rightarrow f} \sim |\langle f | H | i \rangle|^2 \rho_f, \quad (2.2)$$

where P is the transition probability, i and f the initial and the final states and ρ_f is density of the final states.

The final states are the electronic states on the Fermi level which have non equal density of state for electron with a spin up and down. As the result, a number of photo excited electrons in FM depends on the helicity of the X-ray photons. This was observed experimentally both in the experiments on the XMCD-PEEM and in the spectroscopic experiments. In this work this phenomenon was used in order to visualize ferromagnetic domains in the $\text{Mn}_2\text{Au}/\text{Fe}$ multilayer samples. The results of these experiments are described in chapter 6.

2.6.3 X-ray linear magnetic dichroism

In antiferromagnets the XMCD technique is not applicable due to a lack of net magnetization in antiferromagnetic materials. That means that there is no asymmetry of DOS for the electrons with spin up and down on the Fermi level.

In antiferromagnets spins are coupled antiparallel. The presence of spins and their antiparallel arrangement modifies the electronic state on its own. We can consider this phenomenon on the example of a cubic antiferromagnetic material NiO [40].

Due to cubic symmetry, the charge distribution around the Ni atoms in paramagnetic state is spherical. In this configuration there is no X-ray linear dichroism. Below T_N (520 K) in antiferromagnetic phase Ni spins are aligned antiparallel within the (111) plane. The presence of the antiferromagnetic order breaks the spherical symmetry of the charge distribution in the cubic potential via spin-orbit coupling [40]. In antiferromagnetic state the charge distribution is elongated along the spins direction. Insert of the figure 2.13 shows the charge distribution in NiO below and above T_N .

As the result, the absorption of light will depend on the relative orientation of the charge distribution and the polarization of the X-ray beam due to a matrix element, which defines the transition probability (see formula 2.4), has different values for the different angles between X-ray photon polarization and the Néel vector. Figure 2.13 b) shows the X-ray absorption spectra NiO near L_2 , L_3 edges measured for two orientations of the X-ray polarization and the Néel vector.

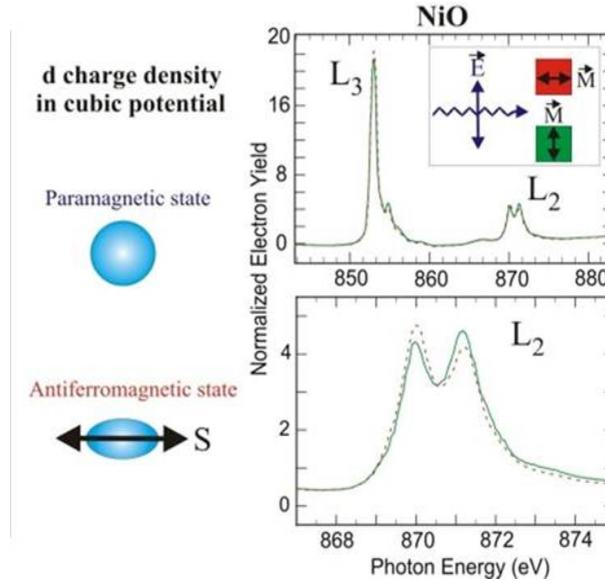


FIGURE 2.13: Origins of the XMLD in NiO. In the paramagnetic state the absorption spectrum of NiO does not exhibit a polarization dependence because of the cubic symmetry. In the antiferromagnetic state the spin-orbit coupling leads to a distortion of the charge density and an XMLD effect is observed. That leads to the asymmetry in XAS for two orientations of the X-ray linear polarization [40].

Due to a lack of the net magnetization, imaging of the AFM domains is not a trivial task. During this PhD work, the XMLD-PEEM technique was used as the main imaging technique to visualize the AFM domains in Mn_2Au . The experiments on the XMLD-PEEM also allowed us to visualize the Néel vector reorientation induced by the applied current pulses and pulses of high magnetic field. Results of the AFM domain visualization in Mn_2Au are shown in chapter 5 and 6.

Chapter 3

Sample preparation

In this chapter, I give an overview of the growth process of the Mn_2Au (001) thin films and the patterning of microstructures using optical lithography. All samples were grown from a single Mn_2Au target using RF-sputtering. It is important to control material parameters by changing the growth parameter, because many intrinsic properties of Mn_2Au thin films also affect the Néel vector manipulation process. For example, the value of AMR depends not only on the magnetic properties of the material but also on material properties such as the intrinsic resistivity. Therefore, it is important to have Mn_2Au thin films of good crystal quality in order to achieve the highest possible AMR signal. Another important material parameter that plays a crucial role in observation and visualization of AFM domains, is the morphology of the Mn_2Au thin films. By using different growth parameters, we can control the surface roughness of the samples.

3.1 Optimization of crystal quality of the Mn_2Au thin films

As a means to deposit Mn_2Au on Al_2O_3 ($1\bar{1}02$) (R-cut) substrates, I used Ta (001), 10 nm buffer layers. Ta buffer layers were used to satisfy the lattice matching and symmetry conditions. Tantalum has a cubic symmetry with the lattice constant $a=3.310 \text{ \AA}$, while Mn_2Au has a tetragonal crystal structure with the lattice constants $a=3.328 \text{ \AA}$ and $c=8.539 \text{ \AA}$. Ta layer was deposited on the R-cut sapphire substrate at 700°C at the argon pressure 0.03 mbar. Antiferromagnetic Mn_2Au was deposited on top of the Ta buffer layer at the different temperatures in the range $500\text{-}700^\circ\text{C}$. The deposition of Mn_2Au at lower or higher temperature leads to a significant reduction of crystal quality. The argon pressure during the deposition of Mn_2Au for all samples was persisted at a level of 0.1 mbar. The power of the RF power source was set to 20 W for the Ta deposition and 25 W for the Mn_2Au deposition. At these conditions the deposition rate

of Mn_2Au is around 8.9 nm per minute. This allowed us to grow 80 nm of Mn_2Au within approximately 9 minutes. All samples were capped by a Ta or Al capping layer to prevent the oxidation process. Figure 3.1 shows the XRD $\theta/2\theta$ scan of the Mn_2Au sample grown on Ta buffer layer. In this scan we can see few peaks. The first peak at $2\theta=20.78^\circ$ corresponds to the lattice constant of 8.5 Å, which corresponds to (001) phase of Mn_2Au . We also can see diffraction peaks of a higher order approximately at $2\theta=42.4^\circ$ and $2\theta=64.8^\circ$. Additionally to the (001) phase peaks, we can see a diffraction peak at $2\theta=28.3^\circ$ which corresponds to (101) phase of Mn_2Au .

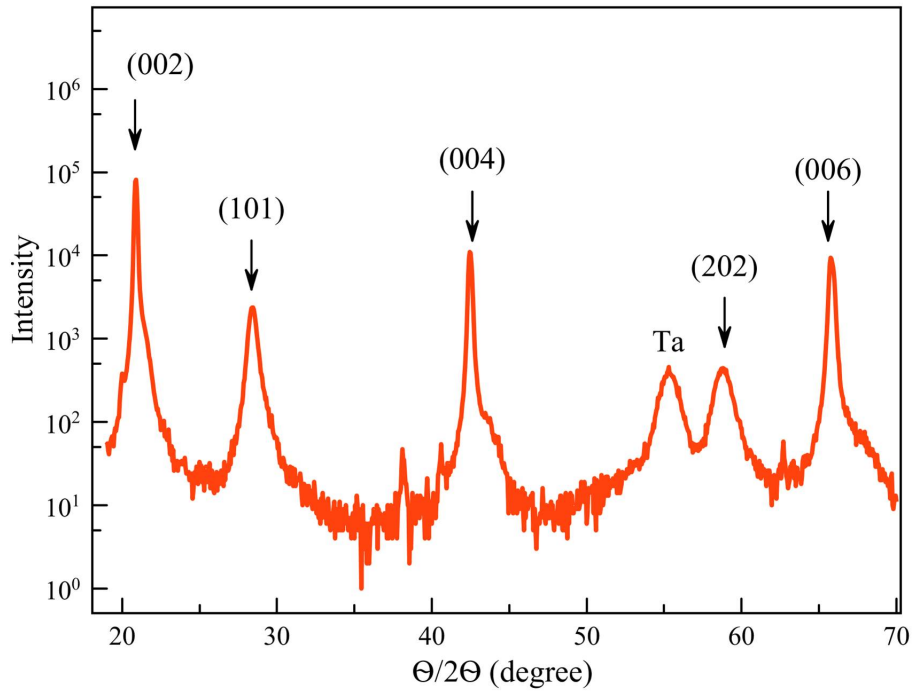


FIGURE 3.1: $\theta/2\theta$ scan of Mn_2Au thin films grown at 550°C on R-cut sapphire with the Ta buffer layer.

During the growth optimization process we aimed at improving two parameters associated with crystal quality of Mn_2Au thin films. The first parameter is the ratio of the areas under the peaks in $\theta/2\theta$ scan which correspond to (001) and (101) crystal phases. This ratio can be changed from 10 for the sample grown at 700°C and to 100 for the sample grown at 500°C . The second quantitative parameter of the thin-film quality, which we optimized, is the rocking curve width of (001) Mn_2Au crystal phase. Figure 3.2 shows the rocking curve of the 80 nm Mn_2Au thin films grown at different temperatures.

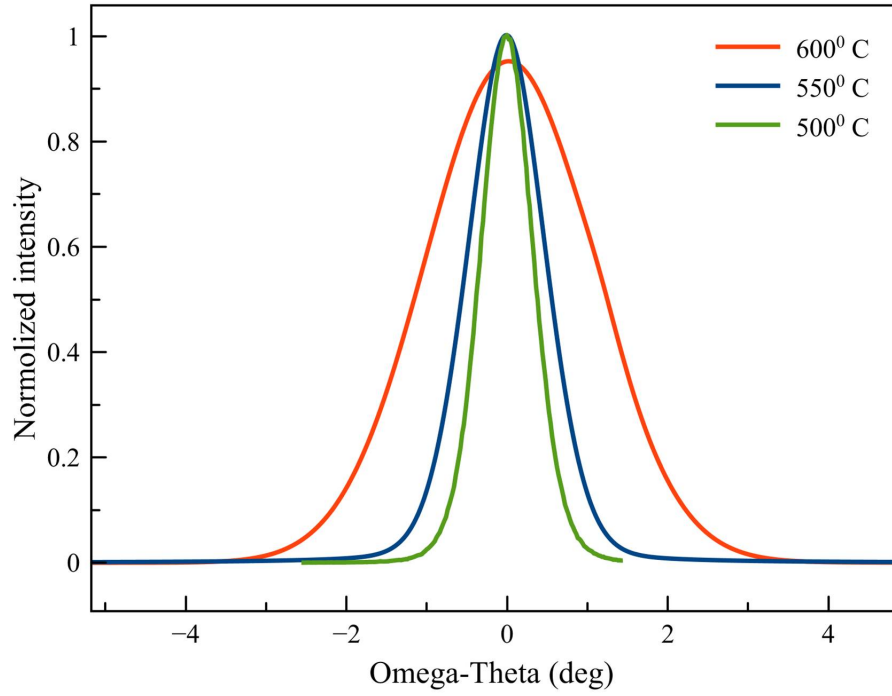


FIGURE 3.2: Rocking curves of Mn_2Au grown at different temperatures.

We can see that the narrowest rocking curve is associated with the sample, which was grown at 500°C . The sample grown at this temperature shows a full width at half maximum of the rocking curve of about 0.5 degrees, while the sample grown at 600°C shows the rocking curve with a width of 1.4 degrees. Broader rocking curves correspond to the presence of a higher degree of mosaicity of the (001) phase of Mn_2Au .

I also measured the rocking curve position of the (001) phase of Mn_2Au for the 0 degree orientation and for 90 degrees rotated with respect to the first orientation. Two rocking curves, which are related to two sample orientations, are separated by 3 degrees. This is an indication of the fact that the (001) crystal planes of Mn_2Au are tilted with respect to the $(1\bar{1}02)$ crystal planes of the sapphire substrate. Figure 3.3 shows the rocking curves of the (001) phase of Mn_2Au thin film measured for two different orientations of the sample. This tilt of the (001) plane of Mn_2Au can create asymmetry between two orthogonal $[110]$ and $[\bar{1}\bar{1}0]$ crystal directions.

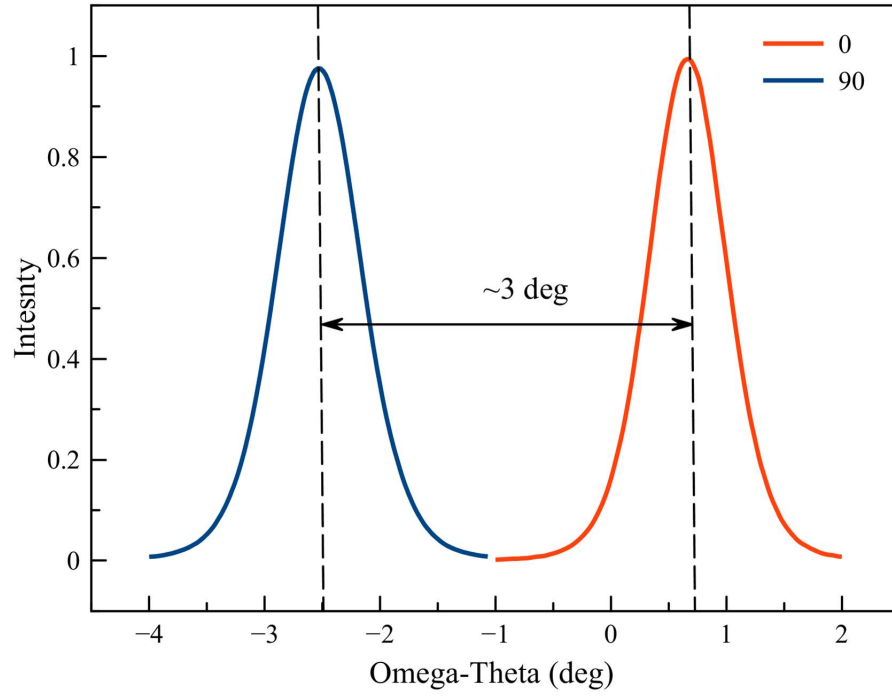


FIGURE 3.3: Rocking curves of the Mn_2Au thin film measured at the different in-plane orientation of the sample. Red and blue curves indicate rocking curves for two orientations of the sample rotated by 90 degrees around the sample normal.

The in-plane crystal order of the samples was determined from the XRD φ -scans. The figure below shows an in-plane φ -scan of a 80 nm Mn_2Au sample grown on the R-cut sapphire substrate with 10 nm of Ta as a buffer layer.

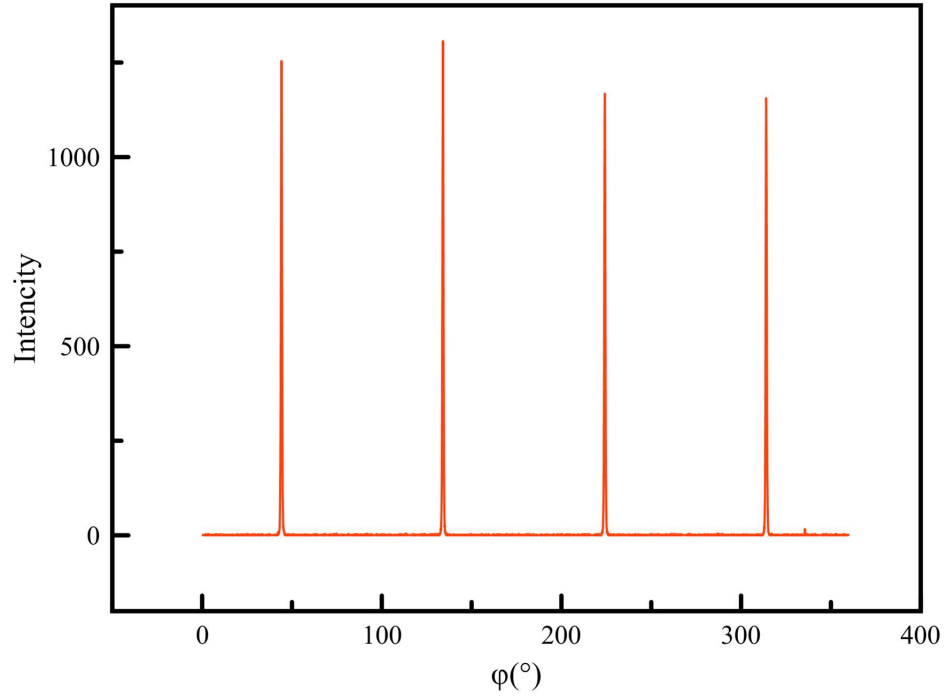


FIGURE 3.4: In-plane XRD φ -scan of 80 nm Mn_2Au thin film.

Optimization of the crystal quality of the Mn_2Au thin films is an important step in sample preparation for further transport experiments. As it was mentioned before, the crystal quality defines the intrinsic resistance value, which is important for the transport experiments, particularly for experiments involving pulses with high current density. Lower resistance allows injecting higher current with lower dissipation associated with Joule heating.

3.2 Optimization of the morphology of the Mn_2Au thin films

Another important property of Mn_2Au thin films, which we aimed to control via changing growth parameters, is morphology. Morphology can have an influence on the antiferromagnetic domain pattern. Moreover, very pronounced morphology can affect the transport properties of the sample via the presence of inhomogeneous current distribution across the sample. From the experimental point of view, strong morphology creates difficulties for observation of the antiferromagnetic domains in Mn_2Au .

I examined the samples grown at the different deposition temperatures. Figure 3.5 shows the SEM and atomic force microscopy images of the sample grown at 700°C .

It can be noticed that this sample grown under conditions mentioned above shows quite a pronounced morphological pattern. The 80 nm sample has a roughness of 30 nm.

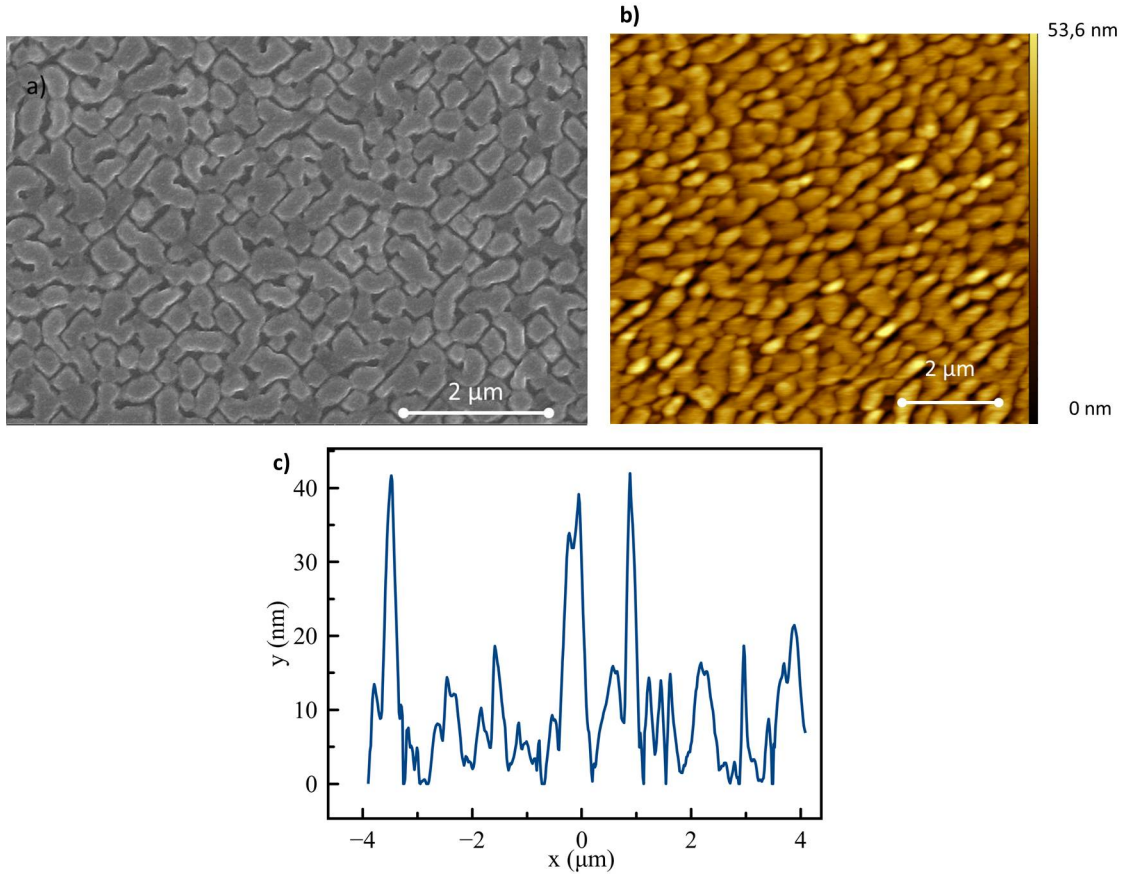


FIGURE 3.5: a) The SEM image of the sample grown at 700°C. b) The AFM image of the sample grown at 700°C. c) The profile plot of the AFM image.

This type of morphology can be changed by growing samples under different temperatures. Lower deposition temperature leads to smoother morphology. Figure 3.6 shows the SEM scan of the sample grown at a) 600°C and b) 500°C.

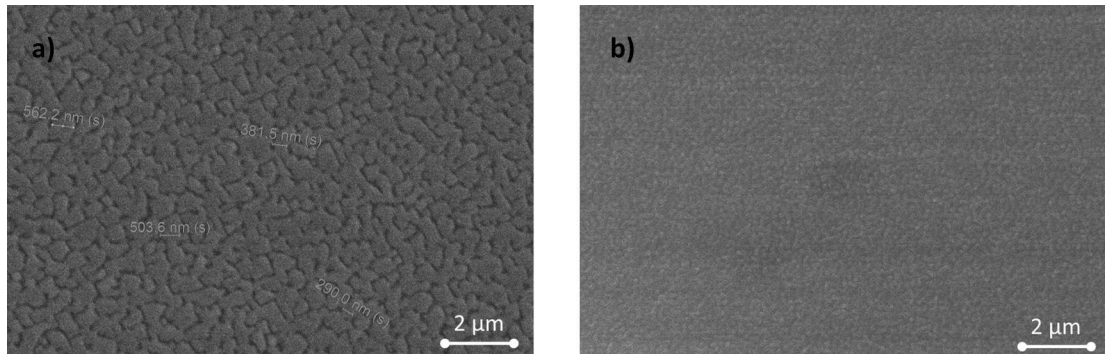


FIGURE 3.6: The SEM images of 80 nm Mn_2Au (001) thin films grown at a) 600°C and b) 500°C.

The level of roughness can be further improved by adding a step of post-annealing. The post-annealing process was performed at 700°C for 1 hour. A longer post-annealing process leads to a significant growth of the lines on the $\theta/2\theta$ scan correspond to (001) phase, which shows that the size of the crystallites in the growth direction becomes reduced. Figure 3.7 shows the SEM and AFM images of the sample grown at 500°C with the post-annealing step.

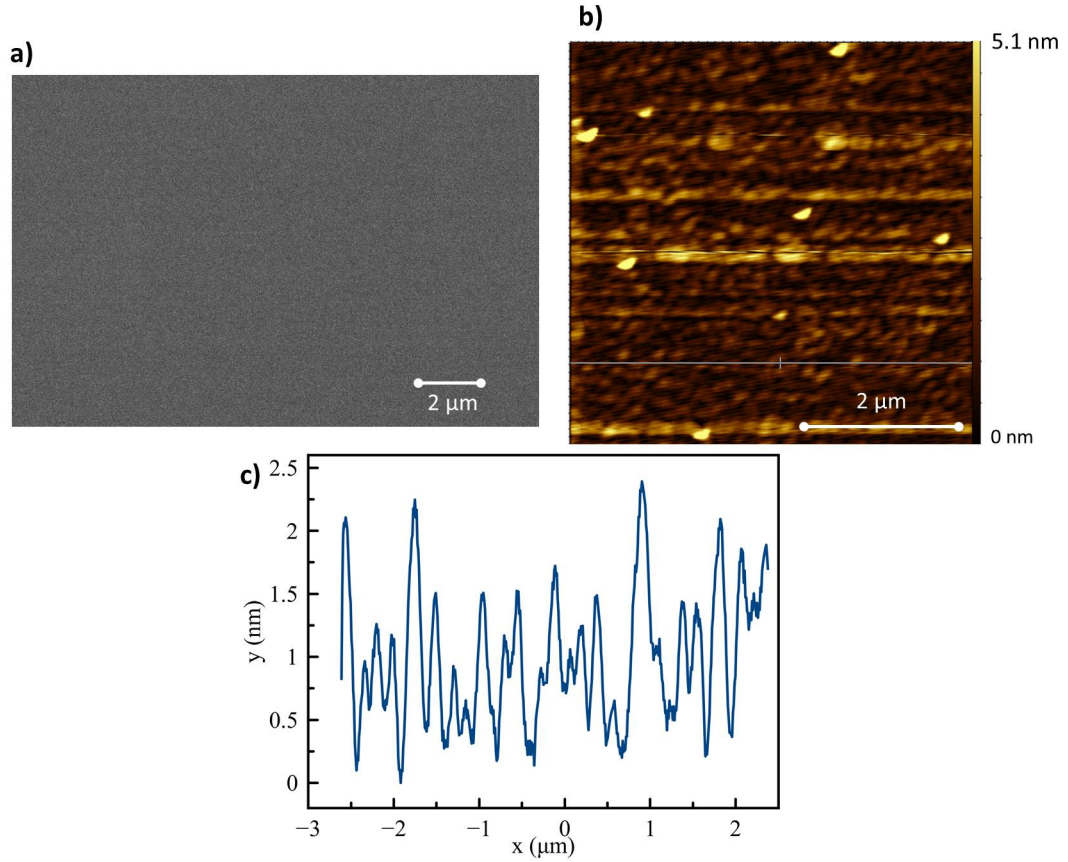


FIGURE 3.7: a) The SEM image of a 80 nm $\text{Mn}_2\text{Au}(001)$ thin films grown at 500°C with the post-annealing process at 700°C. b) AFM scan of a sample grown at 500°C with the post-annealing process. c) Profile plot of the AFM scan.

By tuning the depositing temperature and using the post-annealing procedure we can achieve different crystal and morphological quality of our sample. In my work, the reorientation of the Néel vector was investigated in the samples with different morphological and crystal qualities. The description of the experiments and experimental results on the Néel vector switching will be given in the following chapters.

3.3 Patterning of the Mn_2Au microstructures by optical lithography

In order to prepare microstructures from the thin films of Mn_2Au , I used a positive photolithography process. Photolithography allows to achieve a spatial resolution up to $1\ \mu\text{m}$. The process of optical lithography includes several steps. The first step is spin coating of the samples. In our case the samples were covered by positive photoresist ma-P 1215 using spin coating. The samples were spin coated at a frequency of 3000 rpm during 30 seconds. At the second step, the spin coated samples were put in contact with an optical mask and illuminated by UV light. After that, I developed the samples by putting the samples into the ma-D 331 developer for 12 seconds. In case of a positive process the photoresist remains after the development step in the area, which was recently exposed to light (see fig. 3.8). As the next step, the samples were etched by using an ion etcher IonSys 500. The samples were etched down to the sapphire substrate. As the last step, I removed the remaining photoresist by putting the samples into an ultrasonic acetone bath for 15 minutes. Figure 3.8 shows the necessary steps for both positive and negative photolithography.

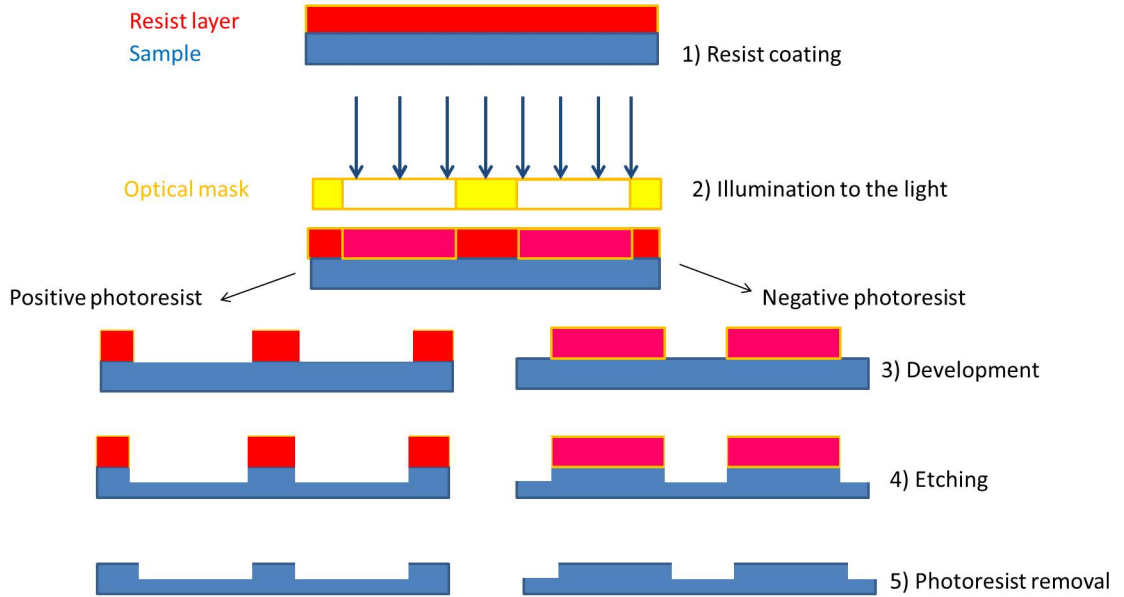


FIGURE 3.8: Schematic representation of the optical lithography process.

For the transport experiments described in the next chapter, I patterned devices using positive optical lithography. Each sample used in this experiments has two structures, patterned from a $1 \times 1\ \text{cm}^2$ Mn_2Au thin film. The first structure is aligned resulting in a direction of the writing current pulses parallel or perpendicular to the easy axes of

Mn_2Au . The second structure is rotated by 45 degrees with respect to the first structure. The figure below shows the layout of the structure used for the transport experiments.

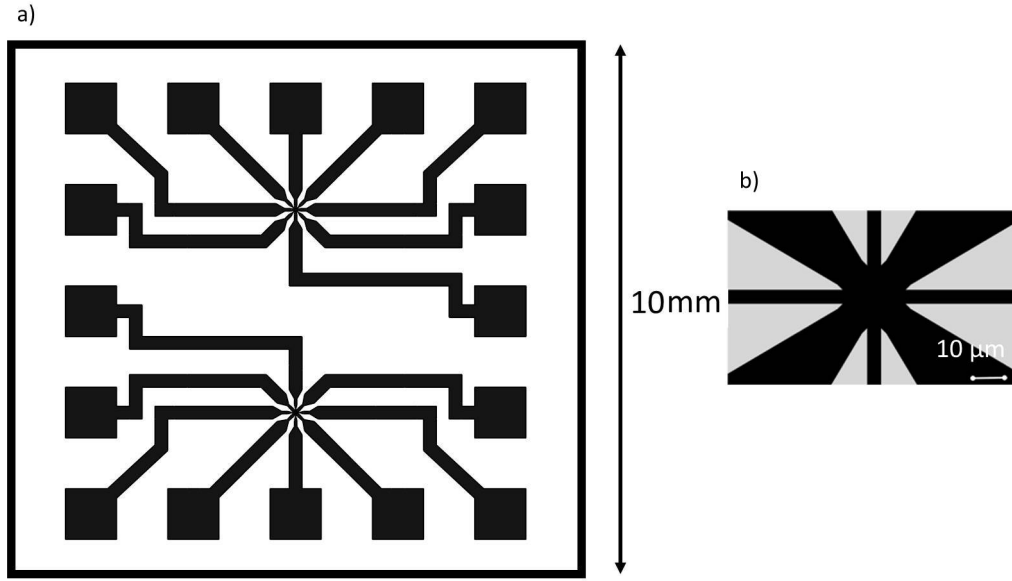


FIGURE 3.9: a) The layout of the structure used for the transport measurements. b) A zoomed-in image of the central part of the cross-structure.

This type of geometry allows injecting current pulses in two orthogonal directions and probing of the resistance of the central area using the other 4 wires. The structures used for the XMLD-PEEM experiments described in chapter 5 and the structure for the magneto-transport measurements described in chapter 6 were prepared using the same photolithography process.

Chapter 4

Current induced switching of Néel vector in Mn_2Au

In this chapter, I demonstrate current-induced manipulation of the Néel vector in Mn_2Au samples detected by electric transport measurements. The current-induced changes of the resistance in Mn_2Au were measured both in longitudinal and traversal configurations. Additionally, the possible impact of current-induced sample heating is also discussed in this chapter.

4.1 Current-induced Néel vector reorientation in Mn_2Au

The samples for the transport measurements were grown using RF-sputtering following the recipe described in chapter 3. By using a positive photolithography process, I patterned the Mn_2Au thin-films into cross-like structures. Figure 4.1 shows the structure used for the current-induced Néel vector switching experiments. As shown in chapter 3, the first structure has a geometry, in which the wide stripes for the writing pulses are parallel or perpendicular to the easy axes in Mn_2Au . The second structure is rotated by 45 degrees with respect to the first structure. The crystallographic directions of the epitaxial Mn_2Au thin films were determined from the in-plane XRD measurements.

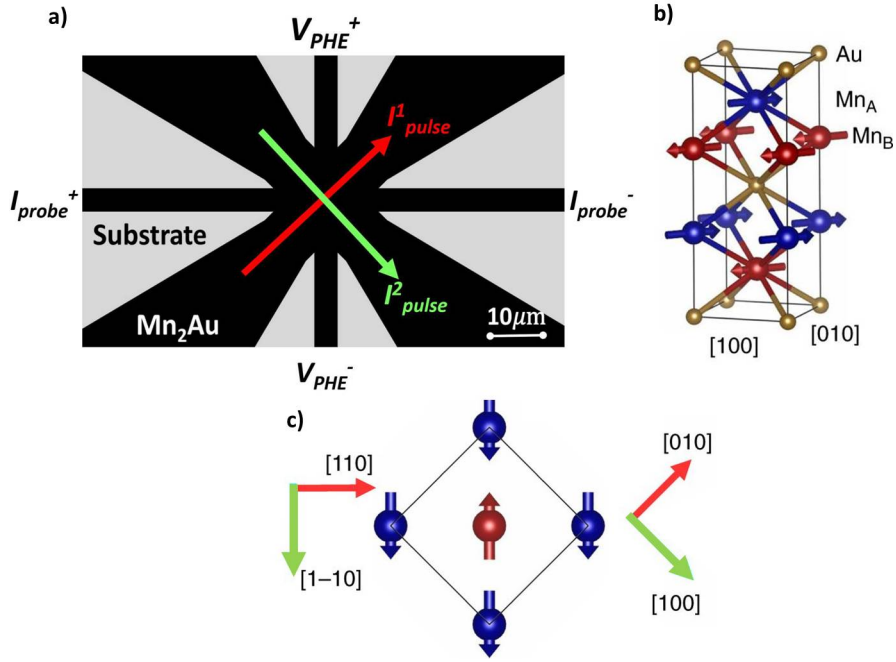


FIGURE 4.1: The sample layout. a) Star pattern used for the current-induced Néel vector manipulation experiments with current pulse directions $I_{1/2pulse}$ and probing contacts for transversal resistance measurements indicated. b) Crystal and structure of Mn_2Au . c) In-plane orientation of the epitaxial Mn_2Au thin films, which corresponds to the star pattern shown in a) I_{pulse} parallel to $[1\bar{1}0]$ or $[110]$ and parallel to $[100]$ or $[010]$.

For the transport experiments, I have grown 80 nm continuous films of Mn_2Au on R-cut sapphire with 10 nm of Ta as a buffer layer. After that, the thin films were patterned into a star-like structure, which is shown in figure 4.1. As mentioned previously, four contacts were used to inject current pulses along two orthogonal directions. Figure 4.2 shows the value of the transversal resistance recorded after the application of the current pulse trains along two easy axes. In this experiment I used current pulses with a pulse width of 1 ms and a delay between the pulses of 10 ms. This relatively long delay between the pulses was set in order to avoid excessive heating of the samples. As a single current pulse resulted in very small changes of the read-out signals only, the current pulses were applied in trains. Each train contained 100 pulses. The writing current pulses were first applied along the $[110]$ and $[1\bar{1}0]$ easy axes of Mn_2Au . The resistance was recorded 10 seconds after each train of current pulses in order to avoid any possible contribution of heating to the resistance value. The current density in this experiment was ranged from 1.4×10^7 to 1.8×10^7 A/cm². It can be clearly seen in figure 4.2 that increasing the current density of the writing pulses leads to larger changes of the transversal resistance. This is consistent with the model in which we assume a rotation of the Néel vector in the central part of the structure.

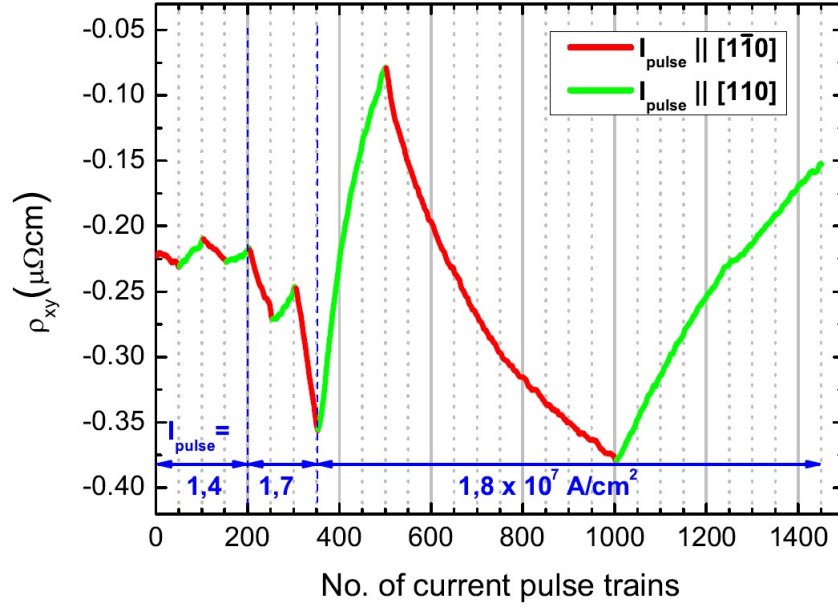


FIGURE 4.2: Probed transversal resistivity (DC probing current density 10^4 A/cm²) vs. the number of applied pulse trains along different directions. The crystallographic direction in which the current pulses were injected is indicated by the green and red color of the data points. The pulse current density was increased from 1.4×10^7 to 1.8×10^7 A/cm² as indicated in the graph.

A similar experiment was performed with samples patterned in a geometry with a similar cross structure but rotated by 45 degrees with respect to the first structure. This time the writing pulses were applied along [100] and [010] crystallographic directions. In this experiment, the values of the longitudinal and transversal resistances were recorded in the same way as described before. In figure 4.3 it can be clearly seen that the application of the writing current pulses in the orthogonal directions leads to a change of resistance for, both transversal and longitudinal geometries. This result is consistent with the reorientation of the Néel vector model. The reorientation of the Néel vector generates positive or negative changes of the resistance, depending on the direction of the applied writing current pulses. For the first trains of writing pulses, only small variations of the longitudinal resistivity were observed. However, with the application of the subsequent pulse trains of the same amplitude the magnitude of the resistance changes increased. The resistance modifications decrease with the application of the further writing current pulses.

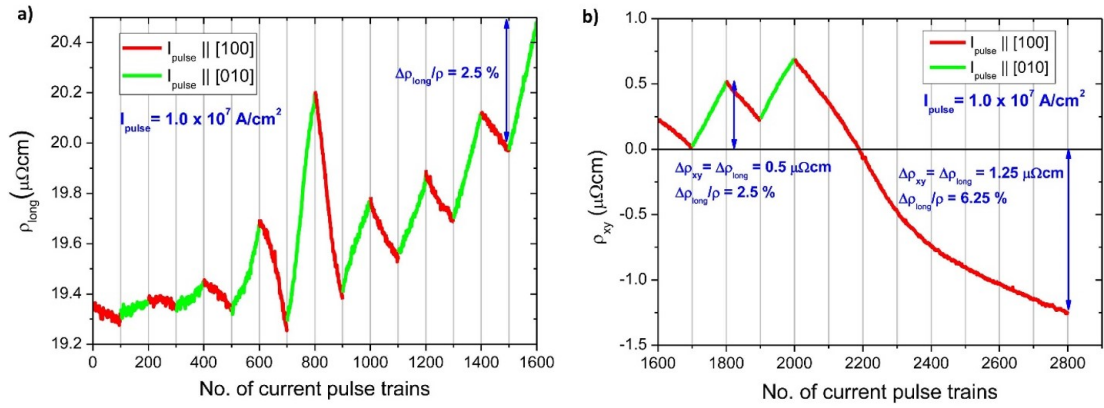


FIGURE 4.3: Longitudinal and transversal resistivities. a) Longitudinal resistivity (DC probing current density 10^4 A/cm^2) vs. number of applied pulse trains. b) Transversal resistivity of the same sample as shown in the main panel of a vs. number of applied pulse trains. The crystallographic direction in which the current pulses were injected is indicated by the green and red color of the data points.

Similar experiments were performed for another sample prepared by the same recipe as the sample discussed above. For this sample I used trains of current pulses with a density of $1 \times 10^7 \text{ A/cm}^2$ injected along two orthogonal directions. Figure 4.4 shows the longitudinal resistance value recorded after the application of the current pulses.

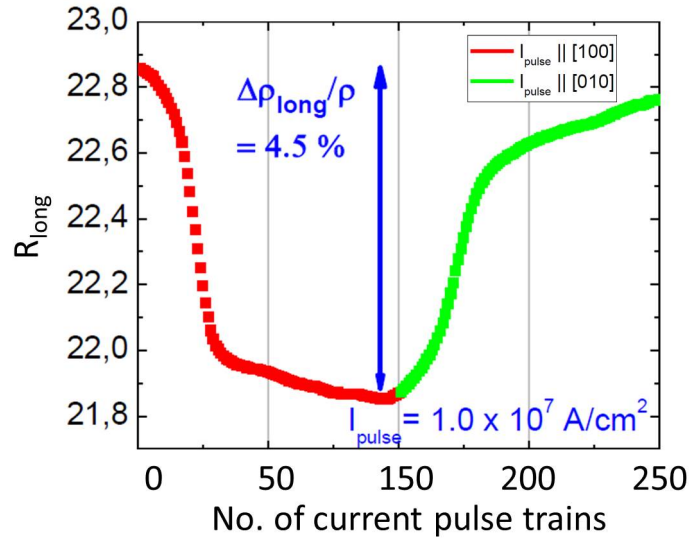


FIGURE 4.4: Longitudinal resistance recorded after the application of the current pulses along two orthogonal crystallographic directions. The crystallographic direction in which the current pulses were injected is indicated by the green and red color of the data points.

In this experiment I observed a saturation of the signal. The saturation behavior in this sample was observed 4 times before the sample got destroyed. The total resistance changes achieved in this case is about 4.5 %.

The resistance changes observed in these transport experiments are consistent with NSOT model of the Néel vector switching in the Mn_2Au . However, the experimental results described in chapter 6 shows the AMR value in Mn_2Au in the order of 0.15 %. As the source of magnetoresistance in the order of 2 % we consider DWs resistance.

It is also important to mention that the changes of the resistance induced by the current pulses did not decay with time. This phenomenon is very likely to be related to the stable state of a new domain configuration induced by the current pulses. Persistent changes in the domain structures induced by the current pulses were also visualized by the XMLD-PEEM. The results of this investigation are described in the next chapter.

4.2 The role of heating in the Néel vector switching process

In order to investigate the influence of the Joule heating on the Néel vector switching process in Mn_2Au values of the sample resistivity was recorded, while applying current pulses of different amplitudes. The voltage drop across the sample during the application of the current pulses was recorded using a digital oscilloscope Tektronix TDS210. Figure 4.5 shows the profile of the voltage drop recorded during the application of the current pulses of different amplitudes. The application of the current pulses leads to the generation of the Joule heating, which leads to the temperature increase. Mn_2Au is a metal compound, for which we recently measured $R(T)$ curve [22]. During the application of a current pulse, we extrapolate linearly $R(T)$ above room temperature, thus we are able to conclude what the sample temperature is.

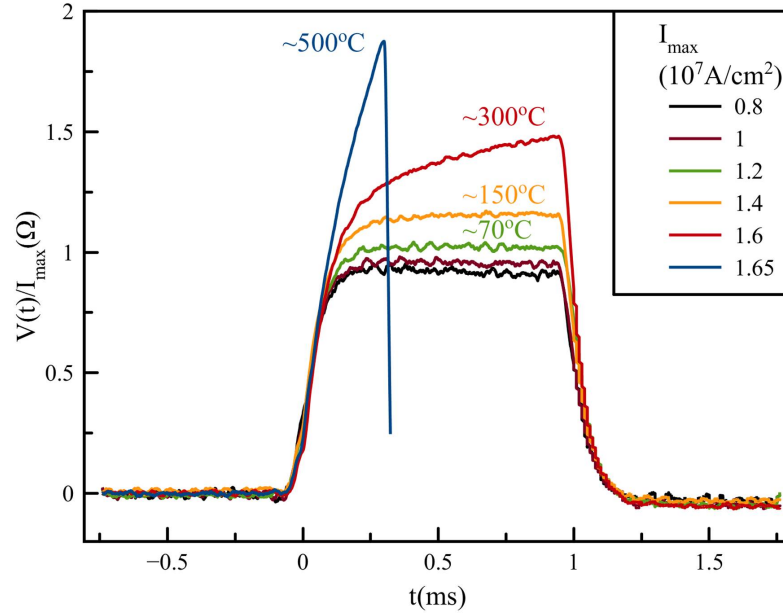


FIGURE 4.5: Current pulse induced sample heating. Time dependent normalized voltage $V(t)/I_{max}$ measured while applying current pulses. The current pulse induced temperature of our sample is estimated from a comparison with the Mn_2Au temperature dependent resistivity $R(T)$ [22] extrapolated above the room temperature.

In figure 4.5 we can clearly see that the average temperature of the sample stays much below the Néel temperature of Mn_2Au ($T_N=1500$ K) and the deposition temperature, which in the case of this sample was $700^\circ C$. At the same time, during the application of the current pulses with the current density of $j=1.6 \times 10^7$ A/cm², at which I observed massive changes of resistance, the sample temperature increases to $300^\circ C$. There are some mechanisms how the sample temperature can affect the Néel vector switching process. The first possible impact of the heating on Néel vector reorientation is the possible reduction of the anisotropy barrier which is necessary to overcome in order to switch the Néel vector orientation [41]. The second possible impact of the heating is the reduction of the strength of the pinning centers of antiferromagnetic domain walls. Another probable impact of the heating on the Néel vector switching is formation of the anisotropy gradient across the sample due to the presence of the inhomogeneous sample heating. This can as well possibly shift domain walls. Also, it is important to mention here that during the application of current pulses the temperature of the sample goes to values which are comparable to the deposition temperature ($700^\circ C$). In principle at these temperatures annealing processes are possible, but these are unable to explain the observed increase and decrease of the longitudinal resistance associated with a change of the current pulse directions.

4.3 Simulation of the current distribution in the microstructures

The structure that I used for the transport experiments has a quite complicated design with several wires for a current injection and a voltage probe. It would be reasonable to assume that the current distribution across this structure is inhomogeneous. In order to understand how electric current can propagate through the structure I performed simulations. I used a python based software called Agros 2D that allows to solve the 2D differential equations for the different types of geometries and different boundary conditions. Particularly, in our case I used this software to solve one of the Maxwell's equation (Gauss's law) in the differential form:

$$\text{div}\mathbf{E} = 4\pi\rho, \quad (4.1)$$

where ρ is the total electric charge density (charge per unit volume) and $\text{div}\mathbf{E}$ is the divergence of the electric field.

I performed simulations for structure similar to the structures that I used for the Néel vector switching experiments described above. Figure 4.6 shows the color map of the electric field during the application of the writing pulse. It can be clearly seen that the application of the pulse leads to a high value of the electric field in the region next to all four sharp corners. That leads the accumulation of the Joule heating in the corner regions, which I observed experimentally as the spots of destroyed material at the corners of the microstructures.

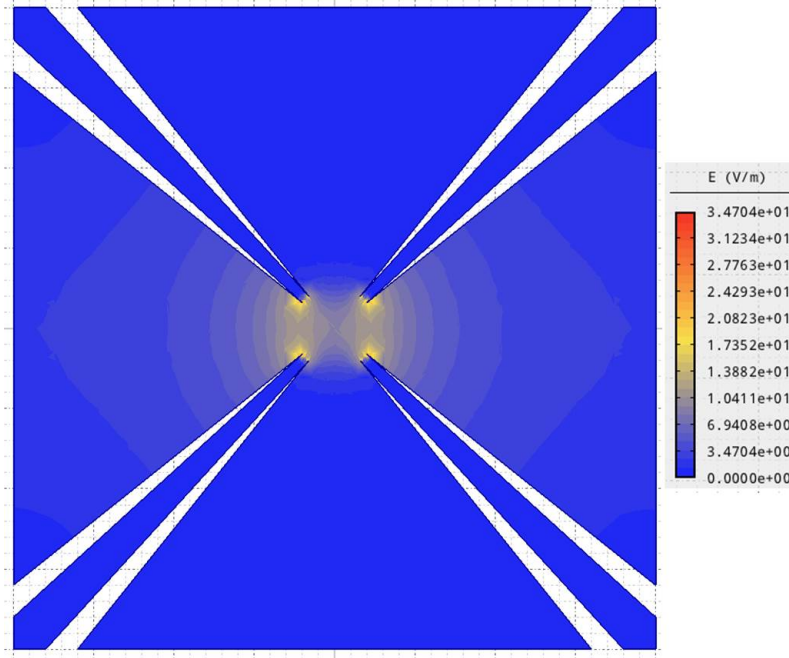


FIGURE 4.6: A color map of the electric field distribution during the application of the writing current pulse.

I also performed simulations for the case in which the probing current is injected through the thin wires. The result of this simulation is reflected in figure 4.7. Similarly to the previous case we have hot spots of the high value of the electric field next to the sharp corners.

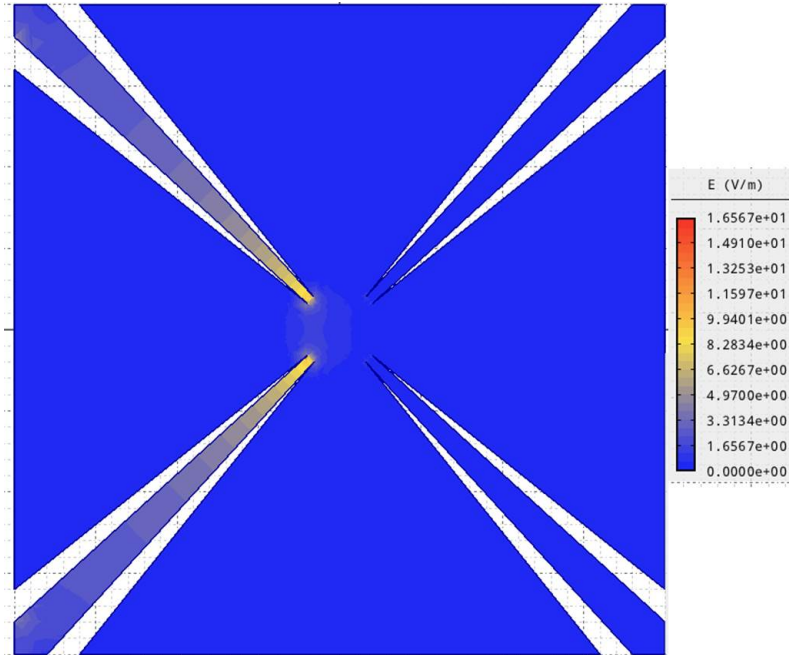


FIGURE 4.7: A color map of the electric field distribution during the application of the probe current.

It is also worth mentioning that the electric field is distributed inhomogeneously across the central area of the sample. The resistance of the central area is presumably not the same everywhere due to the inhomogeneous writing current pulse propagation. Damaged parts of the films on the corner of the structure also lead to massive changes in the resistance. However, those changes can only result in increasing of the longitudinal resistance.

Chapter 5

Direct visualization of current induced Néel vector switching in Mn_2Au

In this chapter, I show the results on the visualization of current-induced Néel vector switching in Mn_2Au using XMLD-PEEM. We observed changes of the magnetic contrast of the AFM domains after application of the current pulses with the current density in the order of 10^7 A/cm^2 . The same order of pulse current magnitude, which produced the previously described resistance changes, also results in modifications of the domain structure.

5.1 Visualization of the antiferromagnetic domains in Mn_2Au

In order to visualize AFM domains in Mn_2Au , we have performed XMLD-PEEM experiments. For these experiments, we used the same type of samples as I used for the Néel vector switching transport experiments described in the previous chapter. The experiments were carried on beamline I06 at Diamond Light Source (UK). As mentioned in chapter 2, this type of a beamline has a shallow geometry. An incident X-ray beam hits the sample plane under 16 degrees. Figure 5.1 shows the geometry of the X-PEEM experiment with the shallow geometry.

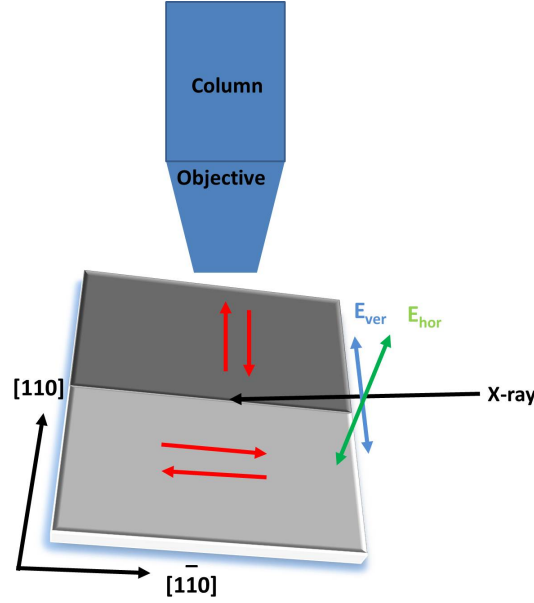


FIGURE 5.1: Schematic image of the X-PEEM experiment with shallow geometry. The red arrows indicate the Néel vector. The blue and green arrows indicate the vertical and horizontal polarization, respectively.

Before acquiring XMLD-PEEM images, we have measured XAS for each sample in order to make sure that the sample does not show surface oxidation. We measured XAS around the L_3 and L_2 absorption edges of Mn. X-ray absorption spectra were recorded for linear vertical and horizontal polarization of the X-ray beam and normalized by an unfocused image. In order to calculate the XMLD spectrum, we subtracted the normalized XAS spectra for the horizontal and vertical polarization, and used the following formula:

$$XMLD(E) = \frac{I(E)_{hor} - I(E)_{ver}}{I(E)_{hor} + I(E)_{ver}}, \quad (5.1)$$

where $I(E)_{hor}$ and $I(E)_{ver}$ is a total signal for the horizontal and vertical polarization, respectively.

Figure 5.2 a) shows the XAS measured at the L_2 and L_3 absorption edges of Mn and the corresponding XMLD spectrum calculated by the formula shown above.

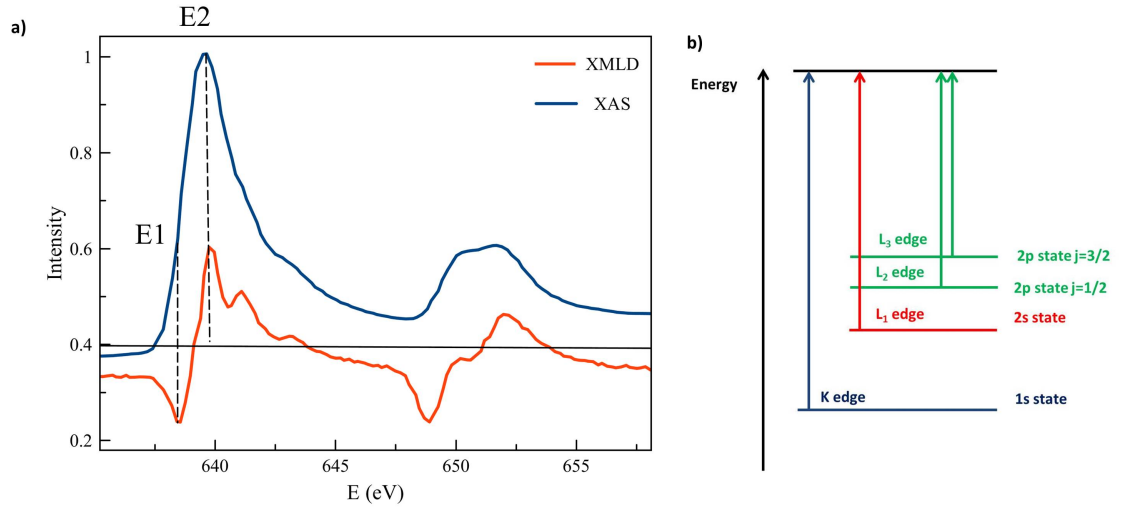


FIGURE 5.2: a) The XMLD and XAS spectra of Mn₂Au. b) A schematic representation of the electron transitions from the core level to the Fermi level.

It is important to mention that in case of an in-plane antiferromagnetic order, which is the case for Mn₂Au (001), it is not possible to use the images, which were taken using the vertical and horizontal polarization of the incident X-ray beam, in order to get the magnetic contrast. The polarization vector of the incident X-ray beam, in case of the vertical polarization, has a very small (16 degrees) angle with the Néel vector of Mn₂Au (see fig. 5.1). This circumstance makes the contrast between different domains with different in-plane orientation of the Néel vector not sufficient. To overcome this difficulty, we used another method of getting the magnetic contrast.

To visualize AFM domains in Mn₂Au, the same method was used as in our previous work on the visualization of the AFM domains in Mn₂Au [31]. In this method we calculated the asymmetry image from two images taken at two different X-ray energies. The first energy $E_1=640$ eV corresponds to the Mn L₃ absorption edge, which roughly has the same value as the maximum of the XMLD spectrum. The second energy E_2 is 0.8 eV lower than the maximum of absorption, which corresponds to the minimum of the XMLD spectrum. In order to get the magnetic contrast, we used the following formula:

$$I_{asym} = \frac{I(E_1) - I(E_2)}{I(E_1) + I(E_2)}, \quad (5.2)$$

where $I(E_1)$ and $I(E_2)$ are intensity pictures taken at energies E_1 and E_2 , respectively.

Using this formula, the AFM domains in Mn₂Au were visualized. In this experiment we kept the polarization of the incident X-ray parallel to the easy axes of Mn₂Au. Figure 5.3 a) shows an asymmetry image of the 240 nm Mn₂Au thin film. The dark

and bright areas correspond to the AFM domains with two orthogonal orientations of the Néel vector. The red arrow indicates the polarization direction of the incident X-ray beam. The data in this experiment were evaluated by A. Sapozhnik.

For the XMLD-PEEM measurements it is always necessary to verify the magnetic origin of the contrast. Usually, this can be done by heating up the sample above the Néel temperature, but due to a very high Néel temperature ($T_N=1500$ K) of Mn_2Au , this method is not applicable. In order to confirm the magnetic origin of contrast seen on asymmetry images (see fig. 5.3), calculated by formula 5.2, we performed these measurements for three different orientations of the crystallographic axes of the sample with respect to the incident X-ray and its polarization.

Figure 5.3 shows the asymmetry images of a 240 nm thin film of Mn_2Au measured for a) 0 degrees , b) 45 degrees and d) 90 degrees.

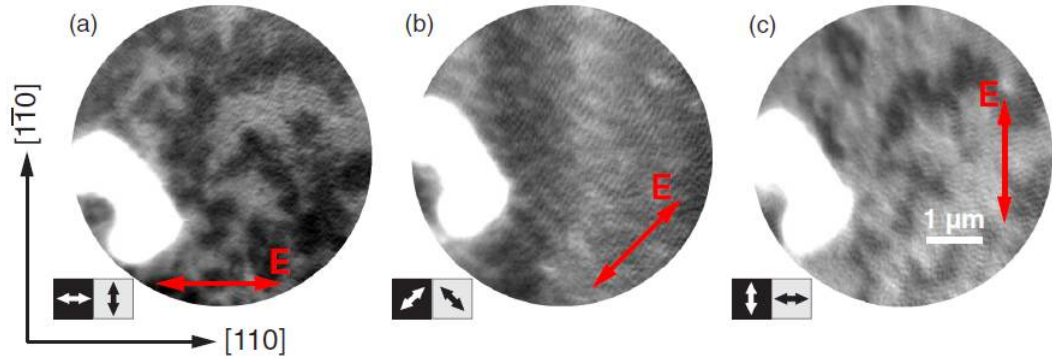


FIGURE 5.3: Asymmetry images of an as-prepared sample. The in-plane angle of the x-ray direction of incidence is (a) 0° , (b) 45° and (c) 90° with respect to the crystallographic $[1\bar{1}0]$ axis. The red double-headed arrow indicates the electric field vector E of the linearly polarized x-ray beam. The double box at the bottom specifies the Néel vector orientation in the AFM domains. The bright area on the left-hand side of the image is caused by a marker, which was used to keep the image position fixed during the rotation of the sample [31].

As mentioned earlier, the easy plane of Mn_2Au is the (001)-plane. Within this easy plane there are two easy axes parallel to the $[110]$ and $[1\bar{1}0]$ crystallographic directions. In figure 5.3 a) and c) we can see that magnetic contrast of the AFM domain with two orthogonal orientations of the Néel vector changes its sign after the rotation of the sample by 90 degrees. When the polarization of the X-ray beam is orientated by 45 degrees with respect to the easy axes, we see no magnetic contrast. This allows us to conclude that the contrast seen in the asymmetry images represents the antiferromagnetic domains of Mn_2Au .

For the experiments on the visualization of the current induced Néel vector manipulation, we prepared several 80 nm Mn_2Au thin films grown at 700°C on R-cut sapphire.

These samples exhibit a high level of surface roughness. By using the method to calculate the asymmetry images described above, we performed XMLD-PEEM investigations. As the energies E_1 and E_2 we used energies, which correspond to the maximum of X-ray absorption and lower energy was selected to be 0.8 eV below the value of the absorption maximum. Similarly to our previous work, the magnetic origin of the contrast in the asymmetry images was identified by rotating the samples by 90 degrees. A comparison of the asymmetry images for two different incident angles of the X-ray beam can be seen in figure 5.4.

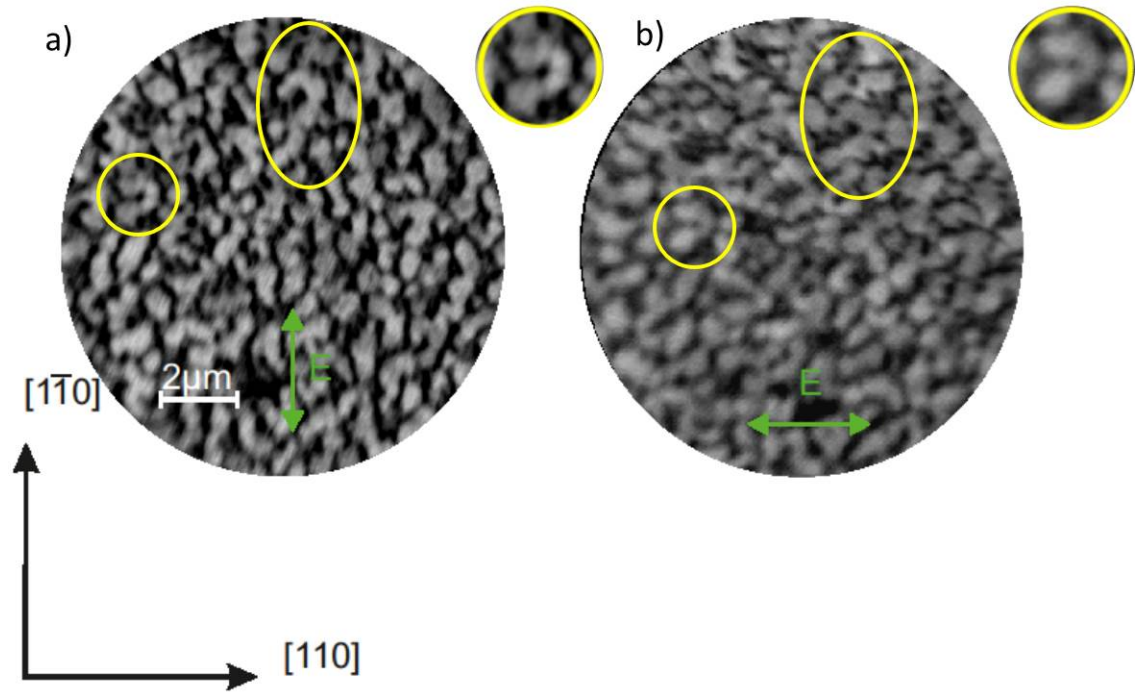


FIGURE 5.4: The asymmetry images for the a) 0 degree and b) 90 degree orientation of a Mn₂Au sample with respect to the incident x-ray beam. The images were taken at the same area of the sample. Within the morphological grain there are two scales of contrast. The two levels of contrast correspond to two orthogonal orientations of the Néel vector. The yellow circles mark the area where the magnetic contrast changes its sign due to the rotation of the sample.

In figure 5.4, it is obvious that the morphological pattern remained visible in the asymmetry images. However, the contrast associated with the AFM domains is presented in these images as well. This can be recognized by the different grey values within the grain structure produced by the morphology. Due to the shallow geometry of the XMLD-PEEM setup, the remained morphological contrast produced a different pattern for the two orientations of the sample. Nevertheless, we can identify regions of the sample where the contrast was inverted after the rotation of the sample by 90

degrees. These areas are marked in figure 5.4 by a yellow oval and a circle. The insets show a zoomed in image of the encircled area..

The morphology of the Mn_2Au thin films was examined using atomic force microscopy and SEM. The level of roughness of the 80 nm thin films is about 30 nm. Figure 5.5 shows the corresponding atomic force microscopy image of a Mn_2Au thin film with such a rough morphology.

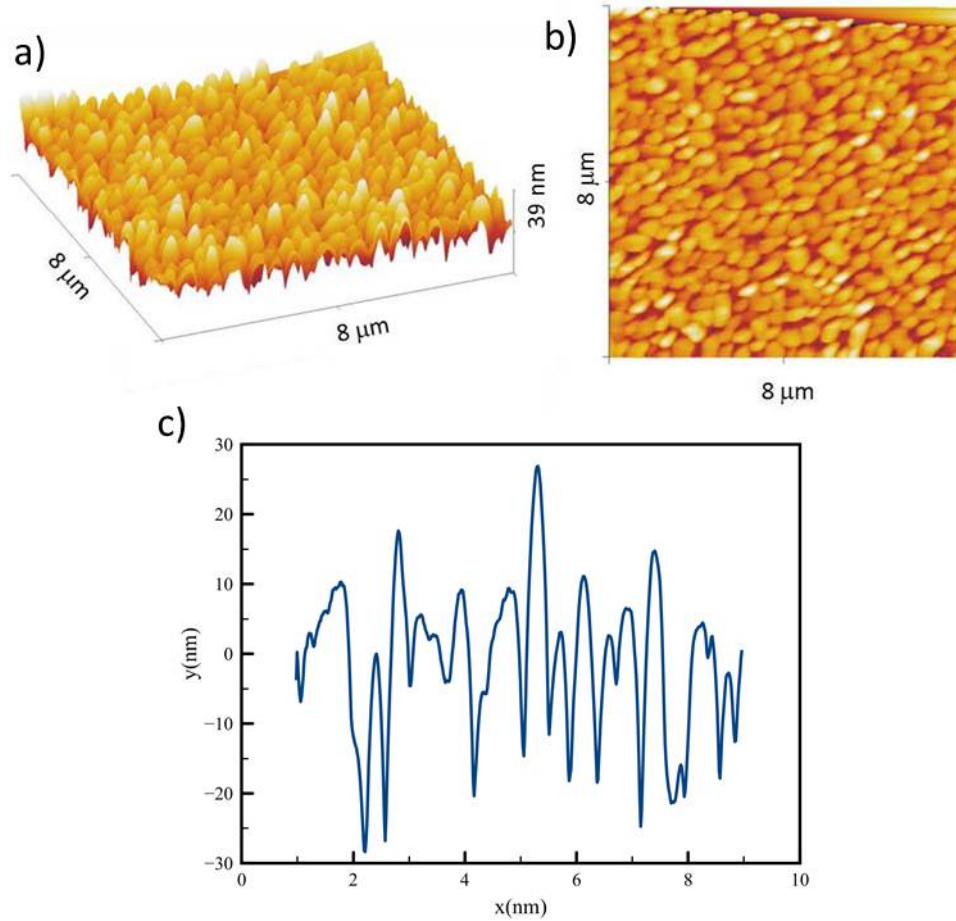


FIGURE 5.5: a) 3D b) 2D AFM scans of the sample used for the Néel vector switching experiment. c) A profile plot of the AFM scan.

The measurement of the PEEM images for two different energies gave us two similar patterns. However, the absorption spectra scale nonlinear for the "valley" and the "hill" areas. That means that the ratio of the intensity for a maximum of absorption $E_2=640$ eV and at the energy $E_1=639.2$ eV has different values for the "valley" and the "hill" areas. This can be seen as a nonlinear scaling factor for intensities taken at the different areas of the sample. When we subtract the PEEM images taken at the different energies we cannot get rid of the morphological contribution to the contrast due to this phenomenon. Figure 5.6 shows XAS for the "hill" and the "valley" areas of the sample.

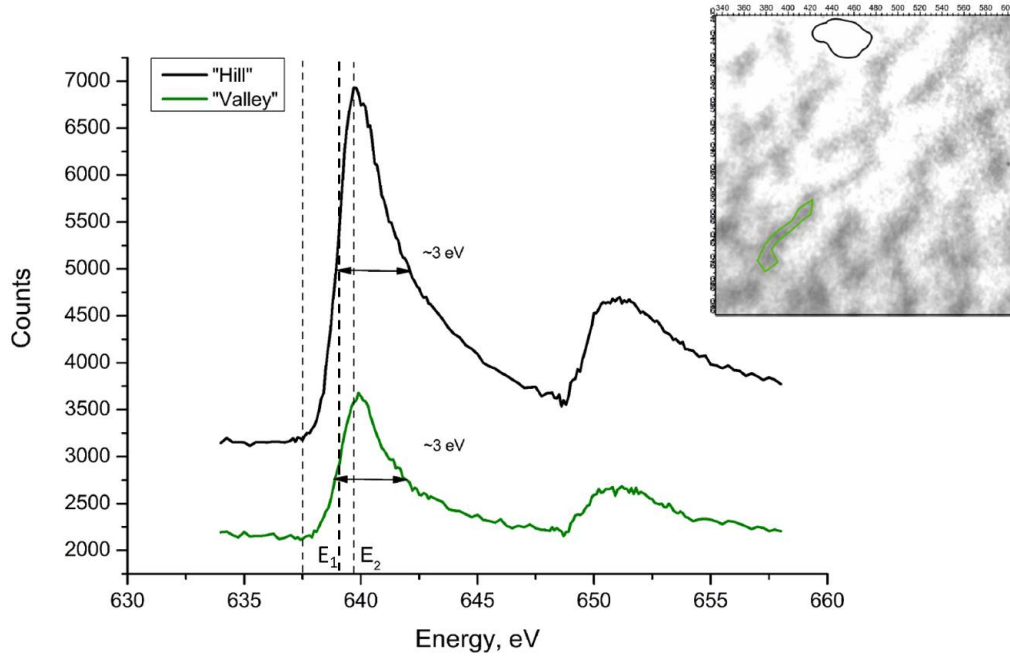


FIGURE 5.6: XAS taken at the different positions of the sample. The black curve shows the XAS for the "hill", the green for the "valley". The insert shows the part of the sample where the XAS was measured.

As I have mentioned earlier, the formula 5.2 was used in order to get the asymmetry images. For the case of a very pronounced morphology, the asymmetry images will always contain both the morphological and the magnetic contrast. In all the asymmetry images we can see four levels of contrast. Black color corresponds to the morphological "valley" area. Morphological features corresponding to the "hill" area have two different intensity values (corresponding to two grey levels). These two scales marked correspond to the orthogonal orientations of the Néel vector. The border region corresponds to an intermediate intensity. Figure 5.7 shows a histogram taken from an asymmetry image. The total distribution is fitted by four Gaussian normal distribution curves corresponding to the different sources of XMLD-PEEM intensity.

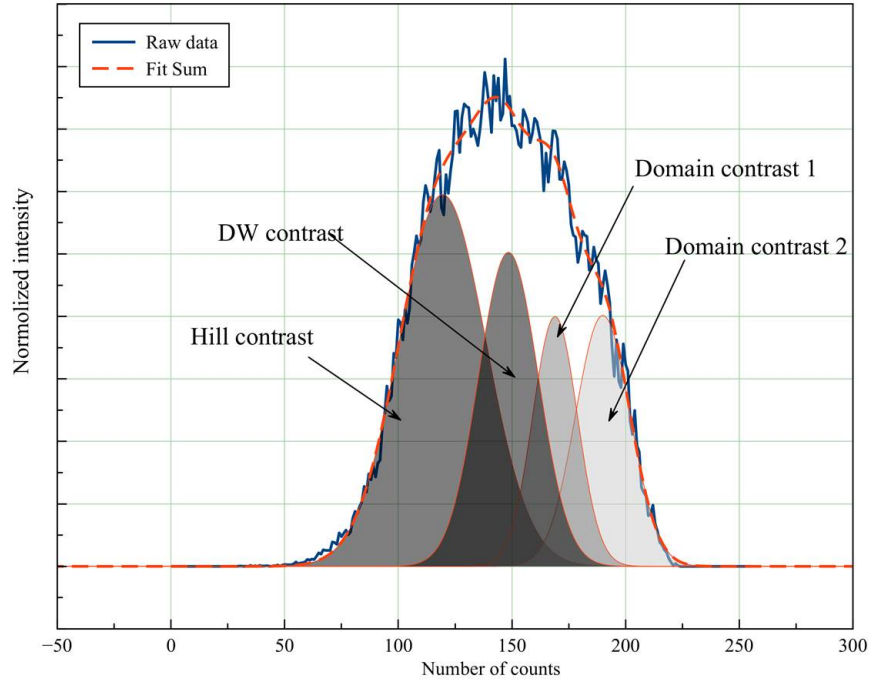


FIGURE 5.7: Histogram distribution of contrast of the XMLD-PEEM asymmetric image.

5.2 Switching of the Néel vector in the as-prepared sample

In the previous section I describe the visualization of the static domain patterns in Mn_2Au . The next step of our investigation is the visualization of the domain pattern changes induced by the electric current pulses. In order to visualize the switching of the Néel vector we performed XMLD-PEEM investigations of patterned Mn_2Au thin films. Continuous films of Mn_2Au were patterned into the cross structures with four wires, which allows injecting the current pulses along the $[110]$ and $[1\bar{1}0]$ crystallographic directions. The central part of the structures has a size $10 \times 10 \mu\text{m}^2$. Figure 5.8 shows a schematic image of the sample layout and of the shallow geometry of the XMLD-PEEM experiment.

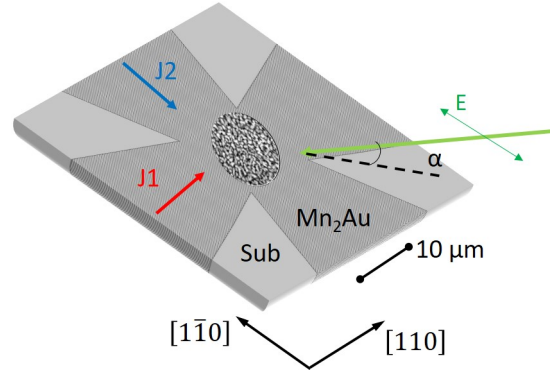


FIGURE 5.8: Sample layout used for the switching experiment and the geometry of the experiment [42].

For the XMLD-PEEM imaging experiments I prepared two types of samples. The sample of the first type is an as-prepared thin film of Mn_2Au (001) with a thickness of 80 nm grown on the R-cut sapphire substrate and 10 nm of Ta as a buffer layer. The second type of the sample has the same structure but the samples of that type were exposed to a pulsed magnetic field of 60 T along the easy axis. The field exposure was done at the High Field lab of the Helmholtz-Zentrum Dresden-Rossendorf (Germany). This type of a sample shows an almost monodomain state with the Néel vector in a perpendicular orientation to the applied high magnetic field [31]. The results of the current induced Néel vector reorientation for this kind of sample will be discussed in the next section.

The visualization of the current-induced switching of the Néel vector includes three steps. The first step is the visualization of the initial domain pattern, following the procedure described in the previous section. After that, a train of current pulses with a current density of $j=1.35 \times 10^8 \text{ A/cm}^2$, pulse width of 1 ms and delay 10 ms between pulses was applied. In order to inject the current pulses, I used a Keithley 2430 sourcemeter controlled by a Python-based program. After the application of the current pulses we imaged the domain pattern following the same procedure. As the final step, the asymmetry images taken before and after the application of the current pulses were subtracted. This procedure allows us to remove the morphological contribution from the total asymmetry image as well as to visualize the clear changes of the AFM domain pattern induced by the application of the current pulses. Figure 5.9 shows the asymmetry images taken a) before, b) after the application of the current pulses, and c) the difference between a) and b). During the whole time of the experiment, the polarization of the incident X-ray beam was aligned along one of the easy axes and kept in this orientation.

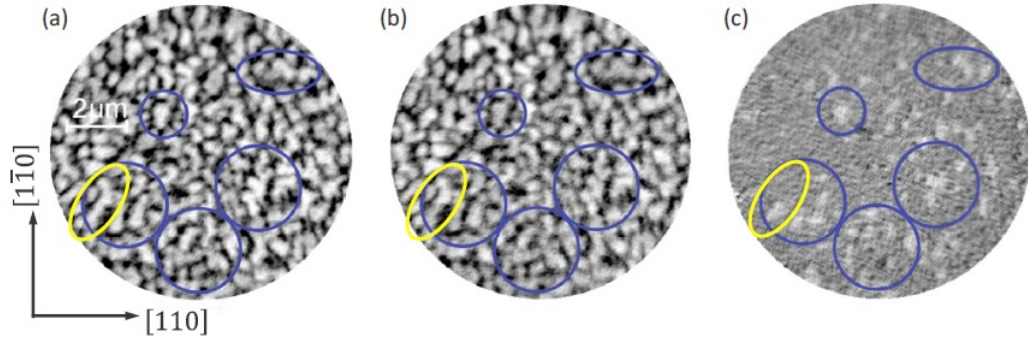


FIGURE 5.9: (a) XMLD-PEEM asymmetry image of a Mn_2Au thin film in the as-grown state. (b) XMLD-PEEM asymmetry image of the same sample at the same position after the application of a train of the current pulses. (c) The difference between the images a) and b). The yellow circle indicates a domain which was switched partially. The blue circles indicate grains where domains were fully switched [42].

There is no morphological contrast remaining in the difference images (Figure 5.9 c). This image shows the AFM domains with the Néel vector reoriented by the current pulses directly. Note, that some of the domains were switched completely and some only partially. The domains that were switched completely are marked on this figure by the blue circles and an example of a domain, which was switched only partially, is marked by a yellow oval. Here we can see that the switching of all domains happens in the same direction. In other words, in figure 5.9 c) there are no areas with a dark contrast. Only the domains with the Néel vector parallel to the applied current pulses were switched. In case of a random thermally activated Néel vector switching process we would see an equal distribution of switched domains with the Néel vector parallel or perpendicular to the applied current.

As the next step, the current pulses were applied in an orthogonal direction with respect to the first current pulse and in order to visualize reversible switching of the Néel vector we applied the current pulses subsequently in two orthogonal directions. Figure 5.10 shows the difference images after the application of the current pulses along the $[110]$ and the $[1\bar{1}0]$ directions.

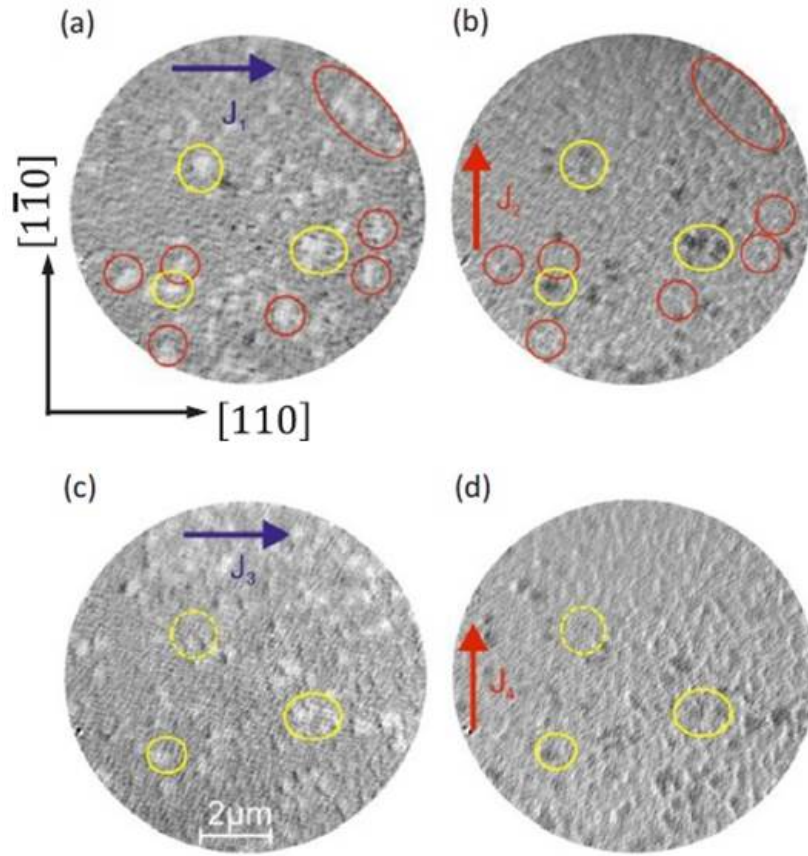


FIGURE 5.10: Difference images calculated from the XMLD-PEEM asymmetry images obtained before and after the subsequent application of the current pulse trains with $I = 1.25 \times 10^7 \text{ A/cm}^2$ along the easy-axis directions $[110]$ and $[1\bar{1}0]$. The current direction for each panel (a)–(d) is indicated by the blue and red arrows. The yellow circles indicate obvious examples of reversibly switching AFM domains, whereas the red circles indicate examples of domains switching irreversibly [42].

In figure 5.10 it is obvious that some domains within the morphological grains can be switched in both directions. This type of domains are marked by the yellow circles. Some of the domains can be switched only in one direction during the injection of the first current pulses. Those domains are marked by the red circles on the figure 5.10. This type of an asymmetric behavior can be related to that fact that the Mn_2Au (001) crystal plane is tilted by 3 degrees with respect to the $(1\bar{1}02)$ plane of the sapphire substrate. This phenomenon was discussed in chapter 3.

The (001) planes of Mn_2Au , which is tilted with respect to the R-cut of sapphire substrate, can cause the asymmetric behavior of the Néel vector switching process. As shown in chapter 1, the value of the effective magnetic field generated by the Rashba effect within magnetic sublattices is proportional to the applied current. In the case of tilted (001)-planes of Mn_2Au , the two orthogonal directions of the current injection

are not equivalent. The projections of the current of this plane is not the same for the two orthogonal directions. This could lead to a small asymmetry in the NSOT for the two orthogonal current directions. Figure 5.11 shows a schematic picture of the applied current and the tilted (001) Mn_2Au planes.

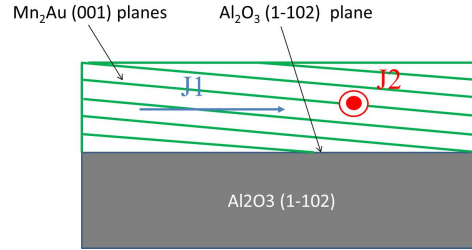


FIGURE 5.11: Schematic image of the asymmetry in the applied current pulses induced by tilted (001) plane of Mn_2Au .

The experiments on the visualization of the current-induced Néel vector reorientation are in good agreement with the transport experiments on the current-induced Néel vector switching described in chapter 4. The application of the subsequent current pulses along the orthogonal easy axes of Mn_2Au leads to positive and negative resistance changes (see chapter 4). At the same time, this can be seen in the XMLD-PEEM experiments as the changes of the magnetic contrast. However, other experiments described in chapter 6 indicate, that the AMR of the domains is much smaller than values observed in chapter 4.

5.3 Néel vector switching in Mn_2Au with prealigned Néel vector

After XMLD-PEEM imaging of the current induced Néel vector switching in the as-prepared sample we imaged the domain pattern of Mn_2Au thin films with prealigned Néel vector. As shown in our previous work, Mn_2Au samples which were exposed to pulses of a high magnetic field of 60 T along the easy axis show an almost monodomain-like pattern [31]. The sample with the prealigned Néel vector was investigated in order to understand the influence of the relative orientation of the current pulse direction and the Néel vector on the switching probability. This sample with the prealigned Néel vector state was grown by the same recipe as the sample discussed in the previous section. The sample has a thickness of 80 nm and is covered by 2.5 nm Al capping layer.

For this type of sample, I patterned cross-like structures similar to the previous experiment with the size of the central region of 10 μm . This structure allows us to inject current pulses along $[110]$ and $[\bar{1}\bar{1}0]$ crystallographic directions. For the field-exposed

sample the current pulses were applied along the direction which is perpendicular to the direction of the applied magnetic field pulse (60 T). After each train of the current pulses, I applied another train of the current pulses along the same direction but with an increased current density. Following the procedure described in the previous section, we accumulated asymmetry images after each current pulse train. Figure 5.12 shows the difference images obtained after the application of the current pulses along $[1\bar{1}0]$ direction with different current densities.

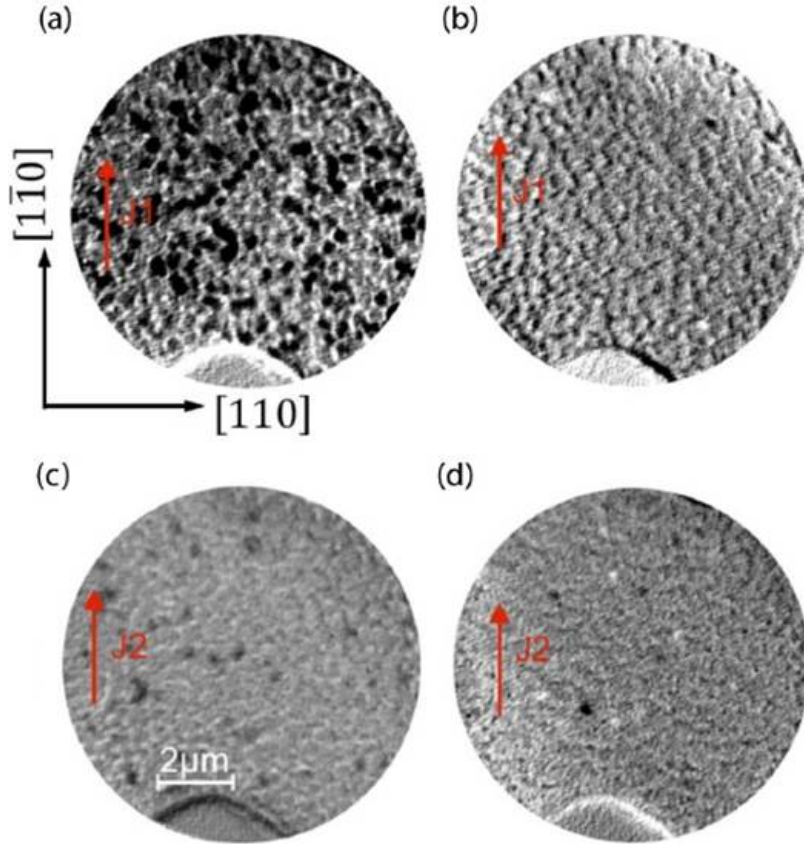


FIGURE 5.12: Difference images calculated from the XMLD-PEEM asymmetry images obtained before and after the subsequent application of the current pulse trains along $[110]$. The Néel vector of this sample was prealigned parallel $[110]$ by a spin-flop transition in a 60-T magnetic field $[110]$ prior to the combined pulsing and XMLD-PEEM experiments. (a) After 100 current pulses with 1.25×10^7 A/cm², (b) after additional 100 current pulses with 1.25×10^7 A/cm², (c) after additional 100 current pulses with 1.3×10^7 A/cm², (d) after additional 100 current pulses with 1.3×10^7 A/cm² [42].

The first train of current pulses with a density of $j=1.25 \times 10^7$ A/cm² was applied perpendicularly to the prealigned Néel vector parallel to $[110]$. This did not lead to any modification of the domain pattern. After that, I applied a train of the current pulses with the same current density $j=1.25 \times 10^7$ A/cm² along $[1\bar{1}0]$ (Figure 5.12 a). That induced massive changes of the AFM domain pattern. The application of the second

current pulse train of the same current density along the same direction did not affect the domain pattern (Figure 5.12 b). As a next step, the current density was increased by 0.05 A/cm^2 . Some of the domains change their contrast, but the changes of the magnetic contrast are much smaller than after the first current pulses (Figure 5.12 c). Then I applied the current pulses with the same current density along the same direction. In this case, we observed no changes of the magnetic contrast (Figure 5.12 d). During the application of the current pulses with the current density $j=1.35 \times 10^7 \text{ A/cm}^2$ the sample suffered from an electrical breakdown. Therefore, no further investigations of the sample were possible.

From all that is mentioned above, we can conclude that the efficiency of the Néel vector switching process in Mn_2Au depends on the current density of the writing pulses. As shown in chapter 4 in figure 4.2, changes of the resistance associated with the current-induced Néel vector switching scale with a current density of the writing pulses. Thus, the changes domain pattern associated with the Néel vector switching observed by the XMLD-PEEM are consistent with the electric transport experiments described in chapter 4. However, in chapter 6 we show the experimental results which indicate a smaller value of the AMR associated with nearly full reorientation of the Néel vector in Mn_2Au .

It would be reasonable to perform experiments that combine the visualization of the current-induced Néel vector reorientation of the AFM domains in Mn_2Au and the measurement of the resistance changes associated with this process. Unfortunately, this was not possible due to a high electrical noise level in the X-PEEM beamline produced by a relay disconnecting the high voltage from the devices.

5.4 Evaluation of the switched domains fraction

In order to determine the fraction of the domains with switched Néel vector, I performed an analysis based on the calculation of the area of the switched domains. I transformed difference images into black and white pictures, in order to count the number of the black and white pixel. After that, I set the threshold at the level at which the switched domains correspond to black color and the non-switched domains correspond to white color. Figure 5.13 shows the difference image in black and white color code with two different threshold levels.

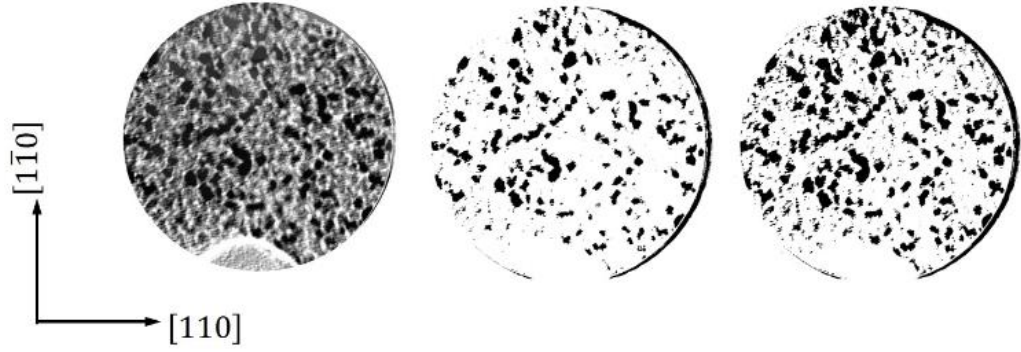


FIGURE 5.13: a) Difference image of the AFM domains manipulated by the current pulses. b) and c) the same in black and white color code for two different threshold levels [42].

This procedure was performed for all the difference images, both for the as-prepared sample and for the sample with the prealigned Néel vector. Figure 5.14 shows the fraction of the domains which were switched by the current pulses.

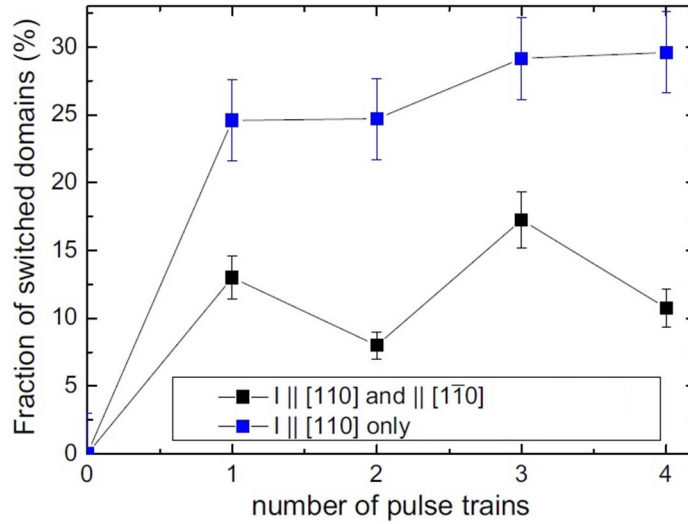


FIGURE 5.14: Fraction of the switched domains derived from 5.10 (black squares), i.e., for subsequent application of the current pulse trains along the easy directions with constant current densities of $1.25 \times 10^7 \text{ A/cm}^2$. The blue squares represent the fraction of switched domains derived from figure 5.12, i.e., for subsequent application of the current pulse trains along the same easy direction with the current densities $1.25 \times 10^7 \text{ A/cm}^2$ [42].

From figure 5.14 it is obvious that in the as-prepared sample there is a smaller number of domains which were switched. This is presumably due to the fact that in as-prepared state there are only half of the domains which can be switched by the application of the current pulses applied along certain easy axes of Mn_2Au . At the same time, in the sample with the prealigned Néel vector state most of the domains are in the required state for NSOT induced Néel vector switching.

Overall, XMLD-PEEM visualization of the Néel vector switching in the AFM domains demonstrated current induced reorientation of the Néel vector in Mn_2Au . The fact that the injection of the current pulses along two orthogonal easy axes of Mn_2Au leads to a rotation of the Néel vector by 90 degrees in only those AFM domains with the Néel vector parallel to the applied current, provides strong evidence for the NSOT mechanism of the Néel vector switching.

Chapter 6

Manipulation of the Néel vector in Mn_2Au by high magnetic field pulses

In this chapter, I show results of the experiments on the reorientation of the Néel vector in Mn_2Au induced by the application the high magnetic field pulses (60 T). As mentioned in chapter 4, the reorientation of the Néel vector induced by current pulses could be influenced by the temperature due to Joule heating. This contribution can be excluded, if the Néel vector is switched by high magnetic field pulses. This allows to identify different contributions to the resistance changes associated with the Néel vector manipulation experiments. In particular, I show that there are two different types of contributions to the resistance changes, which are of magnetic origin. Both are observed in resistance measurements during and after the application of a high magnetic field pulse. The first contribution results either in an increase or in a decrease of the resistance depending on the relative orientation of the applied magnetic field and the direction of the probing current. The magnitude of this contribution amounts to 0.15%. The resistance modifications resulting from this contribution are persistent. The second contribution results in a resistance reduction of about 1-2%, independent from the direction of the applied magnetic field. This resistance reduction decays on the time scale of seconds after the application of the high magnetic field pulse. These phenomena will be discussed in the following chapter.

6.1 Persistent magnetoresistance effects in Mn_2Au induced by high magnetic field pulse

Recently, modifications of the domain pattern in Mn_2Au induced by the application of the high magnetic field pulses were investigated by us [31]. There, we showed that a full reorientation of the Néel vector in Mn_2Au can be achieved by the application of a high magnetic field above 30 T [31] via a spin-flop transition. This phenomenon was observed by XMLD-PEEM. The figure below shows the AFM domain pattern for a) an as-prepared Mn_2Au (001) thin film and b) for a thin film exposed to a 60 T magnetic field pulse.

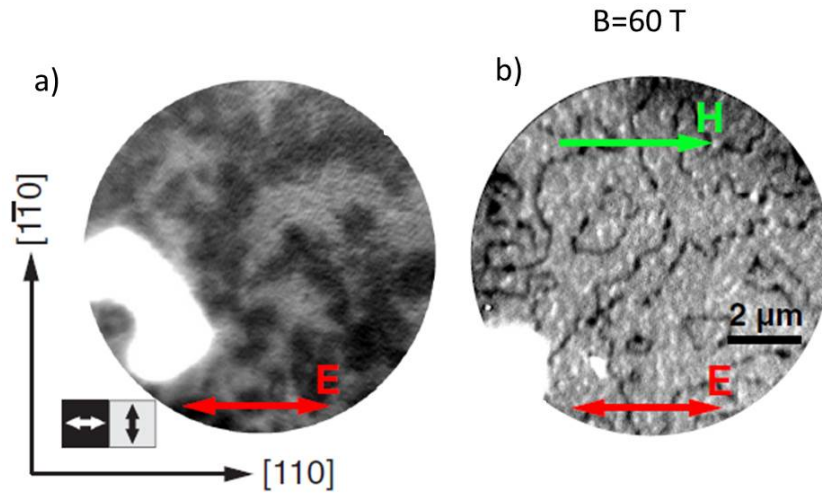


FIGURE 6.1: a) XMLD-PEEM asymmetry image taken in an as-prepared 240 nm $\text{Mn}_2\text{Au}(001)$ thin film. b) XMLD-PEEM asymmetry image taken in 240 nm $\text{Mn}_2\text{Au}(001)$ thin film exposed to 60 T magnetic field pulse along $[110]$ easy axis.

In figure 6.1, it can be clearly seen that the application of a high magnetic field (60 T) pulse along an easy axis leads to massive modifications of the AFM domain pattern in Mn_2Au . In the as-prepared state, we can see an approximately equal number of domains with two orthogonal Néel vector orientations. After applying a 60 T high magnetic field pulse the domain pattern changes dramatically. In this case there are large domains with the Néel vector aligned perpendicular to the direction of the applied magnetic field. These domains are separated by the worm-like domains with the perpendicular Néel vector orientation. It is important to mention that the XMLD-PEEM asymmetry images were measured approximately six months after the application of the high magnetic field pulse. In other words, the changes of the AFM domain pattern are persistent and also can be measured via the magneto-transport measurements.

To measure the persistent changes of the resistance in Mn_2Au induced by the spin-flop transition, I measured the resistance of the sample before and after application of the magnetic field pulse. I used a four-point geometry, in which two contact pads are used to inject the probe current and the other two are used to read-out the voltage drop. The inset in figure 6.2 shows the geometry of the structure used for the transport measurements. This structure allows us to measure the value of the resistance of Mn_2Au along two orthogonal directions at the same time. During the first experiment the probe lines were aligned along the easy axes of Mn_2Au . The probe lines on this structure are 7 mm long and $200\text{ }\mu\text{m}$ wide. To record the value of the resistance I used a Keithley 704 current source for the application of the probe current and a nanovoltmeter Keithley 2182a to read the value of the voltage. The values of the resistance for both directions were recorded with the sampling rate of 1 Hz. The sample was cooled to 4 K for the whole time of the experiment. Figure 6.2 shows the value of the resistance for two probing directions recorded during approximately 20 minutes. At the time of 250 s the high magnetic field pulse was applied.

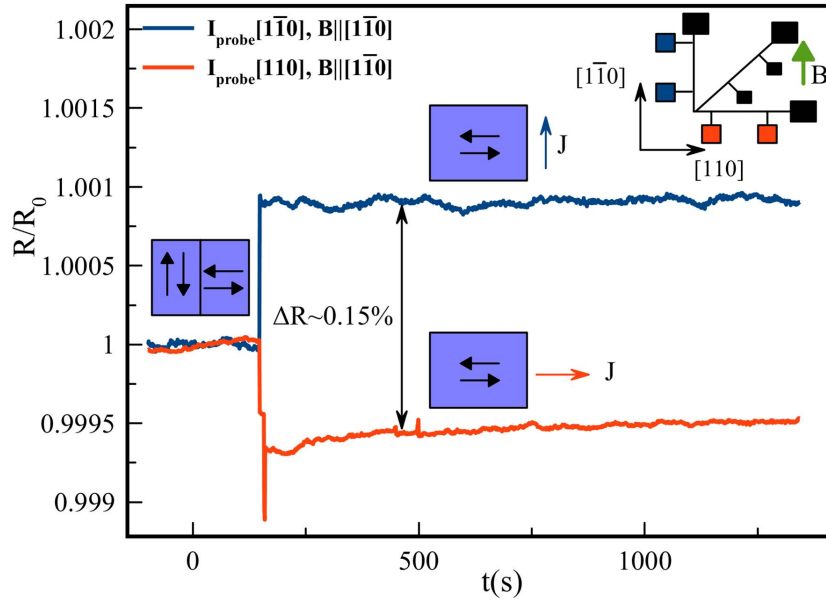


FIGURE 6.2: Time dependent resistance for different probe current directions (see inset) of a Mn_2Au thin film in the as-grown state and after the application of the first 60 T field pulse at $t = 250$ s along the direction indicated in the inset. The standard dc-measurement is unable to produce meaningful data during and directly after the field pulse due to overloading of the nanovoltmeter by the pulse induced induction.

The blue boxes indicate the alignment of the Néel vector.

As shown in this figure, the resistance modifications for both orthogonal probe current directions after the spin-flop transition are persistent. We assume that the spin-flop field aligns the Néel vector orthogonally to the direction of the applied magnetic

field [31]. In figure 6.2 we can see that the resistance decreases when the probe current is applied along the Néel vector and increases when the Néel vector is aligned perpendicular to the probe current. Note that after the application of the high magnetic field pulse there are about 10 seconds during which we cannot measure properly the value of the resistance due to the large voltage drop generated by the electromagnetic induction effect. In this experiment I measured the value of the resistance after the spin flop transition for two equilibrium states. The persistent changes of the resistance induced by the spin-flop transition, which I observed in this experiment, are in the order of 0.15%.

To study the influence of the sample purity on the AMR value in Mn_2Au , I prepared a sample with a higher degree of the mosaicity and increased surface roughness. In this particular case the sample was prepared at a high deposition temperature of Mn_2Au . As mentioned in chapter 2, the samples grown at 500°C with an additional post-annealing step show the best crystal quality. In contrast to that, the sample with the reduced crystal quality was grown at 600°C without the post-annealing step. The sample with the reduced crystal quality shows similar behavior of the AMR as the sample with good crystal quality which was discussed before. However, the magnitude of AMR for the sample with the reduced crystal quality is only 0.05 %. From this we can conclude that the AMR value scales with the crystal and the surface quality of the sample, presumably due to the different residual resistances for the samples with the different levels of mosaicity and the roughness level. Figure 6.3 shows the resistance of the sample with the reduced crystal quality recorded before and after the application of a pulse of the magnetic field (60T).

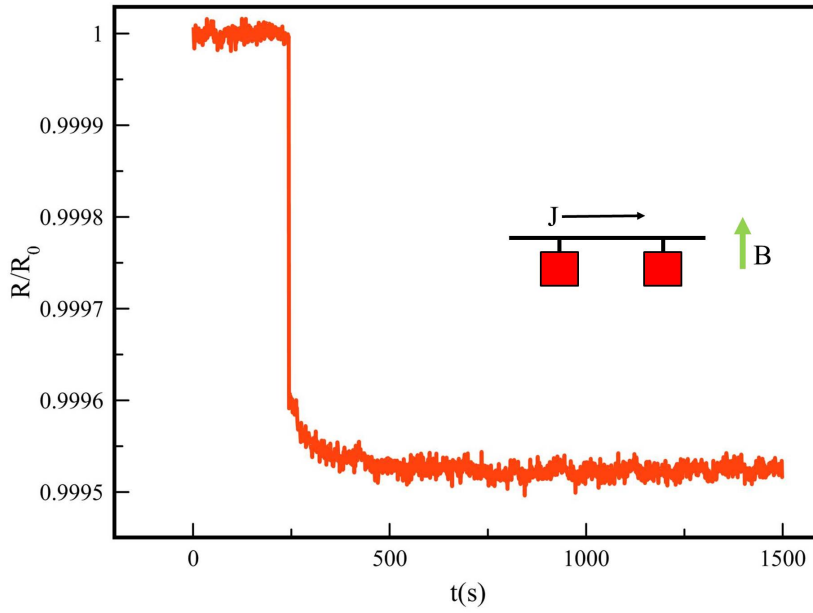


FIGURE 6.3: Value of resistivity recorded for the high magnetic field pulse applied along an easy axis. Measurement was performed for the sample with a reduced crystal quality. The inset shows the direction of the applied magnetic field with respect to the probe current.

As discussed in our previous work [31], Mn_2Au has two easy axes ($[110]$ and $[1\bar{1}0]$) and two hard axes ($[010]$ and $[100]$) [31]. In this work, we have shown that the application of the high field pulse along the hard axis in Mn_2Au does not lead to the transition of the sample with the AFM domain pattern with the preferred orientation of the Néel vector. Instead, it leads to an expansion of domains with two orthogonal Néel vector orientations aligned along the easy axes up to a typical size of to 1-2 μm .

To measure the resistance changes associated with the application of the high magnetic field pulse along the hard axes I performed the following electric transport experiments. The schematic picture of a microstructure used for this experiment is shown in the inset of figure 6.4. This structure allows to measure the AMR of Mn_2Au along the $[010]$ crystallographic direction. Figure 6.4 shows the value of the resistance recorded before and after the application of the magnetic field pulse (60 T) along the $[010]$ hard axis. The probe current was parallel to the magnetic field. In the beginning of the experiment, the sample was in as-prepared state with an equal distribution of the AFM domains with both orthogonal Néel vector orientations. The application of the high magnetic field pulse along the hard axis leads to the resistance changes in the order of 0.005% only (see fig. 6.4). The magnitude of this signal is 300 times smaller than when applying the magnetic field pulse along easy axes. This is an additional confirmation of the fact that the $[110]$ and the $[1\bar{1}0]$ crystallographic directions are the

easy axes of Mn_2Au . This tiny signal presumably originates from the imperfect parallel alignment of the sample with respect to the applied magnetic field or from the domain walls resistance. The signal-to-noise ratio in this experiment is too small to reliably conclude if there is any non-zero signal at all.

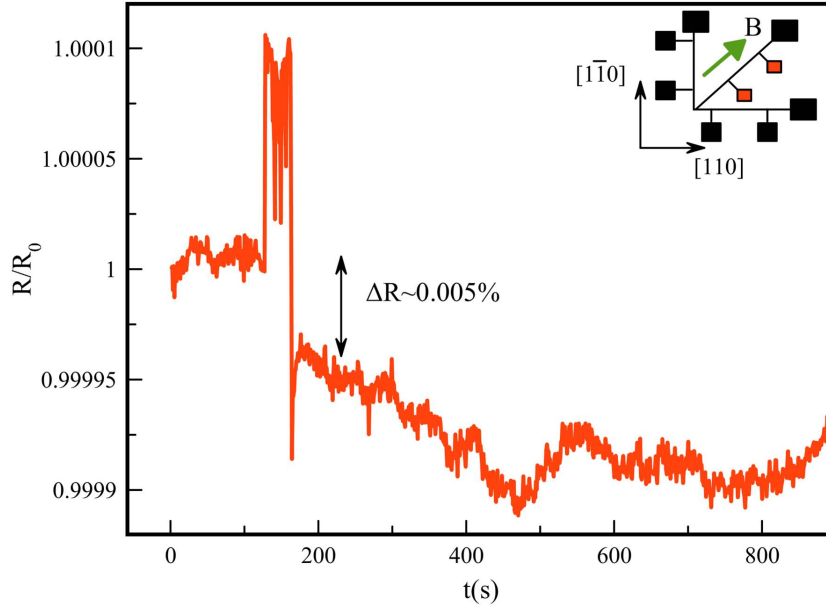


FIGURE 6.4: Value of the resistivity recorded for case of high magnetic field pulse applied along the hard axis. Inset shows the geometry of the experiment.

From the electric transport measurements described in this section we can conclude that the persistent resistance changes associated with a nearly full reorientation of the Néel vector are of the order of 0.15%. The quality of the material has an impact and can change the value of the AMR dramatically. In our particular case the ratio of AMR of the sample with the highest achieved crystal quality to the AMR of the sample with the reduced crystal quality is about 3.

6.2 Fast magnetoresistance measurements

In the previous chapter, I described the persistent changes of the resistivity in Mn_2Au induced by the spin-flop transition. To determine the exact value of the spin-flop field from the magnetotransport measurements we performed experiments on the in-situ resistance measurements during the application of the high magnetic field pulse. During these measurements we discovered that there are additional transient resistance modifications associated with the field-induced Néel vector alignment.

To probe the resistivity value I used the four-point configuration. We applied the AC probe current with an amplitude of 10 mA and a frequency of 20 kHz. The sampling rate was set to 200 kHz. In order to avoid picking up signals generated by electromagnetic induction, I performed a numeric lock-in procedure using a MATLAB based software. I measured values of the resistance during the application of the high field pulse with a duration of 150 ms and additional 10 s after the pulse high field pulse, in order to investigate possible relaxation behavior. Figure 6.5 shows the value of the resistance recorded during the application of the high magnetic field pulse (60 T) along the easy axis of Mn_2Au .

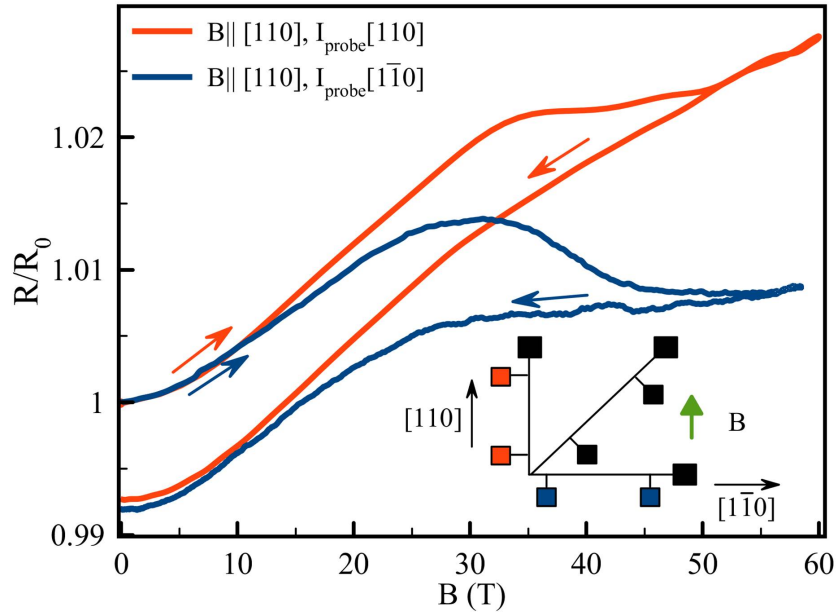


FIGURE 6.5: Normalized field dependent resistances of a Mn_2Au (001) measured during the exposure to the magnetic field pulses applied along $[110]$ and $[\bar{1}\bar{1}0]$ directions with a pulse duration of 150 ms. The resistances are normalized to the sample resistances measured directly before the application of the high field pulse. Note that between both field pulses a waiting time of about 4 h was required.

In figure 6.5 we can clearly see that up to 30 T we can observe an increase of resistance, associated with the ordinary magnetoresistance, which is typical for all kinds of metals including nonmagnetic metals. Additionally to that, we can see a drop of the resistance for the $[110]$ and $[\bar{1}\bar{1}0]$ directions of the probe current (the easy axes of Mn_2Au), observed at the magnetic field between 30 T and 50 T. Consistent with our previous XMLD-PEEM results (see fig. 6.1), I observed a resistance reduction in the field range between 30 T and 50 T, which is associated with the field-induced alignment of the Néel vector originating from the spin-flop transition.

When the magnetic field goes back to zero after the peak value, we can see a drop of resistance for both configurations. In the case of the magnetic field applied along the

easy axes of Mn_2Au , the drop of resistance is around 1.5%. The same measurements were performed for configuration in which the magnetic field was applied along the $[010]$ and the $[100]$ hard axes of Mn_2Au . Figure 6.6 shows the resistance value recorded for this configuration. In case of the application of the high magnetic field along the hard axes, the sample resistance shows similar behavior, as in case of the application of the high field pulse along the easy axes. For the hard axes case, changes of the resistance after the application of the magnetic field pulse are larger than in case of the easy axes. The resistance drop in this case is roughly 2%.

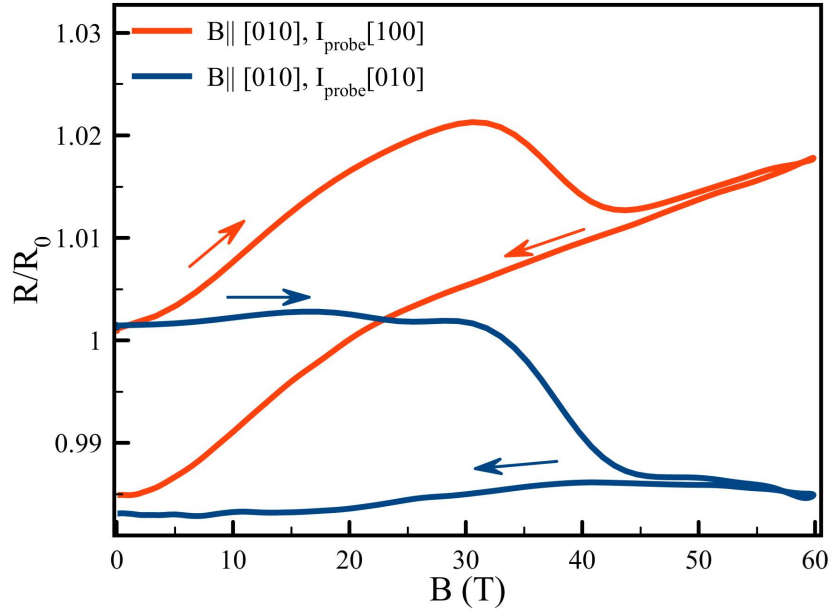


FIGURE 6.6: Normalized magnetoresistance curves of a Mn_2Au (001) measured during the application to a magnetic field pulse along $[010]$ with a duration of 150 ms.

For all configurations of the applied magnetic field, we observed a resistance drop roughly at 30 T. When we performed the same measurements two times in a row we found that the magnetoresistance curve has a similar behavior. Figure 6.7 shows the value of the resistance recorded during the application of the magnetic field pulse which is perpendicular to the probe current. I applied the first high magnetic field pulse of 60 T to the sample which initially was exposed to the 60 T magnetic field pulse in perpendicular direction. After 4 hours I applied the second 60 T magnetic field pulse to the sample along the same direction. During the cooling time the sample was kept in the cryostat. The initial values of resistance before the second pulse are larger than value of the resistance before the first pulse by 0.15%, which is consistent with the persistent AMR value described in the previous section. Also, it is important to notice that the final value for both pulses is the same. In the range of the magnetic field from 30 T

to 0 T, the resistances are identical for both pulses of the applied magnetic field. The absolute values of the resistances after the application of both pulses are the same.

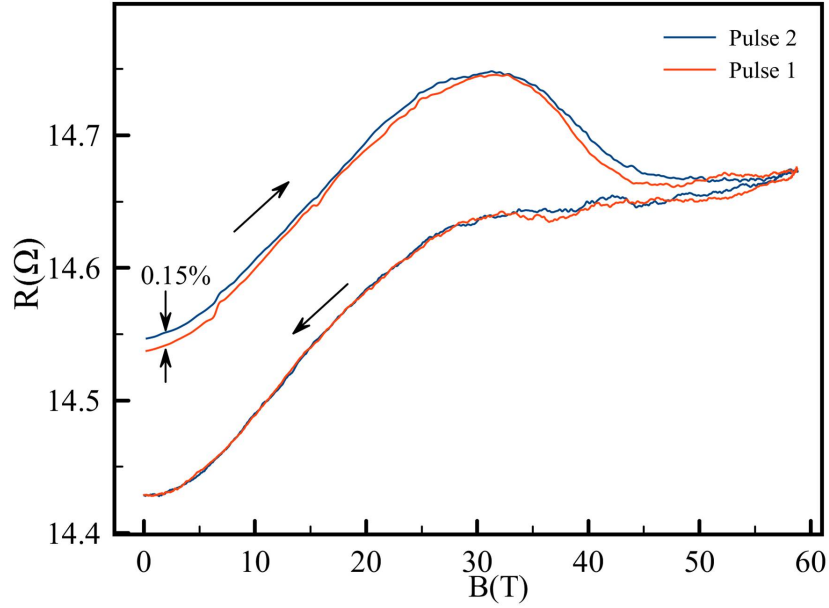


FIGURE 6.7: Normalized magnetoresistances of the Mn_2Au (001) epitaxial thin film recorded for two pulses of magnetic field.

The fact that the final value of the resistance is independent from the initial state after the spin flop transition can be interpreted as the same magnetic state at the moment of the high field pulse application. This hypothesis is also consistent with the geometry of the experiment. For the case of the field pulse applied along and perpendicular to the probe current we observed a similar resistance reduction.

After the application of the high magnetic field pulses the resistance restores on a time scale of 10 seconds. This process of a signal relaxation is related presumably to the restoration of the domain walls taking place after the spin-flop transition. In the next chapter, the phenomenon of the DWs restoration will be discussed.

6.3 The effect of the magnetoresistance relaxation.

As was discussed in the previous chapter, I measured the values of the resistance during the application of the high magnetic field pulses. In order to see how the resistance recovers after the spin-flop, I also recorded the value of the resistance during a period of 10 seconds after the application of the pulse of the magnetic field with the same sampling rate of 200 kHz.

Figure 6.8 shows the resistance value recorded after the application of the high magnetic field pulses (60 T) applied along the different crystallographic directions. In this figure we can see that the resistance is restored on a time scale of 10 s.

The spin-flop transition is associated with a resistance reduction of the sample and independent from a relative orientation of the probe current and the applied magnetic field. From this observation we can exclude anisotropic magnetoresistance as the origin of the observed resistance drop in the range of 1%. At the moment when the 60 T field is applied, the sample is in the state with a lower number of domain walls. Presumably, the formation and the relaxation of the AFM domain walls are origins of the observed decay curves at a longer time scale. The value of resistance after the pulse application of a high magnetic field recovers following logarithmic behavior. This type of relaxation behavior is typical for ferromagnetic materials of different types [44]. Figure 6.8 shows the value of resistance recorded after the application of the magnetic field pulses along different directions.

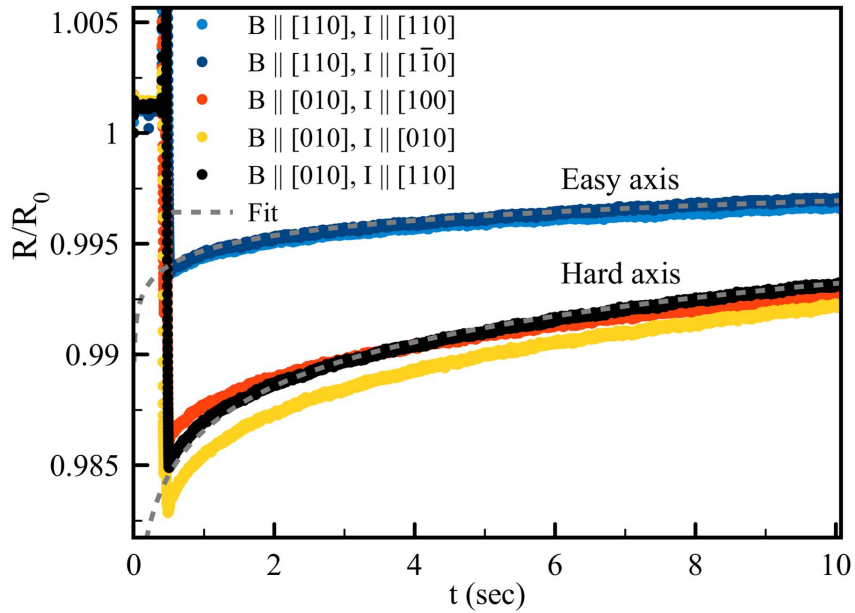


FIGURE 6.8: Time dependence of the normalized magnetoresistances of a Mn_2Au (001) epitaxial thin film probed along different crystallographic directions after the application of the magnetic field pulses along the easy and hard axes. The MR relaxes with a logarithmic time dependence as shown by the fits (dashed curves).

6.4 Visualization of the antiferromagnetic domain pattern of Mn_2Au exposed to large magnetic fields

In order to answer the question of how pulses of the high magnetic field change the domain structure of Mn_2Au , we performed the experiments on the visualization of AFM domain pattern in two steps. As the first step, we visualized the changes of the domain pattern in Mn_2Au induced by the application of a magnetic field pulse with different magnitudes using the XMLD-PEEM [31]. As the second step, we investigated the domain pattern of the bilayer system of $\text{Mn}_2\text{Au}/\text{Fe}$.

Figure 6.9 shows the XMLD-PEEM asymmetry images for a sample a) in the as-prepared state, b) after the application of 30 T magnetic field along the easy axis and c) after the application of 60 T magnetic field along the easy axis. These data were already recently reported in A. A. Sapozhnik's thesis. The samples were prepared under the same conditions and are 240 nm thick. The as-prepared sample shows a domain pattern with roughly equal amount of domains with the orthogonal Néel vectors. In contrast to the as-prepared sample, the sample exposed to 30 T magnetic field along the easy axis shows a large fraction of domains with the Néel vector perpendicular to the applied magnetic field. Nevertheless, in figure 6.9 b) we still can see domains with the Néel vector parallel to the applied magnetic field. These domains have an average size of about $1\text{ }\mu\text{m}$. The sample which was exposed to the 60 T high magnetic field along the easy axis shows an almost monodomain pattern. Only worm-like domains remain with the Néel vector parallel to the applied magnetic field pulse.

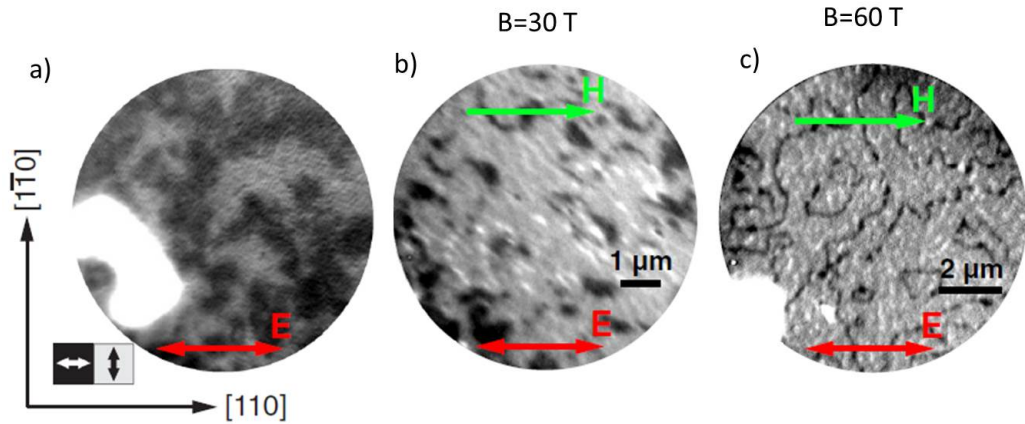


FIGURE 6.9: a) XMLD-PEEM asymmetry image of Mn_2Au in the as-prepared state. b) XMLD-PEEM asymmetry image of Mn_2Au taken after exposure to the 30 T magnetic field along the easy axis. c) XMLD-PEEM asymmetry image of Mn_2Au taken after exposure to the 60 T magnetic field pulse applied along the easy axis [31].

The worm-like structures could possibly be recognized as 180-degree domain walls or as the domains with two 90-degree domain walls. However, XMLD-PEEM cannot distinguish between 180-degree AFM domains. In order to discover the possible presence of 180-degree domains in the Mn_2Au sample exposed to the spin-flop field, we performed experiments on the visualization of the domain structure of the heterostructure of antiferromagnetic Mn_2Au and ferromagnetic Fe. In this case, the Fe top layer, which is coupled to the top antiferromagnetic layer of Mn_2Au , is used as a tracer layer. For these experiments I prepared a thin film of 80 nm Mn_2Au covered by 3 nm Fe layer on top. The sample was grown according to the growth recipe for the smooth films described in chapter 3. The scheme of the stack is shown in figure 6.10.

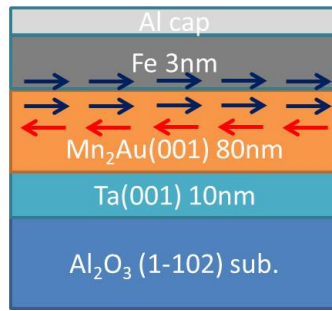


FIGURE 6.10: Mn_2Au sample grown on the R-cut Al_2O_3 substrate. The thin film is covered by polycrystalline Fe, magnetically coupled to the top Mn_2Au layer. The top layer of Al serves as a capping layer which prevents the oxidation of the magnetic layers.

The antiferromagnetic layer of Mn_2Au was covered by 3 nm of polycrystalline Fe deposited at room temperature. To prevent oxidation the Fe layer was covered by 1.5 nm of Al. The sample was exposed to a high magnetic field pulse along the easy axis, similarly to our recent work [31].

The domain pattern was visualized by XMCD/XMLD-PEEM. Figure 6.11 a) shows the XMLD-PEEM asymmetry image of the $\text{Mn}_2\text{Au}/\text{Fe}$ sample calculating the contrast as described in chapter 5. This image shows a similar pattern which was seen in our previous work [31]. In both cases, the worm-like structures separate relatively large AFM domains of Mn_2Au . As the second step, we visualized the domain pattern of the top Fe layer. In order to do that we used an X-ray beam with photon energy $E=709$ eV, which corresponds to the iron absorption edge. The sample was shined by the x-ray beam with two different circular polarization and the XMCD-PEEM asymmetry images were calculated using the following formula:

$$XMCD = \frac{I_{\sigma+} - I_{\sigma-}}{I_{\sigma+} + I_{\sigma-}}, \quad (6.1)$$

where $I_{\sigma+, \sigma-}$ are the intensity images taken at the positive and negative circular polarizations respectively.

Figure 6.11 b) shows the XMCD-PEEM asymmetry image calculated using formula 6.1. This image was taken at the same spot as the XMLD-PEEM asymmetry image.

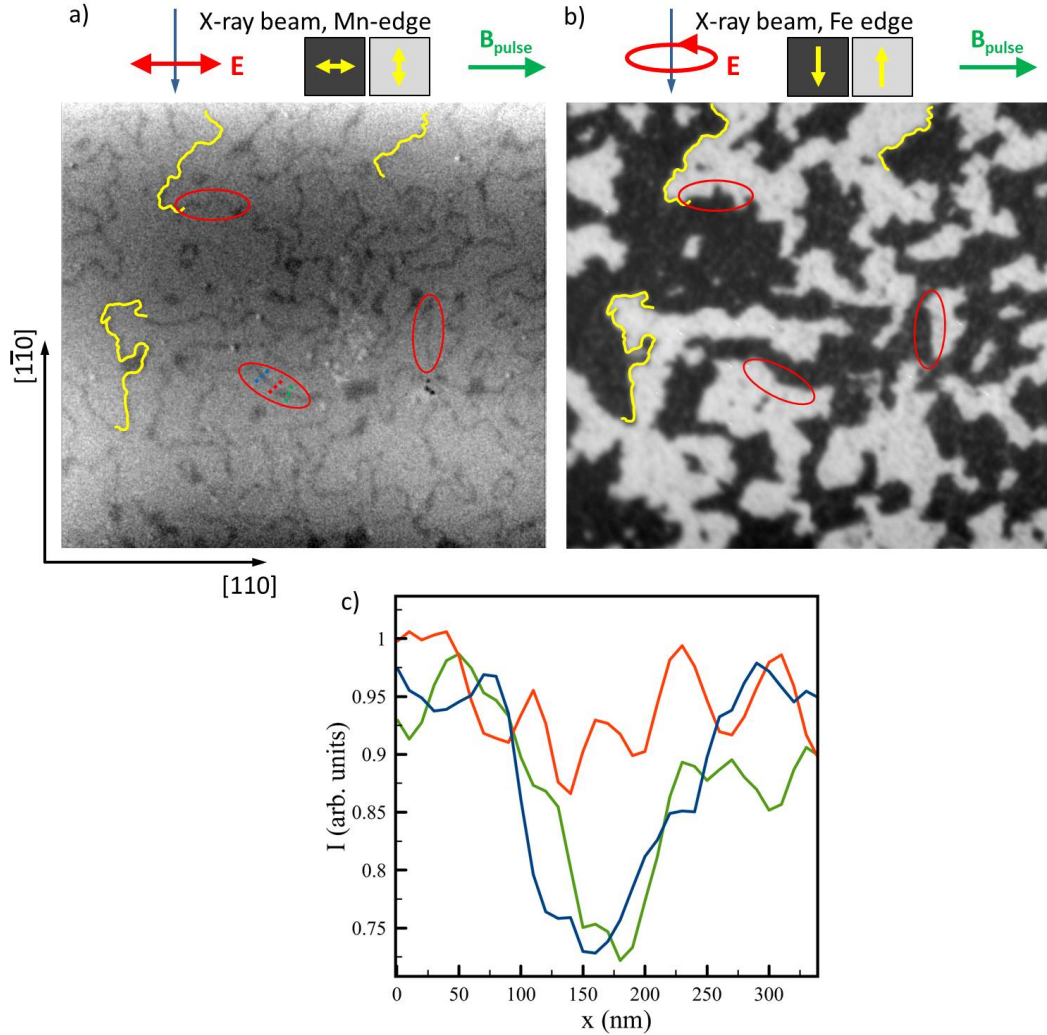


FIGURE 6.11: a) XMLD-PEEM asymmetry image taken from the Mn₂Au (80 nm)/Fe (3nm) thin film exposed to a high magnetic field. The inset indicates the direction of incident x-ray beam and AFM domain color code. b) XMCD-PEEM image taken at the same spot as image a). Inset indicates the color code for iron magnetization direction. c) Domain wall profile taken in the region indicated at the image a) by dashed lines with the corresponding colors.

In figures 6.11 a) and b), we can see that the AFM domain pattern of Mn₂Au and the FM domain pattern of the top Fe layer are strongly correlated. The yellow lines indicate some areas with worm-like structures. It can be noticed from these images that the worm-like domains always separate areas with the opposite direction of iron

magnetization. In this case, the Fe ferromagnetic domain pattern imprints the AFM domain pattern of Mn_2Au . Thus, the worm-like structures separate the 180 degrees AFM domains with the opposite Néel vector orientations.

Note that the worm-like structures do not form closed rings. Instead, there are voids in some parts of the worm-like structures. The red ovals in figure 6.11 a) indicate regions of the worm-like structures with voids in them. In order to make sure that this is not an artifact of the measurements I plotted profiles of the worm-like structures in the void regions. Figure 6.11 c) shows the profile of the worm-like structures. Dashed lines with the corresponding color indicate the lines across the profiles that were taken. Blue and green dashed lines indicate a part near the void and the red curve corresponds to the spot with the void. Red dashed line indicates the area within the void. However, the iron magnetization changes its direction in the void areas. This adds additional evidence to the interpretation of the worm-like structures as narrow 90-degree domains. From figure 6.11 a) we can conclude that the number of 90-degree domain walls in the sample after the spin-flop transition is comparable to the number of the domain walls in the as-prepared state (figure 6.9 a).

Taking into account all the aspects mentioned above, it is possible to build now a model of the Néel vector reorientation induced by a high magnetic field in Mn_2Au . In the as-prepared state, the material has a domain structure with equal amount of domains with two orthogonal orientations of the Néel vector. These domains are separated by 90-degree domain walls (figure 6.14 a). At the moment when the magnetic field pulse (60 T) is applied, the Néel vector flips by 90-degree in the domains which initially had the Néel vector parallel to the applied magnetic field. Two neighboring domains can form one big domain or they can form a 180-degree domain wall between (figure 6.14 b). Vanishing of the 90-degree domain walls corresponds to a resistance drop of 1 % at the MR curves (figure 6.5). As soon as the applied magnetic field goes back to 0, the worm-like domain pattern begins to form. This leads to the formation of two 90-degree DWs instead of one 180-degree DW (figure 6.14 c). Restoration of the 90-degree DWs takes place on a time scale of 10 seconds, which leads to relaxation of the resistance to its initial value (figure 6.8) with correction on the persistent resistance changes of the sample associated with the reorientation of the Néel vector within domains (figure 6.2).

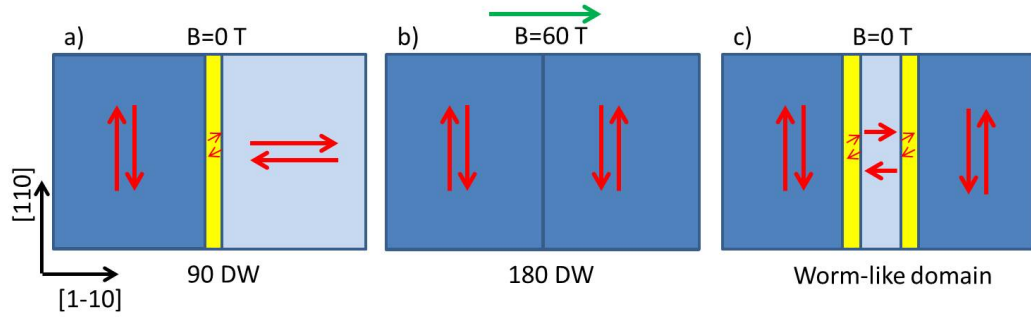


FIGURE 6.12: a) Schematic picture of domain structure in as-prepared state. b) Schematic picture of the domain structure while applying of the high magnetic field pulse along the easy axis. c) Schematic picture of the domain structure at zero field after the application of the high magnetic field pulse.

However, the situation in case of the application of the 60 T field pulse along the hard axis is different. In this case, the magnetic field induces a continuous rotation of the Néel below the spin-flop field (30 T). This brings positive and negative contributions into the magnetoresistance when the probe current is parallel and perpendicular to the Néel vector respectively 6.6. At the magnetic field around 30 T the spin-slop transition takes place in the areas within 90 degrees domain walls. This leads to elimination of the 90-degree domain walls from the sample. The figure below shows a schematic picture of a domain pattern when magnetic field is applied along hard axis.

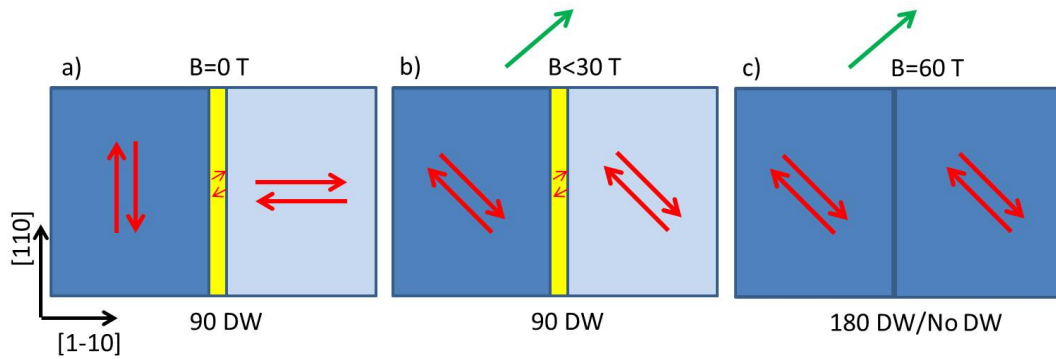


FIGURE 6.13: a) Schematic picture of domain structure in the as-prepared state. b) Schematic picture of the domain structure while the magnetic field 30 of T is applied along hard axis. c) Schematic picture of the domain structure while the magnetic field of 60 T applied along hard axis.

When the magnetic field goes to 0 the domain structure transforms into a pattern with two types of the domains with two orthogonal Néel vector orientations. However, the domains are expanded and have an average size of about 3 mm. The figure below shows the XMLD-PEEM asymmetry image of the sample exposed to the high magnetic field (60 T) along the hard axis.

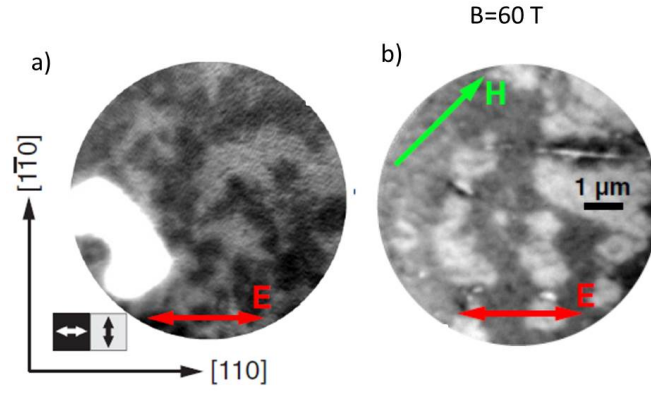


FIGURE 6.14: a) XMLD-PEEM asymmetry image of as-prepared Mn_2Au sample. b) XMLD-PEEM asymmetry image of the sample exposed to a high magnetic field along the hard axis [31].

From all mentioned above we can conclude that there are two contributions of magnetic structures into MR in Mn_2Au . The contribution associated with AMR has a value of 0.15 %. The second contribution associated with the presence of the 90-degree DW results in 1-2 % changes of the resistance. The restoration of the domain pattern happens in the time scale of 10 seconds after the application of high magnetic field.

Chapter 7

Discussion of the results

In this chapter I am going to present a model which describes the experimental results shown in the previous chapters. In order to do that, I first have to give a short overview of the experimental results which are crucial for the understanding of the following model. In transport experiments, described in chapter 4, we observed the changes of the resistance induced by the current pulses in the order of 6 %. From the microscopy measurements we found that the $[110]$ and $[1\bar{1}0]$ crystallographic directions are easy axes of Mn_2Au . Application of the current pulses along the easy axes leads to modifications of the domain pattern which were visualized by XMLD-PEEM. Application of the high magnetic field along the easy axes leads to the persistent modifications of the domain pattern and to resistance changes of two types. The first type is persistent modifications of resistance, which are in the order of 0.15 %, and it is associated with AMR of Mn_2Au . The second type is a resistance reduction which is observed while applying the high field pulse and it has a value in the order of 2 %. After the application of the high magnetic field pulse resistance restores on a time scale of 10 s. Keeping all these facts in mind we can now build a common model of the Néel vector manipulation in Mn_2Au .

7.1 The key role of the NSOT in the current induced manipulation of the Néel vector in Mn_2Au

In chapter 5 I have described the results on the visualization of the current-induced Néel vector switching process in Mn_2Au . There I have shown the changes of the domain pattern in Mn_2Au induced by current pulses which were observed by XMLD-PEEM. First of all, these experimental results provide the first direct evidence that it is possible to manipulate the Néel vector by current pulses in Mn_2Au . The experimental results on

XMLD-PEEM also allow us to conclude that the mechanism, which is responsible for the current-induced Néel vector switching, is NSOT. For that we have several arguments.

The first argument, which supports NSOT as the mechanism of the current induced Néel vector switching in Mn_2Au , is the consistency between the direction of the applied current and the direction of the Néel vector. As mentioned in chapter 5, the application of the current pulse with the current density 10^7 A/cm^2 along the easy axes leads to the reorientation of the Néel vector by 90 degrees with respect to the initial Néel vector orientation. The reorientation of the Néel vector was induced only in the domains with initial orientation of the Néel vector parallel to the applied current pulses. Moreover, in the sample with prealigned Néel vector, the switching process was possible only in case when the direction of the current pulses was parallel to the initial Néel vector orientation. This is consistent with the model of NSOT, described in chapter 1.

The second argument which points towards the conclusion that NSOT is responsible for the current induced Néel vector switching is the fact that the sample is in the AFM state during the application of the current pulses. As mentioned before, the application of the current pulses with the current density of 10^7 A/cm^2 leads to the sample heating up to 500°C (see chapter 4). For the case of the fully thermally activated Néel switching process we should expect random switching events of the Néel vector, which are independent from the relative orientation of the applied current pulses and the Néel vector. This is not the case for the experiments described in chapter 5. This argument points to the conclusion that the main mechanism of current-induced Néel vector switching in Mn_2Au is NSOT.

The last argument which supports NSOT as the mechanism of the current induced Néel vector switching is dependence of the Néel vector switching efficiency on the current density. As mentioned in chapter 1, the staggered magnetic field in Mn_2Au generated by Rashba splitting is proportional to the magnitude of the applied current (see formula 1.3). In our experiments this dependence was observed as an increase of the switched domains fraction after application of higher electric current pulses (see fig. 5.12). However, the sample temperature also increases during the application of the current pulses and its temperature depends quadratically on the applied current. The temperature could have some influence on the switching process, but as I have recently mentioned, samples keep their temperature much below $T_N=1500 \text{ K}$. Thus, temperature can not be the driving force for the Néel vector switching.

These three main arguments bring me to the conclusion that the mechanism responsible for the current-induced Néel vector switching is NSOT. One can argue about the link between the current induced domain structure modifications and the resistance

changes, which were seen in transport experiments (see chapter 4). This will be discussed in the following sections.

7.2 Comparison of the experimentally observed AMR with theoretically estimated values

In chapter 6 I have shown that the application of the high field pulse along the easy axes leads to the presence of the nearly monodomain state of Mn_2Au with small fraction of remained 90 degrees domain walls (see figure 6.9). The fact that changes of the domain pattern induced by high magnetic field pulses are persistent allowed us to determine the AMR value in Mn_2Au , i.e. the difference between the resistance measured along the Néel vector and perpendicular to it. As shown in chapter 6, the AMR value for Mn_2Au is in the order of 0.15%. Our colleague Libor Smejkal performed the calculations of the AMR value in Mn_2Au , which we can compare now with experimentally observed values.

To calculate the AMR in Mn_2Au L. Smejkal used fully relativistic Dirac tight-binding linear-muffin tin orbital (FRD-TB-LMTO) density functional theory (DFT). More details of the AMR calculation can be found in ref. [43]. We considered a monodomain state of Mn_2Au with different orientations of the Néel vector in Mn_2Au ([100] and [110]) and calculated band structures for this case. Using DFT based methods L. Smejkal estimated conductivity for the different cases of the Néel vector alignment. More details of the resistance calculation can be found in ref. [43]. L. Smejkal considered Mn_2Au in monodomain with different orientations of the Néel vector at $T=0$ K. As the source of electron scattering, which contributes into the resistance value, L. Smejkal considered two types of disorders in Mn_2Au . The first type of disorder is the Mn-Au swapping and the second type of disorder is Au excess. He also considered these types of defects for two orientations of the Néel vector in Mn_2Au . Figure 7.1 a) shows the AMR value dependence on the disorder degree of different types.

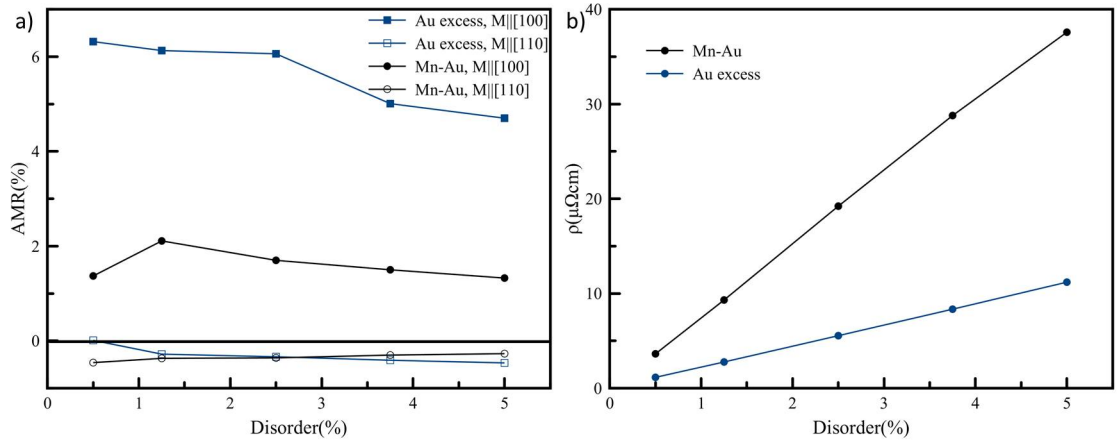


FIGURE 7.1: a) Calculated value of the AMR of Mn_2Au for different types of disorder. b) Calculated dependence of the zero temperature resistance of Mn_2Au on the degree and type of disorder.

In order to examine stoichiometry of our Mn_2Au samples, we performed experiments on the energy dispersion x-ray spectroscopy (EDX). For that we used a 500 nm thin-film of the Mn_2Au (001) sample. The sample showed a stoichiometry with 66.2 ± 0.3 % of Mn and 33.8 ± 0.3 % of Au, which indicates a slight excess of Au atoms. We can expect a small degree of inter-site disorder, but it is not possible to quantify this type of the disorder experimentally. L. Smejkal calculated an intrinsic resistance of Mn_2Au at $T=0\text{K}$ depending on the disorder degree for the Mn-Au swapping and for the Au excess. Figure 7.1 b) shows intrinsic resistance as the function of the disorder degree. Keeping in mind that the experimentally measured value of the resistance at low temperature (4K) is value $7 \mu\Omega\text{cm}$ [22] and results of EDX analysis, we concluded that there is Mn-Au swapping disorder in the order of 1 % in our samples.

As shown in figure 7.1 a), the theoretically estimated value of AMR for the [110] Néel vector orientation is about -0.4% for the 1.25 % Mn-Au swapping disorder degree. The negative sign of the AMR reflects the situation in which the Néel vector parallel to probing current corresponds to a lower resistance state. The calculated value of the AMR is in a good agreement with the AMR value measured during the experiments with the high magnetic field pulses (see fig.6.2). During the experiments described in chapter 6 I measured the AMR value in Mn_2Au in the order of -0.15% .

L. Smejkal also calculated the AMR for the case of Néel vector parallel to the hard axes [100] for the same disorder degrees. For the 1.25 % of Mn-Au swapping we estimated a value of the AMR in the order of 2 %. Experimentally we can observe the situation when the Néel vector is aligned along the hard axes in two cases. The first case is spin alignment within 90-degree domain walls. In chapter 6 I described the experiments on the magnetotransport in Mn_2Au . There we observed a drop of the

resistance in the order of 1.5 % after application of the high magnetic field pulse along the easy axes (see figure 6.5). We attributed this drop of the resistance to the vanishing of the 90-degree DWs. This value is in good agreement with the theoretically estimated value of 2 %. The second case in which the Néel vector can be aligned along the hard axis is when the high magnetic field is applied along the hard axes (see figure 6.6). In this case we observed the changes of the resistance induced by continues rotation of the Néel vector. Also at applied magnetic field of 30 T we can see the drop of the resistance associated with vanishing of the DWs.

The agreement between the theoretically estimated values of AMR and the experimentally measured values points to the conclusion that the AMR in Mn_2Au is in order of 0.15 %, while the DWs bring about 1.5 % of resistance. Thus, DW resistance can have strong influence in the resistance changes induced by the current pulses observed in the experiments described in chapter 4. This will be discussed in more details in the following section.

7.3 Persistent resistance changes induced by the current pulses

In chapter 4 I described the results on the current induced changes of the resistance in Mn_2Au . Application of the current pulses with density 10^7 A/cm^2 leads to the resistance changes in the order of 4-6 %. Note, that the modifications of the domain pattern were observed after the application of the current pulses with the same density (see chapter 5). As mentioned recently, the AMR in Mn_2Au is in the order of 0.15 %. That means we can not consider changes of the resistance induced by the current pulses as the switching of the Néel vector between two monodomain states.

Another source of resistance of magnetic origin which can contribute to the current induced resistance changes is antiferromagnetic domain walls. As mentioned in chapter 6, the DW resistance can bring 2 % in the total resistance value. If we assume that the current pulses can potentially increase or decrease the number of DWs, this could potentially lead to larger changes of the resistance in the order of few percents. Recently the phenomenon of antiferromagnetic domains fragmentation induced by the current pulses in CuMnAs was discovered by M. S. Wornle et al. [45]. In this work the authors observed a nano-scale fragmentation of the antiferromagnetic domains, which was controlled by the amplitude of the applied current pulses. In their experiments the authors used current density in the order 10^7 A/cm^2 , which is similar to current density I used for the Néel vector switching in Mn_2Au . The authors observed the fragmentation

of the antiferromagnetic domains which coexists with permanent switching of the Néel vector induced by NSOT. In case of CuMnAs, the fragmentation of the domains leads to the presence of the higher number of domain walls and to resistance growth associated with it. For Mn₂Au we can expect similar fragmentation of the domains, which would lead to resistance changes in the percent range.

In chapter 5 I described the experimental results on the XMLD-PEEM visualization of the current induced Néel vector switching in Mn₂Au. In our case we can not make any conclusion about the presence of the antiferromagnetic domains fragmentation and formation of the new domain due to rough morphology of our sample. In order to make reliable conclusion about the origins of the current induced resistance changes described in chapter 4, one has to perform the parallel transport experiment and experiments on the visualization of domain pattern changes induced by application of current pulses. We attempted to perform this experiment but it could not be done due to very high noise on the beamline I06 generate by the relay. However, in the future that circumstance can be overcome by using another visualization technique with a lower electrical noise level such as SEM with a polarization analyzer (SEMPA).

Conclusion

As it was recently predicted theoretically, antiferromagnetic Mn_2Au has proper symmetry for manipulation of the Néel vector via NSOT by application of current pulses of magnitude 10^7 A/cm^2 . This antiferromagnetic material combines properties, which are very important for device applications such as relatively good conductivity, high Néel temperature, which is much higher than room temperature and nontoxic composition.

Within this Ph.D. thesis, the experimental realization of the current-induced Néel vector switching is demonstrated. Epitaxial thin-films of Mn_2Au grown by RF-sputtering deposition at high temperature, were patterned into cross-like structures using optical lithography. Current-induced Néel vector switching was observed in transport experiments. The application of current pulses along different crystal directions leads to resistance change in the order of 6 %.

The current induced Néel vector switching process was indeed visualized using XMLD-PEEM. It has been shown that by application of current pulses of density 10^7 A/cm^2 it is possible to switch the Néel vector orientation in a large fraction of AFM domains, up to 35%. Changes of AFM domain pattern induced by current pulses are remanent as well as changes of the current-induced changes of resistance.

Reorientation of the Néel vector was experimentally realized by another approach, using pulses of the high magnetic field above the spin-flop transition of Mn_2Au (60 T). These experiments showed, that there are two contributions to the resistance of magnetic origins. The first contribution is associated with bulk AMR of Mn_2Au and it has value in the order of 0.15 %. This contribution to resistance is persistent. The second contribution is associated with the resistance of antiferromagnetic domain walls. It has the value of the order of 2 % and decays in a time scale of the 10 seconds after the application of high magnetic field pulses. This type of contribution is associated with domain walls of Mn_2Au .

Possibility of the Néel vector manipulation by different means makes Mn_2Au a promising candidate for antiferromagnetic based data storage applications. Moreover, the Néel vector switching can be performed at room temperature.

Appendix A

Appendix

Discharge problem in the X-PEEM experiments.

During the X-PEEM experiments there is a possibility to meet a problem of discharge. During the measurements 12 kV voltage usually is applied between the sample and the objective lens of microscope. In some cases it can cause a discharge. In case of pattern sample, it is crucial to avoid this. Here you can find some tips on how to avoid discharges during the X-PEEM measurements.

The first reason of the discharges is not sufficient vacuum in the X-PEEM vacuum chamber. It is usually the case, when a sample is glued to the sample holder using a silver paste. In this case one has to shine the sample by ultraviolet or mercury lamp for few hours, until the pressure in the chamber is recovered. Another reason, which can cause the bad vacuum conditions is organic materials on top of the sample. This could be for example remained particles of the photoresist.

The second reason which can cause discharges is an open surface of the insulating substrates. In order to avoid this, it is necessary to use a proper mask design. Most of the sample surface should be covered by a conductive material. The contact pads or isolated parts of the sample should be separated by narrow trenches, in order to minimize the open substrate. Figure below shows an example of a mask design used for X-PEEM experiments.

The third reason which can cause discharge is the sharp objects on the sample. This includes pattern with sharp corners, particles on the sample, etc. In case of transport measurements, wires, which are connected to the sample, should be hidden under the cap.

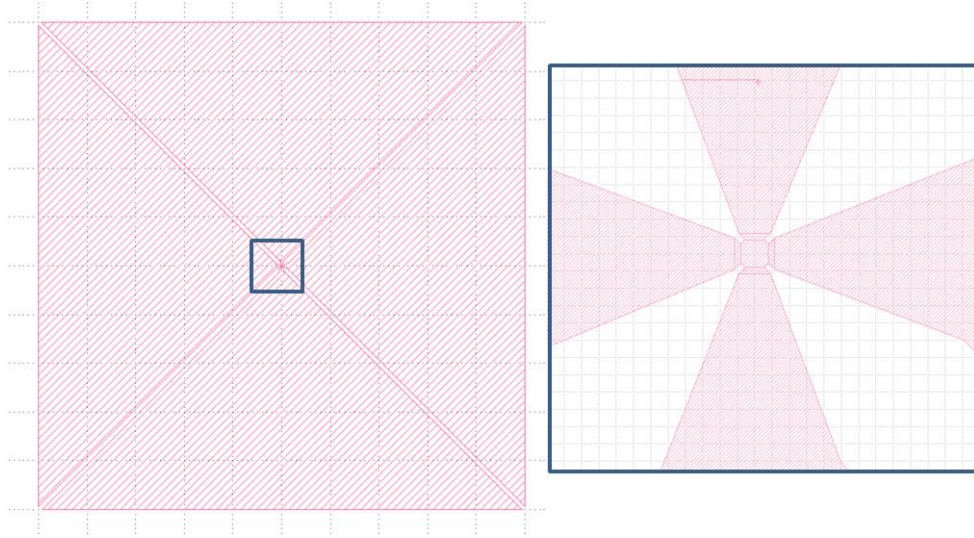


FIGURE A.1: Example of the mask design used for the X-PEEM experiments.

Possible issues in experiments with pulsed magnetic fields.

During our measurements in High Field Laboratory (see chapter 6), I had some issues associated with the measurements.

The main issue associated with experiments, is a voltage drop generated by the high magnetic field pulse. Due to the fact that the value of the applied magnetic field changes rapidly during the pulse, we obtained parasitic voltage drop. In order to avoid this, it is necessary to avoid any wire loop. All wires should be separated into the twisted pairs. Twisted pairs should be glued to the sample holder.

There is also the issue associated with the temperature stability of the sample, in case of the room temperature measurements. The copper coils of the pulse magnet are always cooled to the liquid nitrogen temperature, and in order to perform transport measurements at room temperature it is necessary to mount a heater. After heating up the sample to the room temperature it is necessary to wait for 1 hour in order to get temperature stability of the sample. Figure below shows the temperature value recorded 1 hour after loading sample into the magnetic cryostat.

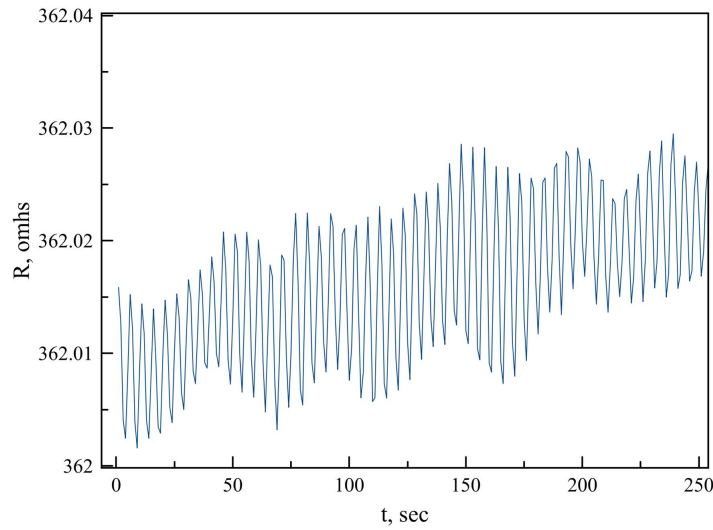


FIGURE A.2: Temperature stability in magnetic cryostat at room temperature.

Data acquisition in beamline I06, Diamond Light Source.

Technical capabilities of beamline I06 allow to perform in situ transport measurements using Keithley 2461 source meter. This device allows to inject the current pulses with an amplitude up to 10 A with total power of 1 kW. The current pulses can be injected using the following python command:

```
pulse [Chanel 1] [Chanel 2] [Pulse Current] [Pulse Width] [Pulse Delay] [Number
of Pulses]
```

This device also can be used in order to probe a value of the sample resistance. Acquiring resistance with probing current of 250 μ A for 20 minutes allows to achieve accuracy of 0.05% at resistance level of 3 ohms. Python code below allows to measure resistance in four probe configuration. Probe current and number of measurements can be changed within the code.

```
def config2461():
    keithley2.communicator.sendCmdNoReply('*RST')

    keithley2.communicator.sendCmdNoReply('SOUR:FUNC CURR')

    keithley2.communicator.sendCmdNoReply('SENS:VOLT:RSEN ON')

    keithley2.communicator.sendCmdNoReply('SOUR:CURRE 0.00025')

    keithley2.communicator.sendCmdNoReply('SOUR:CURRE:READ:BACK ON')

    keithley2.communicator.sendCmdNoReply('SENS:FUNC "VOLT"')
```

```
keithley2.communicator.sendCmdNoReply('SENS:VOLT:UNIT OHM')
keithley2.communicator.sendCmdNoReply('SENS:VOLT:OCOM ON')
keithley2.communicator.sendCmdNoReply('SENS:VOLT:RANG 0.2')
keithley2.communicator.sendCmdNoReply('SENS:VOLT:NPLC 10')
keithley2.communicator.sendCmdNoReply('SENS:VOLT:AZER OFF')
outStr = 'TRIG:LOAD "SimpleLoop", 10, 0, "defbuffer1"'
keithley2.communicator.sendCmdNoReply(outStr)
keithley2.closeConnection()
def startMeas2461():
keithley2.communicator.sendCmdNoReply(':INIT')
```

Bibliography

- [1] L. Neel, Ann. de physique **10**, 5 (1932).
- [2] L. Neel, Ann. de physique **11**, 232 (1936).
- [3] Nobel prize web-page
<https://www.nobelprize.org/prizes/physics/1970/neel/lecture/>
- [4] L. Neel, *Magnetism and the local molecular field*. Nobel Lecture (1970).
- [5] Kampfrath, T. et al. et al., *Coherent terahertz control of antiferromagnetic spin waves*. Nat. Photonics **5**, 31–34 (2011).
- [6] R. Cheng et al., *Terahertz Antiferromagnetic Spin Hall Nano-Oscillator*. Physical Review Letters **116**, 207603 (2016).
- [7] O. Gomonay et al., *Narrow-band tunable terahertz detector in antiferromagnets via staggered-field and antidamping torques*. Phys. Rev. B **98**, 104430 (2018).
- [8] Magnetic Materials, Processes, and Devices 9
- [9] V. Baltz et al., *Antiferromagnetic spintronics*. Reviews of Modern Physics **90**, (2018).
- [10] A. Scholl et. al., *Creation of an Antiferromagnetic Exchange Spring*. Physical Review Letters **9**, 92 (2004).
- [11] Y.Y.Wang et. al., *Room-Temperature Perpendicular Exchange Coupling and Tunneling Anisotropic Magnetoresistance in an Antiferromagnet-Based Tunnel Junction*. Physical Review Letters **109**, 137201 (2012).
- [12] B. G. Park et. al., *A spin-valve-like magnetoresistance of an antiferromagnet-based tunnel junction*. Nature Materials **10**, 347–351(2011).
- [13] T. Moriyama et. al., *Spin torque control of antiferromagnetic moments in NiO*. Scientific Reports **8**, 14167 (2018) .

-
- [14] L. Baldrati et. al., *Mechanism of Néel Order Switching in Antiferromagnetic Thin Films Revealed by Magnetotransport and Direct Imaging*. Physical Review Letters **123**, 177201 (2019).
 - [15] H. Nakayama et. al., *Spin Hall Magnetoresistance Induced by a Nonequilibrium Proximity Effect*. Physical Review Letters **110**, 206601(2013).
 - [16] A. Sapozhnik et. al., *Manipulation of antiferromagnetic domain distribution in Mn_2Au by ultrahigh magnetic fields and by strain*. Physica status solidi **11**,4 (2016).
 - [17] X. Chen et. al., *Electric field control of Néel spin-orbit torque in an antiferromagnet*. Nature Materials **18**, 931–935 (2019) .
 - [18] J. Zelezny et al., *Relativistic Neel-Order Fields Induced by Electrical Current in Antiferromagnets*. Physical Review Letters **113**, 157201 (2014).
 - [19] A. B. Shick et al., *Spin-orbit coupling induced anisotropy effects in bimetallic antiferromagnets: A route towards antiferromagnetic spintronics*. Phys. Rev. B **81**, 212409 (2010).
 - [20] P. Wadley et al., *Electrical switching of an antiferromagnet*. Science, **351**, (2016).
 - [21] P. Wadley et al., *Current polarity-dependent manipulation of antiferromagnetic domains..* Nat Nanotechnol. **13** :362-365 (2018).
 - [22] Jourdan, M. et al. *Epitaxial Mn_2Au thin films for antiferromagnetic spintronics*. Journal of Physics D: Applied Physics **48**, 385001 (2015).
 - [23] Mohammad M. Hassan et al, *Handbook of Antimicrobial Coatings*. (2019).
 - [24] Walter Schottky Institut, *High Resolution X-Ray Diffraction*. Fortgeschrittenpraktikum.
 - [25] G. Zilahi et al., *A common theory of line broadening and rocking curves*. Journal of applied crystallography, **48** (2015).
 - [26] Pennycook, S.J. et al., *Materials Advances through Aberration-Corrected Electron Microscopy*(2011).
 - [27] Weilie Zhou, et al. *Fundamentals of Scanning Electron Microscopy*. (2012).
 - [28] Binnig, G et al. *Atomic Force Microscope*. Physical Review Letters, **56** (9) 930–933 (1986).
 - [29] JPK Instruments *Nanowizard AFM Handbook*.

-
- [30] X. Marti et. al., *Anisotropic magnetoresistance in antiferromagnetic semiconductor Sr_2IrO_4 epitaxial heterostructure*. arXiv:1303.4704
 - [31] A. Sapozhnik et. al., *Direct imaging of antiferromagnetic domains in Mn_2Au manipulated by high magnetic fields*. Phys. Rev. B **97**, 134429(2018).
 - [32] Janis web page
<http://www.janis.com/Products/productsoverview/SuperconductingMagnetSystems>
 - [33] Wikipedia
<https://de.m.wikipedia.org/wiki>
 - [34] BESSY web page
<https://www.helmholtz-berlin.de/>
 - [35] J. E. Penner-Hanh et al., *X-ray Absorption Spectroscopy*.
 - [36] Jolm F. Moulder et al., *Handbook of X-ray Photoelectron Spectroscopy*.
 - [37] Trinity college webpage
<https://www.maths.tcd.ie/~bmurphy/thesis/thesis4.html>
 - [38] J. Stöhr et al., *Magnetism from fundamentals to nanoscale dynamics*. Springer-Verlag Berlin Heidelberg (2006).
 - [39] Peter Böni, Albert Furrer *Neutron Scattering in Layered Copper-Oxide Superconductors*. Springer
 - [40] Stanford Synchrotron Radiation Lightsource,
<https://www-ssrl.slac.stanford.edu/stohr/xmcd.htm>
 - [41] M. Meinert et al., *Electrical Switching of Antiferromagnetic Mn_2Au and the Role of Thermal Activation*. Physical Review Applied 9, 064040 (2018).
 - [42] S. Yu. Bodnar et al., *Imaging of current induced Néel vector switching in antiferromagnetic Mn_2Au* . Phys. Rev. B **99**, 140409(R)(2019).
 - [43] S. Yu. Bodnar et al. *Writing and reading antiferromagnetic Mn_2Au by Néel spin-orbit torques and large anisotropic magnetoresistance*. Nature Communications **9**, 348 (2018).
 - [44] J. I. Arnaudas et al., *Observation of mesoscopic quantum tunneling of the magnetization in systems with strong random magnetic anisotropy*. Phys. Rev. B **47**, (1993).
 - [45] M. S. Wornle et al., *Current-induced fragmentation of antiferromagnetic domains*. arXiv:1912.05287v1

Curriculum Vitae

General information

Name: Stanislav Bodnar

Date of birth: 25.12.1990

Citizenship: Russia/ Hungary

E-mail: sbodnar@uni-mainz.de

Education

2008-2015, Saint-Petersburg State University, Department of Physics (Master of science)

2016-2020, Mainz University, Department of Physics (PhD candidate)

Publication List

1) Bodnar S. Yu. et al., "Exciton mass increase in a GaAs/AlGaAs quantum well in a transverse magnetic field", Phys. Rev. B 95, 195311 (2017)

2) Bodnar S. Yu. et al., "Writing and reading antiferromagnetic Mn₂Au by Néel spin-orbit torques and large anisotropic magnetoresistance", Nature Communications 9, 348 (2018)

3) A. A. Sapozhnik, M. Filianina, S. Yu. Bodnar et al., Direct imaging of antiferromagnetic domains in Mn₂Au manipulated by high magnetic fields. Phys. Rev. B 97, (2018)

4) Bodnar S. Yu. et al., "Imaging of current induced Néel vector switching in antiferromagnetic Mn₂Au", Phys. Rev. B 99, 140409(R) (2019)

5) Bodnar S. Yu. et al., "Domain wall and anisotropic magnetoresistance of the antiferromagnet Mn₂Au" arXiv:1909.12606.

6) H. J. Elmers, S. V. Chernov, S. Dsouza, S. P. Bommanaboyena, S. Yu. Bodnar, et al., "Néel vector induced manipulation of valence states in the collinear antiferromagnet Mn_2Au " (ACS Nano submitted).

Skills

1) Experimental technique: X-PEEM, ARPES , transport measurements, optical lithography, RF-sputtering deposition, AFM, SEM, XRD.

2) Development skills: Matlab, Python, LabVIEW, Origin, MagicPlot.

3) Language: Russian(native speaker), English(fluent), Hungarian(intermediate), German(beginner).

